GLASS CORROSION:
Towards a Unifying Mechanistic Model

Dissertation
zur
Erlangung des Doktorgrades (Dr. rer. nat.)
der
Mathematisch-Naturwissenschaftlichen Fakultät
der
Rheinischen Friedrich-Wilhelms-Universität Bonn

vorgelegt von
Christoph Lenting
aus
Ahaus

Bonn 2018

Angefertigt mit Genehmigung der Mathematisch-Naturwissenschaftlichen Fakultät der Rheinischen Friedrich-Wilhelms-Universität Bonn.

- Redaktionell korrigierte, genehmigte Fassung. -

1. Gutachter: Prof. Dr. Thorsten Geisler-Wierwille (Universität Bonn)
2. Gutachter: Prof. Dr. Sandro Jahn (Universität zu Köln)

Tag der Promotion: 24. Mai, 2019

Erscheinigungsjahr: 2019

An Eides statt versichere ich, dass die vorgelegte Arbeit – abgesehen von den ausdrücklich bezeichneten Hilfsmitteln – persönlich, selbständig und ohne Benutzung anderer als der angegebenen Hilfsmittel angefertigt wurde, die aus anderen Quellen direkt oder indirekt übernommenen Daten und Konzepte unter Angabe der Quelle kenntlich gemacht sind, die vorgelegte Arbeit oder ähnliche Arbeiten nicht bereits anderweitig als Dissertation eingereicht worden ist bzw. sind, kein früherer Promotionsversuch unternommen worden ist, für die inhaltlich-materielle Erstellung der vorgelegten Arbeit keine fremde Hilfe, insbesondere keine entgeltliche Hilfe von Vermittlungs- bzw. Beratungsdiensten (Promotionsberater oder andere Personen) in Anspruch genommen wurde sowie keinerlei Dritte vom Doktoranden unmittelbar oder mittelbar geldwerte Leistungen für Tätigkeiten erhalten haben, die im Zusammenhang mit dem Inhalt der vorgelegten Arbeit stehen, die vorgelegte Dissertation an der nachstehend aufgeführten Stelle vollständig/auszugsweise veröffentlicht worden ist (s. unten).

Kapitel 4 - *Corrosion rim-glass interface*

> C. Lenting, O. Plümper, M. Kilburn, P. Guagliardo, M. Klinkenberg, and T. Geisler, “Towards a unifying mechanistic model for silicate glass corrosion,” npj Materials Degradation, vol. 2, no. 1, p. 28, Sep. 2018

“The First Law of Mentat: A process cannot be understood by stopping it. Understanding must move with the flow of the process, must join it and flow with it.”

— Frank Herbert, *Dune*

Contents

List of Figures

List of Tables

Danksagung

Zuallererst möchte ich mich hier bei den Menschen bedanken, ohne deren Hilfe, Unterstützung und Kritik diese Dissertation nicht zustande gekommen wäre.

Ich danke herzlich meinem Doktorvater Thorsten Geisler-Wierwille für die Projektstelle und Möglichkeit zur Promotion, für wissenschaftliches Streiten, freie Entfaltungsmöglichkeiten innerhalb des Projektes und seine persönliche Unterstützung. Ebenso danke ich Chris Ballhaus für seine Unterstützung.

Ferner möchte ich mich besonders bei Raúl Fonseca für seinen Rat bei analytischen Fragestellungen und Problemen bedanken.

Besonders möchte ich hier eine Reihe von Kollegen erwähnen, die mich bei der experimentellen Durchführung und Analytik unterstützt haben: Christine V. Putnis, die viel Zeit und Mühe für die Durchführung die AFM-Experimente mit mir aufgebracht hat; Martina Klinkenberg und Oliver Plümper, denen ich die Präparation der TEM-Proben und die anschließende Analyse zu verdanken habe; Veronika Rapelius, die mich bei der Lösungsanalyse sehr unterstützt hat; sowie Matt Kilburn und Paul Guagliardo, ohne die die NanoSIMS-Messungen nicht machbar gewesen wären.

Außerdem Danke ich Lars Dohmen und Eugenia Gref für ihre Zusammenarbeit bei den SPFT-Experimenten.

Ich danke außerdem Dieter Lülsdorf und der feinmechanischen Werkstatt, Henrik Blanchard und dem Sekretariat für ihre vielseitige Unterstützung

Ganz persönlich möchte ich mich bei Kerstin und Ti für Zuspruch und Ansporn, bei Matze und den WSDG Jungs und Mädels für mentalen Ausgleich bedanken. Und besonders danke ich Mara.

Diese Arbeit wurde finanziell unterstützt vom *Bundesministerium für Bildung und Forschung* (ImmoRad, 02NUK019F).

Zusammenfassung

Borosilikatgläser werden derzeit zur Immobilisierung von hochradioaktivem Abfall verwendet und sind von Interesse für biomedizinische und industrielle Forschung. Sie sind metastabile Materialien, die in wässrigen Lösungen korrodieren, was sich durch die Bildung von silikatreichen Korrosionssäumen ausdrückt. Bisher gibt es in der wissenschaftlichen Gemeinschaft keinen Konsens über die Reaktions- und Transportmechanismen und die geschwindigkeitslimitierenden Schritte, die bei der Korrosion von Silikatgläsern auftreten. Die meisten Modelle haben die Grundannahme gemeinsam, dass die Ionenfreisetzung aus dem Glasnetzwerk durch Interdiffusion stattfindet und dass das Glasnetzwerk selbst nicht zerstört, sondern nur modifiziert wird. Demgegenüber steht das grenzflächengekoppelte Lösung-Fällungs-Modell, das zunächst für Mineralverdrängungsreaktionen entwickelt und kürzlich auf Glaskorrosion adaptiert wurde. Dieses Modell basiert auf der kongruenten Auflösung des Glasnetzwerks, welche räumlich und zeitlich an die Fällung und Polymerisierung von Kieselsäure, die den amorphen Korrosionssaum bildet. gekoppelt ist. Die Auflösung einer radionuklidbindenen Glasmatrix ist besonders kritisch für die sichere Entsorgung von vitrifiziertem, hochradioaktivem Abfall Eine fundierte Beschreibung der Reaktionsmechanismen und die Identifizierung der ratenlimitierenden Schritte ist daher essentiell, um die Langzeitkorrosion von Silikatgläsern zuverlässig vorherzusagen, insbesondere wenn aus Sicherheitsgründen Zeitskalen von mehreren tausend bis Millionen von Jahren, wie für nukleare Endlager vorgesehen, bedacht werden müssen. In drei Projektstudien wurde das breite Spektrum der Korrosion von Borosilikatgläsern beginnend mit den ersten Oberflächenpräzipitaten an einer sich nach innen bewegenden Lösung-Fällungsgrenzfläche untersucht. Weiterhin wurde die dynamische Entwicklung des Korrosionsrandes selbst und als auch das Verhalten einzelner Spezies innerhalb des Korrosionsaums und über die Saum-Glas-Grenzfläche hinaus verfolgt. Ergebnisse

von Rasterkraftmikroskopie und Durchflussexperimenten lieferten deutliche Hinweise auf einen signifikanten Zusammensetzungsunterschied zwischen der Lösung an der Oberfläche und der Gesamtlösung. Daraus folgt, dass lokale Übersättigung der Grenzflächenlösung an Kieselsäure erklären kann, wie die Ausfällung von amorpher Kieselerde an der Glasoberfläche auftreten kann, obwohl die Gesamtlösung noch untersättigt ist. Um die dynamische Entwicklung des Korrosionssaums in Ort und Zeit zu analysieren, wurde eine neue *in situ* ramanspektroskopische Methode mit Fluidzellen entwickelt. Diese Methode erlaubt die kongruente Auflösung des Glases und gleichzeitig die Präzipitation und Polymerisierung der Kieselerde bei erhöhten Temperaturen in Raum und Zeit zu verfolgen, ohne dabei das Experiment abbrechen zu müssen. Zum ersten Mal konnte so die Bildung einer kieselsäure- und wasserreichen Zone an der Grenzfläche zwischen Glas und Korrosionssaum *in operando* beobachtet werden. Üblicherweise werden solche Zonen als Lücken oder Risse zwischen dem ursprünglichem Glas und Korrosionssaum beschrieben und auf das Trocknen der Probe zurückgeführt. Jedoch lässt sich aus diesen Ergebnisse schließen, dass diese Diskontinuität ein Merkmal des primären Korrosionsprozesses selbst sind und der Auflösungsprozess innerhalb des darin enthaltenen Grenzflächenfluids stattfinden muss. Zuletzt wurden Multi-Isotopen-Tracerexperimente (^{2}H, ^{18}O, ^{10}B, ^{30}Si, ^{44}Ca) an unbehandelten und zuvor korrodierten Glasmonolithen verschiedener chemischer Zusammensetzung durchgeführt. Die Ergebnisse von Transmissionselektronenmikroskopie und Analysen mittels nanoskaliger Sekundärionen-Massenspektrometrie zeigen eine nanometerscharfe Grenzfläche zwischen dem kieselerdebasiertem Korrosionssaum und dem Glas, an der einzelne Isotopentracer sich voneinander entkoppeln, während innerhalb des Glases Protonendiffusion und Ionenaustausch beobachtet werden kann. Weiterhin wurde eine dichte Schicht zwischen Korrosionssaum und Glas beobachtet, die die gequenchte, kieselsäurereiche Grenzflächenlösung zu sein scheint, welche schon *in operando* im *in situ* Ramanexperiment beobachtet wurde.

Da diese neuen Erkenntnisse nicht mit einem Diffusionsprozess im Festkörper erklärt werden können, noch das klassische grenzflächengekoppelte Lösung-Fällungs-Modell Ionenaustausch im Glas berücksichtigt, wird ein vereinendes mechanistische Modell vorgeschlagen, welches alle bisherigen, kritischen Beobachtungen anhand natürlich und experimentell korrodierter Gläser berücksichtigt. Der hauptsächlich den Korrosionssaum bildende Prozess basiert dabei auf der grenzflächengekoppelten Auflösung des Glases und Fällung von Kieselerde. Jedoch erlaubt das Modell, dass sich eine Diffusionsfront über mehrere Zehnernanometer direkt vor der Lösungsgrenzfläche entwickelt, sobald die Auflösungsrate aufgrund von Transportlimitierungen langsamer wird als die Diffusionsrate einer jeweiligen Spezies ($D_H = 1.3 \times 10^{-23}\,m^2\,s^{-1}$).

Abstract

Borosilicate glasses are currently used for the immobilization of highly radioactive waste and are materials of choice for many biomedical and research industries. They are metastable materials that corrode in aqueous solutions, reflected by the formation of silica-rich corrosion rims. Until now, there is no consensus in the scientific community about the reaction and transport mechanism(s) and the rate-limiting steps involved in the corrosion of silicate glasses. Most models have the basic assumption in common that ion release from the glass network is occurring via interdiffusion and that the glass network itself is not being disrupted, only modified. On the contrary stands the interface-coupled dissolution-precipitation (ICDP) model, which first was developed for mineral replacement reactions and was recently adapted to glass corrosion. It is based on the congruent dissolution of the glass network that is spatially and temporally coupled to the precipitation and polymerization of silica, forming the amorphous corrosion rim. The dissolution of a radionuclide-binding glass matrix is naturally a sensitive issue for the safe disposal of vitrified high-level nuclear waste. A sound description of the reaction mechanisms and the identification of the rate-limiting steps is essential to predict the long-term corrosion of silicate glasses, particularly when time scales must reach several thousand to millions of years as required by safety regulations for a nuclear repository.

In three project studies, the broad spectrum of borosilicate glass corrosion was investigated from the first surface precipitates at an inward-moving solution-glass interface, over the dynamic development of the corrosion rim itself, and the tracing of individual species within the corrosion rim and across the rim-glass interface. Results of atomic force microscopy and single-pass flow-through experiments deliver strong evidence for a significant compositional difference between the surfacial and bulk solution. Hence, local supersaturation of the interfacial solution with respect to amorphous silica at the glass surface can explain how precipitation of silica can occur when the bulk solution is still undersaturated. To study the dynamic development of the corrosion rim in space and time, a novel fluid cell-based *in situ* Raman spectroscopy method devised. This method allows monitoring the congruent dissolution of the glass and simultaneously the precipitation and polymerization of the silica-based corrosion rim at elevated temperatures in space and time without the need to terminate the running experiment. For the first time, the formation of a silica- and water-rich zone at the interface between glass and corrosion rim could be observed *in operando*. Commonly such zones were identified *post mortem* as gaps or cracks between pristine glass and corrosion rim, and, hence, referred to as result of sample drying. However, these results show that these discontinuities are a primary feature of the corrosion process itself and that the dissolution process must proceed within the therein present interfacial fluid. Lastly, multi-isotope tracer (^{2}H,^{18}O,^{10}B, ^{30}Si, ^{44}Ca) experiments were performed on pristine and already corroded glass monoliths of different glass compositions. Results of transmission electron microscopy and analyses by nanoscale secondary ion mass spectrometry reveal a nanometre-sharp interface between the silica-based corrosion rim and the glass, where decoupling of isotope tracer occurs, while proton diffusion and ion exchange can be observed within the glass. Moreover, a dense layer was observed between the corrosion rim and glass, which appears to the quenched silica-rich interfacial (pore) solution, which was observed *in operando* in the *in situ* Raman experiment.

As these new findings cannot be explained by solid-state diffusion processes, nor the classical ICDP process accounts for ion exchange in the glass, a unifying mechanistic model is proposed, which accounts for all critical observations so far made on naturally and experimentally corroded glasses. The main corrosion rim forming process is based on the interface-coupled glass dissolution-silica precipitation reaction. However, a diffusion front over several tens of nanometres may evolve in the glass ahead of the dissolution interface once transport limitations cause the dissolution rate to become slower than the diffusion rate of individual species ($D_{H} = 1.3 \times 10^{-23}\,m^{2}\,s^{-1}$).

Chapter 1

Introduction to Glass Corrosion

Glass and in consequence glass corrosion has accompanied humankind since 3500BC. It is still under discussion where and in which century in the middle east glass objects like glass beads were produced for the first time by human hands(Shortland et al., 2016), but the circumvention of corrosion - or here named degradation - of these artefacts is nowadays the working field of modern museum conservationists. Today's industrial research in the glass corrosion behaviour is for example concerned with the delamination of corrosion products in vial for medical fluids or the prevention of corrosion to glassware in dishwashers. In comparison to human history, natural glasses and their 'aqueous alteration' (=corrosion) span back over geologic time-scales. Most natural glasses are of volcanic origin and are regularly dated back to ages of a few million years (Ewing, 1979). However, abundant preserved volcanic glass was also found in a Carboniferous ignimbrite in New South Wales (Australia) and dated back to an age of 332 ± 4 Ma (K-Ar age) (Hamilton, 1992). Old glass samples provide a unique chance to study the long-term corrosion behaviour and are therefore regarded as natural analogue for the evaluation of glass as disposal matrix for highly radioactive and toxic nuclear waste.

1.1 Glass as matrix for nuclear waste disposal

The three principle sources for highly radioactive waste are spent fuel and liquid waste from the reprocessing in the civil energy production field, nuclear weapon programs as well as naval propulsion technology in the military sector. Within a range of possible waste forms, glass is so-far the preferred and, hence, most studied matrix for the immobilization of radioactive nuclides and their fission products. Starting in already the 1950s, shortly after the first nuclear power plant produced electric energy near Arco, Idaho (USA), in 1951, the work on different glass compositions for the waste disposal was initiated (McCarthy and Society, 1979). The amorphous nature of glass allows the incorporation of a wide range of isotopes into its structure, making it ideal for the direct immobilization of high level nuclear waste. Looking at the long list of radioisotopes produced by nuclear fission in a reactor, it has to be further considered that the multiplicity of ionic radii, valencies and short half-lives, which in turn change the immobilization constrains of the individual ions in time, demand a matrix that is not only resistant to external corrosion, but also flexible enough to accommodate this variety of ions and can structurally bind them over a long time. A variety of glass types and compositions have been investigated over the last half of the 20th century (see Fig. 1.1). On the one

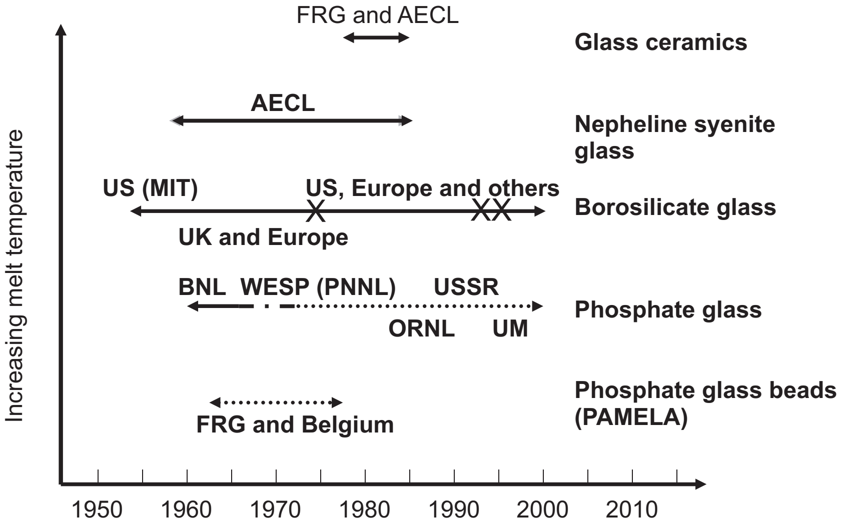

Figure 1.1: Development of nuclear waste glasses over time (taken from Jantzen (2011)). *FRG* = Federal Republic of Germany, *AECL* = Atomic Energy of Canada Limited, *US* = United States of America, *MIT* = Massachusetts Institute of Technology, *BNL* = Brookhaven National Laboratory (US), *WESP (PNNL)* = wet-electrostatic precipitator (Pacific Northwest National Laboratory, US), *USSR* = Union of Soviet Socialist Republics, *ORNL* = Oak Ridge National Laboratory (US), *UM* = University of Michigan (US)

hand, the potential waste glass needs to posses strong chemical durability, mechanical integrity and thermal stability. At the same time, it should also be flexible in regard to the amount of waste loading and potentially incorporate most elements of the nuclear waste. For this, borosilicate glasses are nowadays the matrix of choice. As research for nuclear waste disposal and repository concepts are often enough national efforts, more than one borosilicate glass composition has been proposed and developed. One of the most studied glasses is the French R7T7 with its radio-inactive analogue SON68. The latter was made publicly available as a simplified version (International Simple Glass) containing the six major components of the SON68 in an international effort with the intention make glass corrosion research of different laboratories in the world comparable (Gin et al., 2013b). Another aspect of the immobilization of nuclear waste which needs to be considered is the role of radiation damages caused by the α-, β-, and to a lesser part the γ-decay of the radioactive nuclides. Glass was therefore considered as the ideal immobilization matrix as its molecular structure is *per se* amorphous and hence assumed to be less affected by radiation damage. However, the damage effect of radiation on the glass structure and further on its stability against corrosion is recently a controversial topic in the literature (Weber, 2014; Mir et al., 2015; Peuget et al., 2014, and references therein). A variety of methods is being applied, from direct doping of glass with Pu or other radioactive elements (Rolland et al., 2013; Peuget et al., 2014; Tribet et al., 2014) over simulated damage by radiation with electrons and/or heavy ions (Mir et al., 2015; Lönartz, 2017), to molecular dynamic simulations (Jolley et al., 2015). Encouragingly, the damage caused by the β-decay might actually be partly annealed by the emission of the α-particle from the α-decay (Mir et al., 2015). Lastly, the heat produced by the decay of radionuclides in especially the first few hundred years has to be considered in regard to self-annealing, but also with respect to increased corrosion rates.

1.2 Vitrification & deep geological repository

The main amount of high level nuclear waste for permanent disposal originates from the reprocessing of spent fuels, hence, arrives in a liquefied state. Depending on the chosen vitrification process, the waste will either be consecutively (AVM Marcoule, France) or simultaneously (PAMELA, Germany) calcined and molten together with either individual chemical reagents or preprocessed glass frit. The calcination of high level nuclear waste is performed by heating the liquid waste to 500 to 700 °C, resulting in the decomposition of nitrates and a volume reduction by a factor of 7-10 (M. Ojovan, 2011). Degassing of radioactive nuclides has hereby be taken care of by adequate air filtering. After heating the mixture up to 1200 °C, the resulting glass melt is transferred into stainless steel containers that need to be cooled down at a rate fast enough to suppress any crystallization, but also slow enough to prevent crack formation. Afterwards, the containers will be sealed by welding. Currently operating plants using the AVM procedure like the at La Haque (R7/T7) produce 25 kg vitrified waste per hour at each of their two running production lines (third line is in stand-by for operational reasons) (Liberge et al., 1998; Meleshyn and Noseck, 2013). An overview of past and present vitrification programs can is shown in Section 1.2. The preferred and now approached storage environment is the deep geological repository. Potential sites have to be well studied in respect to structural and hydrogeological characteristics to guarantee current and future geological stability. The question of the ideal host rock itself is not fully solved, and the decision is also depending on what rock formation is available in each country. Three host rock types have been suggested, which each have their merit: (i) Granite is favoured in Sweden and Finland for its strength, and while the Swedish repository site plans at Forsmark are only submitted as of now, Finland scheduled waste burial at the Onkalo site for 2020. At first glance, a hard rock like granite seems ideal, but only in tectonically inactive areas fracturing of the rigid host rock and hence groundwater infiltration can be ruled out. (ii) Large salt bodies: they can compensate to a degree tectonic movements or seismic events due to their ductility. On the other hand, salt solutions are in case of a groundwater breach highly corrosive. At the *Waste Isolation Pilot Plant* near Carlsbad, USA, nuclear waste disposal started in 1999, where low level waste is stored in approximately 650 m depths within a 910 m thick salt formation of the Delaware basin. (iii) The third discussed and researched option for a deep geological waste repository is the use of clay formations as deposits. The main advantage of clay is the low water permeability, which would keep the waste isolated from groundwater. Furthermore, clay minerals can adsorb radionuclides via surface complexation (Nagra, 2002). Waste disposal in clay formations, for instance, is tested in the HADES underground laboratory below the Belgian nuclear research centre SCK·CEN in Mol.

Table 1.1: Operational Data of Vitrification Programs (taken from Ojovan & Williams (2013)). *LILW* = Low- and intermediate-level waste, *HLW* = High-level waste

Facility	Waste Type	Melting Process	Operational Period	Performance
R7/T7, La Hague, France	HLW	IHC[a]	Since 1989/1992	5573 t in 14 045 canisters to 2008, 6430×10^6 Ci
AVM, Marcoule, France	HLW	IHC	1978-2008	1138 t in 3159 canisters, 45.67×10^6 Ci
R7, La Hague, France	HLW	CCM[b]	Since 2003	CCM: U-Mo glass
WVP, Sellafield, UK	HLW	IHC	Since 1991	1800 t in 4319 canisters to 2007, 513×10^6 Ci
DWPF, Savannah River, USA	HLW	JHCM[c]	1996-2011	$\sim$850 t in 3325 canisters, 40×10^6 Ci
WVDP, West Valley, USA	HLW	JHCM	1996-2002	$\sim$500 t in 275 canisters, 24×10^6 Ci
EP-500, Mayak, Russia	HLW	JHCM	Since 1987	$\sim$800 t to 2009, 900×10^6 Ci
CCM, Mayak, Russia	HLW	CCM	Pilot plant	18 kg/h by phosphate glass
Pamela, Mol, Belgium	HLW	JHCM	1985-1991	$\sim$500 t in 2200 canisters, 12.1×10^6 Ci
VEK, Karlsruhe, Germany	HLW	JHCM	2010-2011	60 m of HLW (24×10^6 Ci)
Tokai, Japan	HLW	JHCM	Since 1995	>100 t in 241 canisters (110 L) to 2007, 0.4×10^6 Ci
Radon, Russia	LILW	JHCM	1987-1998	10 t
Radon, Russia	LILW	CCM	Since 1999	>30 t
Radon, Russia	ILW	SSV[d]	2001-2002	10 kg/h, incinerator ash
VICHR, Bohunice, Slovakia	HLW	IHC	1997-2001, upgrading	1.53 m^3 in 211 canisters
WIP, Trombay, India	HLW	IHPT[e]	Since 2002	18 t to 2010 (110×10^3 Ci)
AVS, Tarapur, India	HLW	IHPT	Since 1985	
WIP, Kalpakkam, India	HLW	JHCM	Under testing and commissioning	
WTP, Hanford, USA	LLW	JHCM	Pilot plant since 1998	>1000-2000 t
Taejon, Korea	LILW	CCM	Pilot plant, planned 2005	
Saluggia, Italy	LILW	CCM	Planned	

[a] IHC - Induction, hot crucible.

[b] CCM - Cold crucible melter.

[c] JHCM - Joule-heated ceramic melter.

[d] SSV - Self-sustaining vitrification.

[e] IHPT - Induction-heated pot type melter.

1.3 Glass corrosion

One of the current obstacles in the glass corrosion research is that due to the diversity of scientific backgrounds and working fields of authors, there is a lack of a common language for the description of observations and mechanistic interpretations.

1.3.1 Glossary

To minimize misunderstandings, the most important terms in glass corrosion research and their meaning, shall be revisited in the following:

Congruent dissolution Transition of the glass structure by hydrolysis and rupture of its molecular bonds and degradation into an aqueous solution of the same stoichiometric composition. Stoichiometry of the solution will only be maintained until it is supersaturated with respect to one or more phases.

Corrosion rim Entirety of corrosion products situated between pristine glass and outer surface.

Gel Generalized description for amorphous glass corrosion product building up the major part of the corrosion rim (often used in nuclear waste glass literature).

Fluid boundary layer Layer of fluid in the immediate vicinity of the bordering (glass) surface. An interfacial fluid might have different thermodynamic, chemical and physical properties than the (aqueous) bulk solution, i.e. diffusion, viscosity, solute adsorption, dielectric constant or pH may differ (Ruiz-Agudo et al., 2014 and references therein). The thickness of such a layer may depend on factors like surface charge and bounding properties, diffusivity of ions in the (boundary) solution and dissolution rate of the glass (or mineral), fluid flow and turbulence of the aqueous system. Hence, parameters obtained from analyses of the bulk solution might not represent the actual corrosion conditions.

Glass corrosion General term for the replacement of glass by a secondary, in case of silicate glasses, silica-rich amorphous phase. Glass constituents might thereby be lost to the environment or form mineral precipitates. Commonly, this transformation occurs in an aqueous medium, but is not limited to other environments (e.g. vapour, gas). Also described as *alteration* (Gin et al., 2017; Verney-Carron et al., 2017), *degradation* (Schalm and Anaf, 2016; Vienna et al., 2013), or *deterioration* (Newton and Davison, 1989).

Initial or forward rate Rate describing the congruent dissolution of glass during the initial glass corrosion stage, which, in general, is up to 200 times faster than the residual rate (Gin et al., 2012).

Lamellae Fine, oscillatory zoning in glass corrosion zones, with alternating structural properties and/or chemical composition. Might appear regular or aperiodic.

Leaching Model concept for the diffusion-controlled removal of mobile elements (e.g. alkalis) from the glass matrix without complete disintegration of the glass network (see below for more details).

Palagonite Entirety of corrosion products (*Gel*, phyllosilicates, zeolites, Fe-hydroxides) found in altered natural glasses.

PRI Passivating reactive interface.

Reaction interface Interface between pristine glass and solution during the initial stage of congruent dissolution, later on in the corrosion process the interface between pristine glass and corrosion rim.

Recondensation *In situ* restructuring of the hydrolysed glass network by recombination of previously formed silanol groups to siloxane bridges after the removal of mobile (network modifying) elements (see Eq. (1.1)). By this notion, the glass network structure is not being (entirely) disrupted.

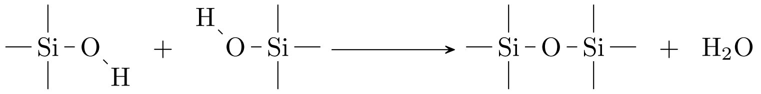

$$-\mathrm{Si{-}O{-}H} \; + \; \mathrm{H{-}O{-}Si}- \longrightarrow -\mathrm{Si{-}O{-}Si}- \; + \; H_2O \tag{1.1}$$

Residual rate Long-term glass corrosion rate. Depending on the applied model it describes the rate of glass corrosion governed by diffusional ion exchange (e.g. Grambow, 2006; Frugier et al., 2008) or transport of dissolved species through the

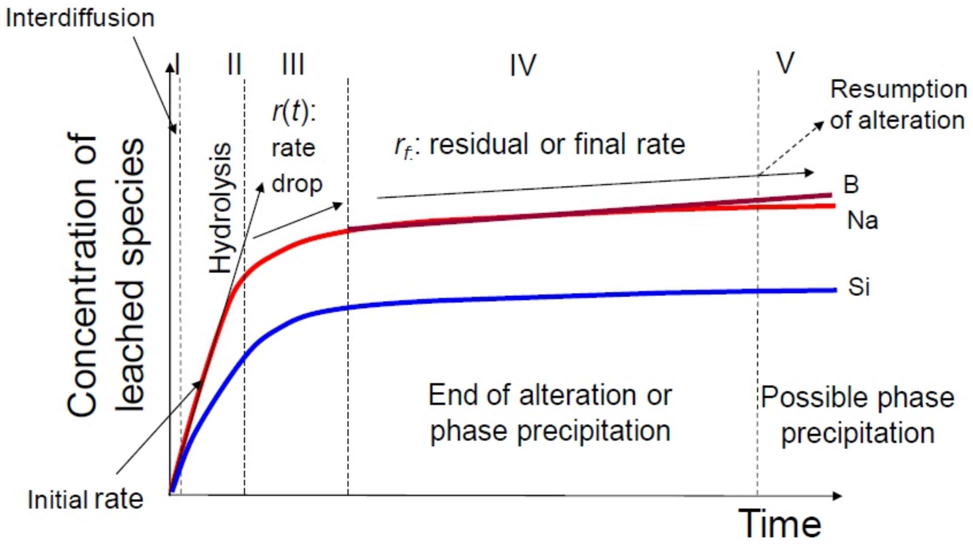

Figure 1.2: Schematic diagram of the corrosion rate regimes over time expressed by normalized concentration of ions in solution (taken from Utton et al. (2011))

reaction rim (e.g. Geisler et al., 2010; Geisler et al., 2015; Hellmann et al., 2012). See below for more details.

Secondary phases Mineral precipitates at the interface between aqueous environment and corroded glass, often occurring in the later stages of glass corrosion.

1.3.2 Glass corrosion models

Understanding and modelling the glass corrosion process in the field of radioactive waste management was always motivated by predicting the corrosion kinetics. Vitrification of high-level nuclear waste can only be recommended as safe disposal strategy under the condition that the extend of corrosion of the radionuclide-bearing glass matrix is admissible over the disposal time - specifically in the (worst) case scenario of water infiltration by a breach of the surrounding barrier systems. Such a breach of the barrier system is considered and parametrized within the safety assessments (J. Ahn, 2010; T. M. Ahn, 2017), but naturally a more durable primary waste form is preferable to complex barrier systems. Accordingly, different (kinetic) glass corrosion model were developed to identify the driving force and rate-limiting steps of the corrosion process (see below). Most models have the basic assumption in common that ion release from the glass network is occurring via diffusive transport and that the glass network itself is not being disrupted, only modified. In most experimental studies (Van Iseghem and Grambow, 1987), the following phenomenological description of the chronological sequence of the glass corrosion process is being used (after Frugier et al., 2008, see also Fig. 1.2), and, hence, aimed to be reproduced by kinetic models:

I. Initial diffusion (or interdiffusion).

II. (Fast) Initial rate (also called forward (dissolution) rate).

III. Rate drop by a factor of up to 200 (Gin et al., 2012; Van Iseghem et al., 2004).

IV. (Slow) Residual rate.

V. Possible resumption of corrosion rate, possibly triggered by secondary phase precipitation (zeolites) (Fournier et al., 2014; Frugier et al., 2017).

The numerical basis for these kinetic regimes are based on solution data analysis varying concentrations of mobile elements like alkalis and boron.

Affinity-driven corrosion

Aagaard & Helgerson 1982 provided an affinity-based rate law for irreversible reactions of silicate minerals in aqueous solutions:

$$d\xi/dt = ks(\prod_i a_i^{-\hat{n}_{i,j}})(1 - exp(-A/\sigma RT)) \tag{1.2}$$

where ξ expresses the overall progress variable, t represents time, k equals the rate constant, s stands for the effective surface area in contact with the aqueous solution, a_i refers to the activity of the ith species in the system, $\hat{n}$ stands for the stoichiometric reaction coefficient of the ith reactant species in the jth reaction corresponding to the reversible formation of the critical activated complex, σ corresponds to the rate of decomposition of the activated complex relative to that of the overall reaction (which is a constant), and A represents the chemical affinity of the overall reaction. Based on transition state theory, the fundamental idea behind this rate law is that dissolution of silicates is conducted by a series of elementary steps. Thereby if all but one step are in equilibrium, the latter step would be rate-limiting and defining the overall reaction rate (Oelkers, 2001; Oelkers and Gislason, 2001). The critical activated complex from transition state theory is seen as a localized surface configuration of elements in the disrupted silicate network, whose irreversible decomposition is controlling the reaction rate. However, close to equilibrium, the reaction rate is proportional to the chemical affinity of the overall reaction. Gin et al. (2008) argues that the application of the Aagaard-Helgeson first order rate law is rather difficult due to the need to determine the content of the affinity function and the activities of each step of the hypothetical series of elementary reactions. In particular, the definition of each elementary reaction step with a complex, multi-oxide glass is called "unrealistic".

Diffusion-driven corrosion

Grambow & Müller (2001) proposed an extended model based on previous work (Grambow, 1984; Grambow, 1997) by adding the influence of glass matrix hydration by water diffusion and ion exchange processes to the affinity-controlled glass network corrosion. The water diffusion hereby enables the alkali release by opening the glass network through formation of silanol groups in the silica ring structures. The diffusion of water and ion release operates parallel to the matrix dissolution, while it is necessarily assumed that the initial diffusion and exchange rates are larger than the rate of matrix dissolution, and that both rates decrease with the square root of time until they equal the dissolution rate. If kept in a steady-state, the diffusion rate is assumed to become constant so that stationary water/alkali diffusion profiles of constant diffusion length will establish in the pristine glass. The experimentally observed amorphous and porous (B. C. Bunker et al., 1984) corrosion rim (often called *gel*), which contains molecular water and provides high ionic mobility (Aines et al., 1986; Doremus et al., 1983), is then thought to form by hydrolysis of the glass network.

Thus, Grambow & Müller (2001) concluded that the rate-limiting step is a thin diffusion layer in the pristine glass in front of the corrosion rim (or dissolution interface), and that the corrosion rim provides a protective effect by limiting the mass transfer of silica into solution. The corrosion rate drop is primarily attributed to the hydration of the glass in the diffusion layer, acting as diffusion barrier against further infiltration of molecular water into the glass network. Furthermore, the corrosion affinity is assumed to be anti-correlated to the silica saturation in solution.

Frugier and co-workers (2008) questioned the phenomenological justification for a corrosion mechanism based on diffusive extraction of mobile elements (alkalis, B, Mo), which is probably a more precise expression for the commonly used term *leaching*. If the corrosion is controlled by diffusion in the solid, element release into solution in a closed system should be proportional to the surface-to-volume (S/V) ratio. While the boron release rate variations over time follow an inverse square root time-dependence ($1/t$), which is characteristic for diffusion in a semi-infinite solid (Chave et al., 2007), Frugier and co-workers observed a non-linear behaviour of the total boron concentrations in solution in regard to the S/V ratio. Instead of looking at the dissolution affinity of the glass, Bourcier et al. (1989) proposed a kinetic corrosion model that is based on the dissolution affinity of the (later) corrosion rim. While Grambow (1984) concentrated on the role of silica and its saturation in the reaction rim, Bourcier et al. assumed all components concentrated in the reaction rim affect the corrosion rate. Eventually, the corrosion rate is thought to be mainly controlled by the ion concentration in solution, which in return is strongly connected to the precipitation of secondary phases. This claim was later questioned by Gin (2001), who performed perturbation experiments, where the reaction solution of a long-term experiment with the SON68 glass was renewed with pure water. Results revealed only a short and slight increase in the reaction rate, which was attributed to a protective effect of the previously formed reaction rim.

Passivating Reactive Interphase

While Grambow & Müller (2001) already pointed out that the reaction rim might have some protective properties, Frugier et al. (2008) established the concept of a *passivating reactive interphase* (PRI) (see Fig. 1.3). The PRI is said to be a thin (3 to 300 nm) intermediate phase between the hydration front and alkali interdiffusion zone (together ~1 nm) in the solid glass and the amorphous reaction rim, and is characterized by sigmoidal diffusion gradients of mobile elements (e.g. alkalis, B, Mo). From the concordance of different element diffusion profiles, network modifiers and formers, it is inferred that not the *leaching*, but the diffusion of water must be the rate-limiting step, thus controlling the overall corrosion progress. The passivating effect is assumed to result from an *in situ* solid-state reorganization of the non-mobilized elements (Si, Ca, Al, Zr, etc.) in the leached glass without being dissolved into solution. In this scenario, the residual reaction rim, here called *depleted gel*, results from *in situ* re-condensation of silanol groups to siloxane bridges. The residual glass is depleted not only in mobile, but also network building elements and offers rapid element diffusion through pore water.

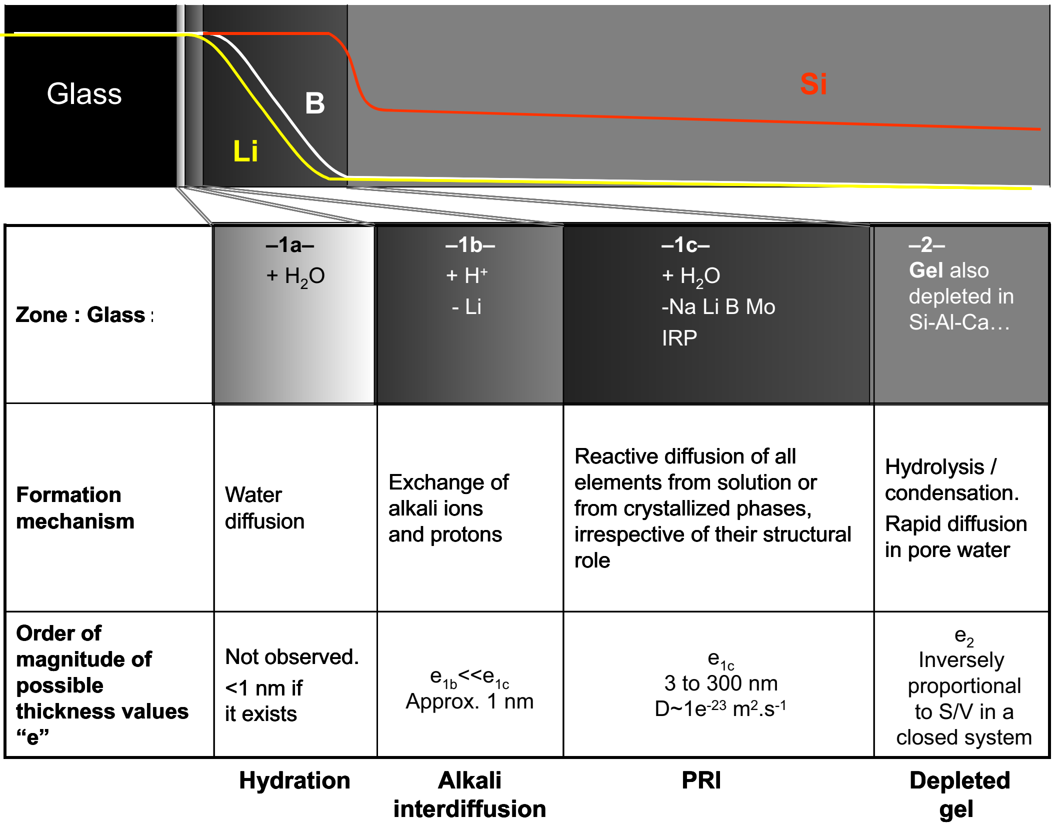

Zone : Glass :	–1a– + H_2O	–1b– + H^+ - Li	–1c– + H_2O -Na Li B Mo IRP	–2– Gel also depleted in Si-Al-Ca…
Formation mechanism	Water diffusion	Exchange of alkali ions and protons	Reactive diffusion of all elements from solution or from crystallized phases, irrespective of their structural role	Hydrolysis / condensation. Rapid diffusion in pore water
Order of magnitude of possible thickness values “e”	Not observed. <1 nm if it exists	$e_{1b} << e_{1c}$ Approx. 1 nm	e_{1c} 3 to 300 nm $D \sim 1e^{-23}$ $m^2.s^{-1}$	e_2 Inversely proportional to S/V in a closed system
	Hydration	**Alkali interdiffusion**	**PRI**	**Depleted gel**

Figure 1.3: Concept model of reaction rim with PRI (taken from Frugier et al. (2008).

GRAAL (*Glass Reactivity with Allowance for Alteration Layer*) Model

The GRAAL model, specifically developed for modelling the long-term corrosion behaviour of the SON68 glass, arose in the wake of the European Commission funded GLAMOR[1] project, which had the goal to achieve a common understanding for the above mentioned corrosion rate decrease (or drop) (Van Iseghem and Grambow, 1987). Briefly, the GLAMOR project suggests to consider both mentioned thoughts of school regarding the glass corrosion mechanism, thermodynamically-driven (affinity) and kinetically controlled (diffusion) dissolution. Hence, the GRAAL model comprises the following (simplified) reaction steps (see also Fig. 1.4):

- Rapid hydrolysis and ion exchange of mobile elements (alkalis, boron, etc.) (Stage I).

---

[1] *A Critical Evaluation of the Dissolution Mechanisms of High-level Nuclear Waste Glasses in Conditions of Relevance for Geological Disposal*

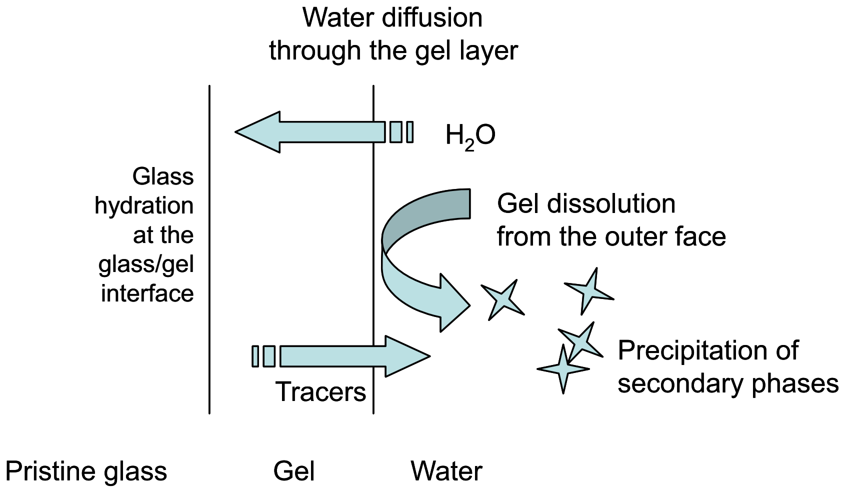

Figure 1.4: Schematic representation of predominant reaction mechanisms considered in the GRAAL model (taken from Frugier et al. (2008)).

- Initially hydrated layer left behind as a result of slower hydrolysis of stronger, glass network bonds (e.g. Si-O-Si, Si-O-Al, Si-O-Zr). This amorphous layer at the glass/solution interface re-organizes by further hydrolysis and condensation. As long as the solution is not saturated with respect to the glass network components, the layer dissolves with the initial/forward (dissolution) rate $\mathrm{r_i}$.

- Corrosion rate drop occurs through continued re-condensation reactions, enabling the amorphous layer to act as transport barrier for any in and out coming species. It should be noted that no distinction between depleted hydrated glass, amorphous gel layer and PRI is specified, but the whole barrier effect is accounted for by the diffusion coefficient of water in the PRI as rate-limiting step for the residual rate $\mathrm{r_0}$ (Stage II).

- Precipitation of secondary phases on the external surface (or in solution) lowers the saturation state of silica in solution, which, in turn, can, depending on the consumed elements, sustain or enhance (Stage III) the glass corrosion.

Mathematically, the GRAAL model comprises five equations for each the kinetics of dissolution and formation of the PRI as for the kinetics of secondary phase precipitation and mass balances of each silicon and boron, representing the network former and mobile elements, respectively.

Interface-coupled dissolution-reprecipitation

While most models have their priority on kinetic modelling of the corrosion rates and have stepwise modified their mechanistic foundation over time, Geisler and co-workers (2010; 2015) adapted the notion of an interface-coupled dissolution-reprecipiation mechanism of mineral replacement reactions (O'Neil, 1977; A. Putnis, 2002; A. Putnis and C. V. Putnis, 2007) to the field of glass corrosion. The fundamental difference in the mechanism between existing glass corrosion models and this newly proposed model is that the new model is based on the congruent dissolution of the (entire) glass network which is spatially and temporally coupled to the precipitation and polymerization of silica, forming the amorphous reaction rim. In this model, the corrosion progress is described as follows (see also Fig. 1.5):

1. In silica undersaturated solutions. the pristine glass that is not in thermodynamic equilibrium with the surrounding solution starts to dissolve congruently by hydrolysis of the surface bonds (Fig. 1.5a).

2. Continuous congruent dissolution of the glass network releases all glass constituents first into a surface-bound fluid layer. This increases the amount of dissolved monomeric silicic acid in the fluid boundary layer which polymerizes towards higher structured forms of dimers and oligomers (Fig. 1.5b) and eventually precipitates on the glass surface (Fig. 1.5c). (Partial) Retention of silica (and other insoluble elements like Zr) within the fluid boundary layer, and proportionally higher transfer of mobile elements into the bulk solution would explain the often observed non-stoichiometry of the bulk solution with respect to the glass composition. This is usually taken as evidence for preferred diffusional loss of mobile elements, *alias leaching.*

3. Silica sphere size and aggregation will mainly depend on the pH and salinity of the fluid boundary layer following the particle growth model of Iler (1979) (Fig. 1.5d).

4. Once the corroded surface is continuously covered by an adherent layer of amorphous silica spheres, transport of dissolved elements released from the glass at the aqueous glass-/reaction rim interface towards the bulk solution becomes more and more controlled by the transport properties of the reaction rim (Fig. 1.5e).

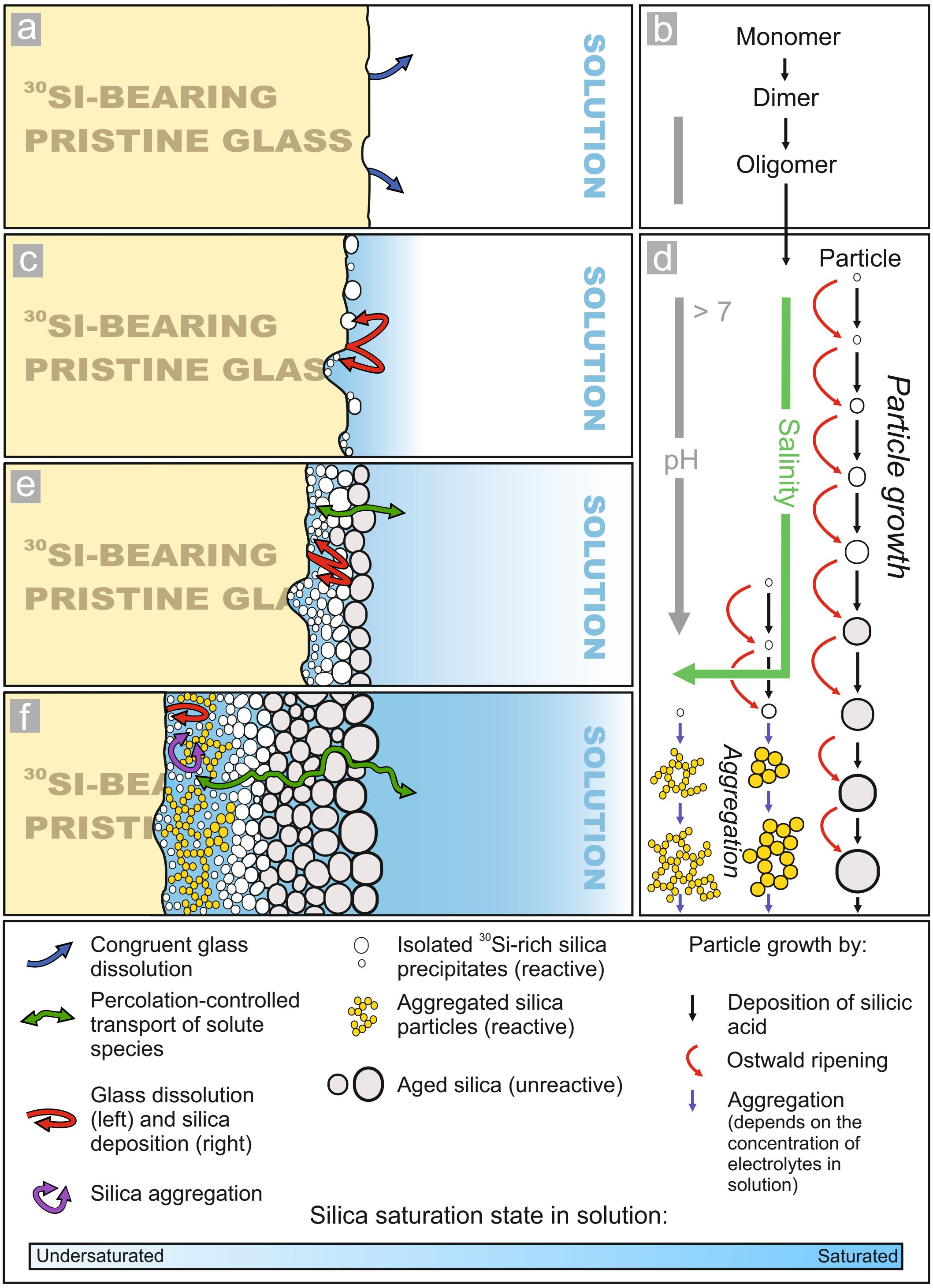

Figure 1.5: Schematic representation of interface-coupled dissolution-reprecipitation mechanism applied for glass corrosion (taken from Geisler et al. (2015)).

5. The growth of the amorphous silica reaction rim is accomplished by continued congruent dissolution of the glass into the inward-moving fluid film. Depending on the pore size, in the reaction rim can become a semi-open or closed chemical environment (Fig. 1.5f). Hence, the interfacial solution must not stand in equilibrium with the bulk solution any more This opens up the possibility for auto-catalytic reactions like the increase of pH by dissolved sodium, which, in turn, increases the solubility of amorphous silica and hereby the corrosion rate.

As such, the ICDP model is fundamentally different to any variation of the *leaching* model. If accurate, total bond-breakage during the corrosion process has to be considered for the immobilization of radionuclides and their daughter products. In contrast to previous models, kinetic modelling of the corrosion progress is not implemented at the status quo.

1.3.3 Currently discussed glass corrosion observations

Due to about half a century of research on glass corrosion, a vast collection of observations regarding textural evolution, corrosion rates, and ion exchange behaviour is available. With the background of formulating a unifying model for the glass corrosion mechanism, the most challenging observation shall shortly be revisited in the following.

Corrosion rate resumption (Stage III)

As reported above, the rate of silicate glass corrosion changes over time, starting with the fast initial dissolution, which then slows down to a residual rate. However, various studies (e.g., Vienna et al., 2013; Fournier et al., 2014) reported a late-stage resumption of the corrosion rate, which is said to be triggered under the following physiochemical conditions:

- High alkali glass composition,
- high S/V ratio,
- $\mathrm{pH}_{20\,^\circ\mathrm{C}} > 10.7$, and/or
- temperatures $\geq 90\,^\circ\mathrm{C}$.

Gin & Mestre (2001) have proposed a macroscopic mechanism for the rate resumption, where zeolites precipitate from the solution rich in silicon and aluminium at the corrosion rim/solution interface. Continued crystal growth consumes aluminium from solution, resulting in aluminium extraction from the corrosion rim. Aluminium being a network former, is thought the play a significant role in the establishment of the protective effect of the corrosion rim (or more specific of the PRI). It has to be noted that the proclamation of this model only hinges on the correlated observation of rate resumption and zeolite precipitation. A detailed understanding on the resumption mechanism on the molecular scale has not yet been given. The point of concern for nuclear waste management is whether the sudden glass corrosion rate acceleration is merely a short term effect of the onset of secondary mineral precipitation or a sustainable rate regime to be accounted for in the long run.

Pattern formation

Long-term corrosion of ancient and natural glasses often results in a corrosion rim consisting of fine lamellae or complex pattern, e.g., Sterpenich and Libourel, 2001; Schalm and Anaf, 2016; Anaf, 2010. The lamellae in corroded ancient glass have been interpreted to reflect seasonal changes in the environment of the buried glass sample and hence could be used for dating the onset of corrosion and burial of the glass object of interest (Brill and Hood, 1961). However, comparable patterned reaction zones were also observed in a variety of glass corrosion experiments with silicate glasses under controlled physiochemically conditions in the laboratory (Anaf, 2010; Dohmen et al., 2013; Geisler et al., 2010), where external influences on fluctuations in the run solution can be excluded. This phenomena of self-organization does not exclude the possibilities of external influence on the manifestation of the patterns formed, but has to have a mechanistic origin. Patterns in corrosion rims can be defined by structural changes (pore/sphere size (Dohmen et al., 2013), ordering of silica spheres (Schalm and Anaf, 2016), or chemical fluctuations (Sterpenich and Libourel, 2001; Geisler et al., 2010), or a combination of both. Whether the occurrence of one might depend or promote the other, is not yet known. In the midst of the 20th century, a correlation was seen between patterned corrosion zones in glass and periodic patterns formed by diffusion-reaction processes at moving reaction fronts (Raw, 1955; Geilmann, 1956). The spatio-temporal self-organization of these so-called Liesegang bands was first described for the diffusion-reaction of two reactants (e.g., HCl, $AgNO_3$) in a matrix of gelatinous mass, where one reactant is introduced into the diffusion matrix already containing the other reactant (Liesegang, 1896). Model ap-

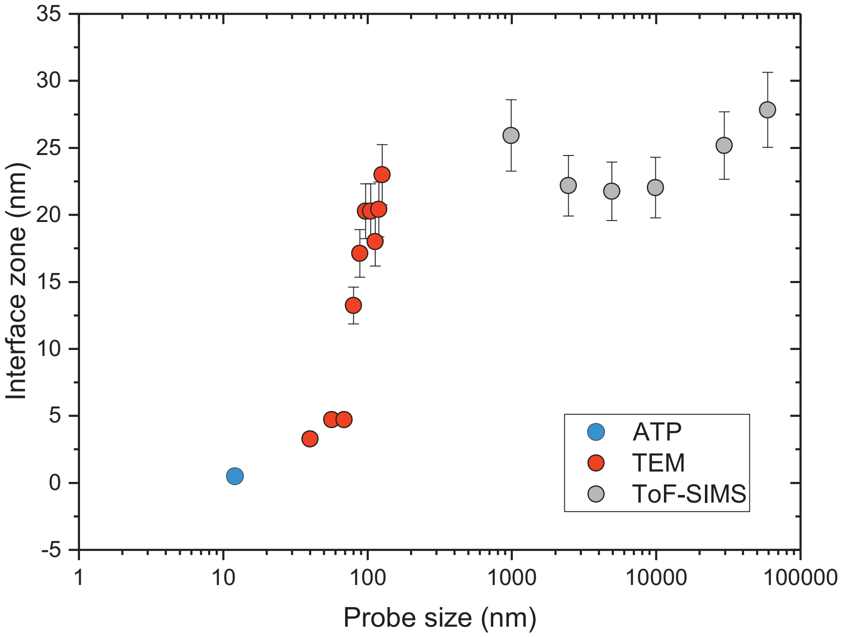

Figure 1.6: Width of the interface gradient zone derived by B profiles as a function of probe size diameter of different analysis techniques (after Gin et al. (2017)).

proaches to explain the periodic pattern formation are roughly divided in the post- and prenucleation stage: (i) during postnucleation or also called competitive particle growth, competition between growing particles alone can spontaneously produce aperiodic and periodic pattern in a gradient-free environment (Feinn et al., 1978; Ortoleva, 1982; Feeney et al., 1983; Sultan and Ortoleva, 1993). Particle ripening via a type of Lifshitz-Slyozov instability (Lifshitz and Slyozov, 1961) results in periodic pattern formation. (ii) Prenucleation represents the classical Oswald-Liesegang supersaturation-nucleation-depletion feedback loop (Ostwald, 1897), where localized crystallization of a supersaturated phase in solution follows to depletion of its components in the adjacent areas (as heterogeneous nucleation is energetically more favourable over homogeneous one). Along these lines, Wang et al. (2016) numerically simulated a nonlinear dynamic model for glass corrosion producing periodic silica and cation concentrations at the glass dissolution interface coupled to an oscillatory dissolution behaviour. This model also allows for at recently discussed atomically sharp dissolution interface previously postulated by different groups (Geisler et al., 2010; Geisler et al., 2015; Hellmann et al., 2015) and later found by atom probe tomography analysis of corroded glass samples (Gin et al., 2017).

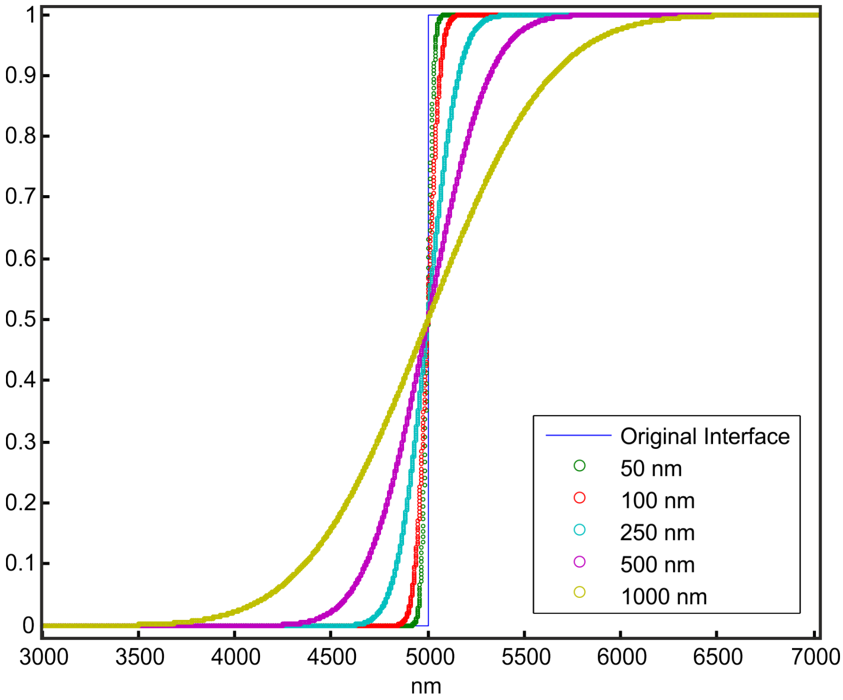

Figure 1.7: Simulation of a concentration profile across an atomically sharp interface as a function of probe size diameter.

Sharp corrosion interface

Several techniques have been applied to define and characterize the interface between pristine glass and corrosion rim. Deep knowledge of the structural (e.g. connectivity of the glass network) and chemical (e.g. ,element distribution) properties of the corrosion interface itself are a key aspect to understand the underlying reaction mechanism. Traditionally, the corrosion mechanism is assumed to be driven by interdiffusion of ions (see Section 1.3.2 for more details). This interpretation is based on sigmoidal-shaped element distribution profiles across the corrosion interface that have frequently been documented (e.g., B. Bunker et al., 1983; Gin et al., 2011; Gin et al., 2013a; Gin et al., 2016; Sterpenich and Libourel, 2006; Robinet et al., 2009; Valle et al., 2010). Over the last decades, the thickness of this so-called gradient or diffusion zones was revised downwards in the light of newer available analysis techniques having a higher spatial resolution (Section 1.3.3, see also Section 1.3.3). Next to direct limitations of the spatial resolution, the probing itself might change the apparent width of the interface. As an example, time-of-flight secondary ion mass spectrometry (ToF-SIMS), one of the widely applied techniques in glass corrosion research, is known to shift individual elements within materials by ion bombardment and can cause artefacts if measured in the depth profiling mode (De Witte et al., 2003). However, also the sub-nanometre resolving atomic probe tomography (APT) struggles with the undisturbed analysis of some elements (e.g., while alkalis are preferentially evaporated over refractory elements, hydrogen analysis seems to work without such problems (Gin et al., 2017)). Nonetheless, recent APT work provided for the first time the direct observation of a sharp corrosion interface (with resolution of 0.15 nm per point across the interface), whereby the residual gradient of 1-2 nm width is attributed to the roughness of the corrosion interface. Such a sharp interface is incompatible with a diffusion-based *leaching* model (see Section 1.3.2), but is in full agreement with the notion of an ICDP process (see Section 1.3.2, p. 15).

1.4 This study

As seen above, a variety of phenomena in the field of glass corrosion cannot be sufficiently explained by the classical *leaching* model and thereby question the proposed corrosion rate models. The aim of this study was to investigate the underlying glass corrosion mechanism, because understanding the corrosion process on a molecular scale is essential to predict the release of any waste elements from the matrix over time and to formulate a realistic rate model. The modelling of glass corrosion rate over the necessary time frame of approx. one million years is in turn the only way to assess the safety of vitrification of (high level) nuclear waste and its disposal in a geological repository. While safeguard systems surrounding the glass package will be installed, groundwater breaches cannot fully be excluded over such a long time. For that reason, it it seems to be essential to ensure that the primary immobilization system, the glass matrix, is stable from the beginning.

Since all currently accepted models are incapable to explain complex pattern formation and diffusion-based corrosion models like GRAAL, are questioned by the recent finding of a nanometre sharp reaction interface (Gin et al., 2017), this study is designed to test and further improve the ICDP model (Geisler et al., 2010; Geisler et al., 2015; Hellmann et al., 2012). For this, the idea was to study glasses ranging from simple to more complex composition (to ensure applicability to any glass) on different scales and times of the corrosion process. Atomic force microscopy (AFM) and single-pass flow-through (SPFT) experiments were applied to investigate the early onset of corrosion and specifically the role of the fluid interface for precipitation of silica (Chapter 2, p. 31).

Conventional glass corrosion experiments have the drawback that the run products have to be analysed *post mortem*. It is unclear so far, what effect the quenching of an experiment has on an unstable phase like the corrosion rim (gel), and how this might effect the interpretation. Therefore, a novel *in situ* Raman technique has been applied to study glass corrosion. The setup of this new, fluid cell-based hyperspectral Raman spectroscopy (FC-HRS), and the herefrom resulting new insights into the dynamic formation of the glass corrosion rim will be presented in Chapter 3 (p. 57).

Finally, multi-tracer experiments (^{2}H, ^{10}B, ^{18}O, ^{30}Si, ^{44}Ca) were designed and carried out to compare corrosion between different glass composition, but more importantly to trace the contribution of solution and glass-derived material for the formation of the corrosion rim. These experiments allowed answering the question of whether the corrosion rim is merely a residual and reshaped 'skeleton' of the original glass network or a newly precipitated phase. The experimental run products were analysed by nanometre-scale secondary ion mass spectrometry (NanoSIMS) and high-resolution scanning transmission electron microscopy (HR-STEM) analyses (Chapter 4, p. 81). Finally, in the light of the observations, a refined version of the interface coupled dissolution-precipitation model for glass corrosion will be given (Chapter 5, p. 127).

1.5 References

Aagaard, P. and H. C. Helgeson (1982). “Thermodynamic and Kinetic Constraints on Reaction Rates among Minerals and Aqueous Solutions; I, Theoretical Considerations”. In: *American journal of Science* 282.3, pp. 237–285.

Ahn, J., ed. (2010). *Geological Repository Systems for Safe Disposal of Spent Nuclear Fuels and Radioactive Waste*. Woodhead Publishing Series in Energy 9. OCLC: 731276033. Cambrigde: Woodhead Publ. 762 pp. ISBN: 978-1-84569-542-2.

Ahn, T. M. (2017). “Risk-Informed Assessment of Radionuclide Release from Dissolution of Spent Nuclear Fuel and High-Level Waste Glass”. In: *Nuclear Engineering and Design* 317, pp. 242–250.

Aines, R. D., H. C. Weed, and J. K. Bates (1986). “Hydrogen Speciation in Hydrated Layers on Nuclear Waste Glass”. In: *MRS Online Proceedings Library Archive* 84.

Anaf, W. (2010). “Study on the Formation of Heterogeneous Structures in Leached Layers during the Corrosion Process of Glass”. In: *CeROArt. Conservation, Exposition, Restauration d’Objets d’Art*. CeROArt asbl.

Bourcier, W. L., D. W. Peiffer, K. G. Knauss, K. D. McKeegan, and D. K. Smith (1989). “A Kinetic Model for Borosilicate Glass Dissolution Based on the Dissolution Affinity of a Surface Alteration Layer”. In: *MRS Online Proceedings Library Archive* 176.

Brill, R. H. and H. P. Hood (1961). “A New Method for Dating Ancient Glass”. In: *Nature* 189.4758, pp. 12–14.

Bunker, B., G. Arnold, E. Beauchamp, and D. Day (1983). “Mechanisms for Alkali Leaching in Mixed-Na-K Silicate Glasses”. In: *Journal of non-crystalline solids* 58.2, pp. 295–322.

Bunker, B. C., T. J. Headley, and S. C. Douglas (1984). “Gel Structures in Leached Alkali Silicate Glass”. In: *MRS Online Proceedings Library Archive* 32.

Chave, T., P. Frugier, A. Ayral, and S. Gin (2007). “Solid State Diffusion during Nuclear Glass Residual Alteration in Solution”. In: *Journal of Nuclear Materials* 362.2-3, pp. 466–473. ISSN: 00223115. DOI: `10.1016/j.jnucmat.2007.01.095`.

De Witte, H., T. Conard, W. Vandervorst, and R. Gijbels (2003). “Ion-Bombardment Artifact in TOF-SIMS Analysis of ZrO 2/SiO 2/Si Stacks”. In: *Applied surface science* 203, pp. 523–526.

Dohmen, L., C. Lenting, R. O. C. Fonseca, T. Nagel, A. Heuser, T. Geisler, and R. Denkler (2013). “Pattern Formation in Silicate Glass Corrosion Zones”. In: *International Journal of Applied Glass Science* 4.4, pp. 357–370. ISSN: 20411286. DOI: `10.1111/ijag.12046`.

Doremus, R. H., Y. Mehrotra, W. Lanford, and C. Burman (1983). “Reaction of Water with Glass: Influence of a Transformed Surface Layer”. In: *Journal of Materials Science* 18.2, pp. 612–622.

Ewing, R. C. (1979). “Natural Glasses: Analogues for Radioactive Waste Forms”. In: *Scientific Basis for Nuclear Waste Management: Volume 1 Proceedings of the Symposium on “Science Underlying Radioactive Waste Management,” Materials Research Society Annual Meeting, Boston, Massachusetts, November 28–December 1, 1978*. Ed. by G. J. McCarthy, R. L. Schwoebel, R. W. Potter, A. M.

Friedman, J. G. Moore, H. C. Burkholder, and W. Lutze. Boston, MA: Springer US, pp. 57–68. ISBN: 978-1-4615-9107-8. DOI: `10.1007/978-1-4615-9107-8_7`.

Feeney, R., S. Schmidt, P. Strickholm, J. Chadam, and P. Ortoleva (1983). “Periodic Precipitation and Coarsening Waves: Applications of the Competitive Particle Growth Modela”. In: *The Journal of Chemical Physics* 78.3, pp. 1293–1311.

Feinn, D., P. Ortoleva, W. Scalf, S. Schmidt, and M. Wolff (1978). “Spontaneous Pattern Formation in Precipitating Systems”. In: *The Journal of Chemical Physics* 69.1, pp. 27–39.

Fournier, M., S. Gin, and P. Frugier (2014). “Resumption of Nuclear Glass Alteration: State of the Art”. In: *Journal of Nuclear Materials* 448.1-3, pp. 348–363. ISSN: 00223115. DOI: `10.1016/j.jnucmat.2014.02.022`.

Frugier, P. et al. (2008). “SON68 Nuclear Glass Dissolution Kinetics: Current State of Knowledge and Basis of the New GRAAL Model”. In: *Journal of Nuclear Materials* 380.1-3, pp. 8–21. ISSN: 00223115. DOI: `10.1016/j.jnucmat.2008.06.044`.

Frugier, P., M. Fournier, and S. Gin (2017). “Modeling Resumption of Glass Alteration Due to Zeolites Precipitation”. In: *Procedia Earth and Planetary Science* 17, pp. 340–343. ISSN: 18785220. DOI: `10.1016/j.proeps.2016.12.086`.

Geilmann, W. (1956). “Antique Glasses. IV. The Decomposition of Glasses in the Soil”. In: *Glastech. Ber., cf. CA 49* 29.4, pp. 145–168.

Geisler, T., A. Janssen, D. Scheiter, T. Stephan, J. Berndt, and A. Putnis (2010). “Aqueous Corrosion of Borosilicate Glass under Acidic Conditions: A New Corrosion Mechanism”. In: *Journal of Non-Crystalline Solids* 356.28-30, pp. 1458–1465. ISSN: 00223093. DOI: `10.1016/j.jnoncrysol.2010.04.033`.

Geisler, T., T. Nagel, M. R. Kilburn, A. Janssen, J. P. Icenhower, R. O. Fonseca, M. Grange, and A. A. Nemchin (2015). “The Mechanism of Borosilicate Glass Corrosion Revisited”. In: *Geochimica et Cosmochimica Acta* 158, pp. 112–129. ISSN: 00167037. DOI: `10.1016/j.gca.2015.02.039`.

Gin, S., I. Ribet, and M. Couillard (2001). “Role and Properties of the Gel Formed during Nuclear Glass Alteration: Importance of Gel Formation Conditions”. In: *Journal of Nuclear Materials* 298.1, pp. 1–10.

Gin, S., J. Ryan, D. Schreiber, J. Neeway, and M. Cabié (2013a). “Contribution of Atom-Probe Tomography to a Better Understanding of Glass Alteration Mechanisms: Application to a Nuclear Glass Specimen Altered 25years in a Granitic Environment". In: *Chemical Geology* 349-350, pp. 99–109. ISSN: 00092541. DOI: `10.1016/j.chemgeo.2013.04.001`.

Gin, S. et al. (2013b). "An International Initiative on Long-Term Behavior of High-Level Nuclear Waste Glass". In: *Materials Today* 16.6, pp. 243–248. ISSN: 13697021. DOI: `10.1016/j.mattod.2013.06.008`.

Gin, S. et al. (2016). "The Controversial Role of Inter-Diffusion in Glass Alteration". In: *Chemical Geology* 440, pp. 115–123. ISSN: 00092541. DOI: `10.1016/j.chemgeo.2016.07.014`.

Gin, S. et al. (2017). "Atom-Probe Tomography, TEM and ToF-SIMS Study of Borosilicate Glass Alteration Rim: A Multiscale Approach to Investigating Rate-Limiting Mechanisms". In: *Geochimica et Cosmochimica Acta* 202, pp. 57–76. ISSN: 00167037. DOI: `10.1016/j.gca.2016.12.029`.

Gin, S. and J. Mestre (2001). "SON 68 Nuclear Glass Alteration Kinetics between pH 7 and pH 11.5". In: *Journal of Nuclear Materials* 295.1, pp. 83–96.

Gin, S., X. Beaudoux, F. Angéli, C. Jégou, and N. Godon (2012). "Effect of Composition on the Short-Term and Long-Term Dissolution Rates of Ten Borosilicate Glasses of Increasing Complexity from 3 to 30 Oxides". In: *Journal of Non-Crystalline Solids* 358.18-19, pp. 2559–2570. ISSN: 00223093. DOI: `10.1016/j.jnoncrysol.2012.05.024`.

Gin, S., C. Guittonneau, N. Godon, D. Neff, D. Rebiscoul, M. Cabié, and S. Mostefaoui (2011). "Nuclear Glass Durability: New Insight into Alteration Layer Properties". In: *The Journal of Physical Chemistry C* 115.38, pp. 18696–18706. ISSN: 1932-7447, 1932-7455. DOI: `10.1021/jp205477q`.

Gin, S., C. Jégou, P. Frugier, and Y. Minet (2008). "Theoretical Consideration on the Application of the Aagaard–Helgeson Rate Law to the Dissolution of Silicate Minerals and Glasses". In: *Chemical Geology* 255.1-2, pp. 14–24. ISSN: 00092541. DOI: `10.1016/j.chemgeo.2008.05.004`.

Grambow, B. (1984). "A General Rate Equation for Nuclear Waste Glass Corrosion". In: *MRS Online Proceedings Library Archive* 44.

Grambow, B. (1997). "Source Trends for Performance Assessment of HLW Glass and Spent Fuel as Waste Forms". In: *MRS Online Proceedings Library Archive* 506.

Grambow, B. and R. Müller (2001). "First-Order Dissolution Rate Law and the Role of Surface Layers in Glass Performance Assessment". In: *Journal of Nuclear Materials* 298.1, pp. 112–124.

Grambow, B. (2006). "Nuclear Waste Glasses - How Durable?" In: *Elements* 2.6, pp. 357–364. DOI: `10.2113/gselements.2.6.357`.

Hamilton, L. H. (1992). "The Oldest Abundant Volcanic Glass on Earth". In: *Australian Journal of Earth Sciences* 39.1, pp. 55–59. DOI: `10.1080/08120099208728000`.

Hellmann, R., S. Cotte, E. Cadel, S. Malladi, L. S. Karlsson, S. Lozano-Perez, M. Cabié, and A. Seyeux (2015). "Nanometre-Scale Evidence for Interfacial Dissolution–Reprecipitation Control of Silicate Glass Corrosion". In: *Nature Materials* 14.3, pp. 307–311. ISSN: 1476-1122, 1476-4660. DOI: `10.1038/nmat4172`.

Hellmann, R., R. Wirth, D. Daval, J.-P. Barnes, J.-M. Penisson, D. Tisserand, T. Epicier, B. Florin, and R. L. Hervig (2012). "Unifying Natural and Laboratory Chemical Weathering with Interfacial Dissolution–Reprecipitation: A Study Based on the Nanometer-Scale Chemistry of Fluid–Silicate Interfaces". In: *Chemical Geology* 294-295, pp. 203–216. ISSN: 00092541. DOI: `10.1016/j.chemgeo.2011.12.002`.

Iler, R. K. (1979). *The Chemistry of Silica: Solubility, Polymerization, Colloid and Surface Properties and Biochemistry of Silica*. John Wiley & Sons. 896 pp. ISBN: 978-0-471-02404-0.

Jantzen, C. (2011). "6 - Historical Development of Glass and Ceramic Waste Forms for High Level Radioactive Wastes A2 - Ojovan, Michael I." In: *Handbook of Advanced Radioactive Waste Conditioning Technologies*. Woodhead Publishing, pp. 159–172. ISBN: 978-1-84569-626-9. DOI: `10.1533/9780857090959.1.159`.

Jolley, K., R. Smith, and K. Joseph (2015). "Borosilicate Glass Potentials for Radiation Damage Simulations". In: *Nuclear Instruments and Methods in Physics Research Section B: Beam Interactions with Materials and Atoms* 352 (Supplement C). Proceedings of the 12th International Conference on Computer Simulation of Radiation Effects in Solids, Alacant, Spain, 8-13 June, 2014, pp. 140–144. ISSN: 0168-583X. DOI: `https://doi.org/10.1016/j.nimb.2014.12.024`.

Liberge, R., J.-L. Desvaux, D. Pageron, and C. Saliceti (1998). "Industrial Experience of HLW Vitrification at La Hague and Marcoule". In: *Proceedings of the Annual Waste Management Symposium*. Waste Management Symposia.

Liesegang, R. (1896). “Über Einige Eigenschaften von Gallerten”. In: *Naturwissenschaftliche Wochenschrift* 10.30, pp. 353–362.

Lifshitz, I. M. and V. V. Slyozov (1961). “The Kinetics of Precipitation from Supersaturated Solid Solutions”. In: *Journal of physics and chemistry of solids* 19.1-2, pp. 35–50.

Lönartz, M. I. (2017). “Effect of Heavy Ion Irradiation on the Sodium Borosilicate Glass Corrosion Rate”. Bachelor’s thesis. Bonn: Rheinische Friedrich-Wilhelms Universität. 40 pp.

McCarthy, G. and M. R. Society (1979). *Scientific Basis for Nuclear Waste Management.* Scientific Basis for Nuclear Waste Management Bd. 1. Plenum Press. ISBN: 978-0-306-40181-7.

Meleshyn, A. and U. Noseck (2013). “Radionuclide Inventory of Vitrified Waste After Spent Nuclear Fuel Reprocessing at La Hague”. In: 56017, V001T02A029. DOI: `10.1115/ICEM2013-96303`.

Mir, A. H., S. Peuget, M. Toulemonde, P. Bulot, C. Jegou, S. Miro, and S. Bouffard (2015). “Defect Recovery and Damage Reduction in Borosilicate Glasses under Double Ion Beam Irradiation”. In: *EPL (Europhysics Letters)* 112.3, p. 36002.

Nagra (2002). *Technical Report 02-05 Project Opalinus Clay.* Safety Report 02-05. ISSN 1015-2636. National Cooperative for the Disposal of Radioactive Waste.

Newton, R. G. and S. Davison (1989). *Conservation of Glass.* Butterworth & Co.(Publishers) Ltd.

O’Neil, J. R. (1977). “Stable Isotopes in Mineralogy”. In: *Physics and Chemistry of Minerals* 2.1, pp. 105–123.

Oelkers, E. H. (2001). “General Kinetic Description of Multioxide Silicate Mineral and Glass Dissolution”. In: *Geochimica et Cosmochimica Acta* 65.21, pp. 3703–3719.

Oelkers, E. H. and S. R. Gislason (2001). “The Mechanism, Rates and Consequences of Basaltic Glass Dissolution: I. An Experimental Study of the Dissolution Rates of Basaltic Glass as a Function of Aqueous Al, Si and Oxalic Acid Concentration at 25 C and pH= 3 and 11”. In: *Geochimica et Cosmochimica Acta* 65.21, pp. 3671–3681.

Ojovan, M. (2011). “1 - Radioactive Waste Characterization and Selection of Processing Technologies”. In: *Handbook of Advanced Radioactive Waste Conditioning*

Technologies. Woodhead Publishing, pp. 1–16. ISBN: 978-1-84569-626-9. DOI: `10.1533/9780857090959.1`.

Ojovan, M. I. and W. E. Lee (2013). *An Introduction to Nuclear Waste Immobilisation*. Newnes.

Ortoleva, P. (1982). "Solute Reaction Mediated Precipitate Patterns in Cross Gradient Free Systems". In: *Zeitschrift für Physik B Condensed Matter* 49.2, pp. 149–156.

Ostwald, W. (1897). "Besprechung Der Arbeit von Liesegangs "A-Linien" (Review on Liesegang's Work "A-Lines")". In: *Physikalische Chemie* 23, p. 365.

Peuget, S., J.-M. Delaye, and C. Jégou (2014). "Specific Outcomes of the Research on the Radiation Stability of the French Nuclear Glass towards Alpha Decay Accumulation". In: *Journal of Nuclear Materials* 444.1, pp. 76–91. ISSN: 0022-3115. DOI: `https://doi.org/10.1016/j.jnucmat.2013.09.039`.

Putnis, A. (2002). "Mineral Replacement Reactions: From Macroscopic Observations to Microscopic Mechanisms". In: *Mineralogical Magazine* 66.5, pp. 689–708. ISSN: 14718022, 0026461X. DOI: `10.1180/0026461026650056`.

Putnis, A. and C. V. Putnis (2007). "The Mechanism of Reequilibration of Solids in the Presence of a Fluid Phase". In: *Journal of Solid State Chemistry* 180.5, pp. 1783–1786. ISSN: 00224596. DOI: `10.1016/j.jssc.2007.03.023`.

Raw, F. (1955). "The Long-Continued Action of Water on Window Glass: Weathering of the Medieval Glass of Weoley Castle, Birmingham, England". In: *J. Soc. Glass Technol* 39, pp. 128–33.

Robinet, L., C. Hall, K. Eremin, S. Fearn, and J. Tate (2009). "Alteration of Soda Silicate Glasses by Organic Pollutants in Museums: Mechanisms and Kinetics". In: *Journal of Non-Crystalline Solids* 355.28-30, pp. 1479–1488. ISSN: 00223093. DOI: `10.1016/j.jnoncrysol.2009.05.011`.

Rolland, S. et al. (2013). "99Tc-and 239Pu-Doped Glass Leaching Experiments: Residual Alteration Rate and Radionuclide Behavior". In: *International Journal of Applied Glass Science* 4.4, pp. 295–306.

Ruiz-Agudo, E., C. Putnis, and A. Putnis (2014). "Coupled Dissolution and Precipitation at Mineral–Fluid Interfaces". In: *Chemical Geology* 383, pp. 132–146. ISSN: 00092541. DOI: `10.1016/j.chemgeo.2014.06.007`.

Schalm, O. and W. Anaf (2016). "Laminated Altered Layers in Historical Glass: Density Variations of Silica Nanoparticle Random Packings as Explanation for the

Observed Lamellae". In: *Journal of Non-Crystalline Solids* 442, pp. 1–16. ISSN: 00223093. DOI: `10.1016/j.jnoncrysol.2016.03.019`.

Shortland, A., K. Eremin, P. Degryse, S. Kirk, and M. Walton (2016). "The Origins of Glass: The Near East or Egypt?" In: Annual Meeting of the American Schools of Oriental Research. San Antonio, Texas. ISBN: 978-0-89757-096-1.

Sterpenich, J. and G. Libourel (2001). "Using Stained Glass Windows to Understand the Durability of Toxic Waste Matrices". In: *Chemical Geology* 174.1–3. 6th International Silicate Melt Workshop, pp. 181–193. ISSN: 0009-2541. DOI: `http://dx.doi.org/10.1016/S0009-2541(00)00315-6`.

Sterpenich, J. and G. Libourel (2006). "Water Diffusion in Silicate Glasses under Natural Weathering Conditions: Evidence from Buried Medieval Stained Glasses". In: *Journal of Non-Crystalline Solids* 352.50-51, pp. 5446–5451. ISSN: 00223093. DOI: `10.1016/j.jnoncrysol.2006.08.041`.

Sultan, R. and P. Ortoleva (1993). "Periodic and Aperiodic Macroscopic Patterning in Two Precipitate Post-Nucleation Systems". In: *Physica D: Nonlinear Phenomena* 63.1-2, pp. 202–212.

Tribet, M., S. Rolland, S. Peuget, V. Broudic, M. Magnin, T. Wiss, and C. Jégou (2014). "Irradiation Impact on the Leaching Behavior of HLW Glasses". In: *Procedia Materials Science* 7, pp. 209–215.

Utton, C., R. Hand, N. Hyatt, and S. Swanton (2011). *Glass Durability in High pH Environments: A Review of the Literature.* Serco Report SERCO/TAS/003133/001.

Valle, N., A. Verney-Carron, J. Sterpenich, G. Libourel, E. Deloule, and P. Jollivet (2010). "Elemental and Isotopic (29Si and 18O) Tracing of Glass Alteration Mechanisms". In: *Geochimica et Cosmochimica Acta* 74.12, pp. 3412–3431. ISSN: 00167037. DOI: `10.1016/j.gca.2010.03.028`.

Van Iseghem, P. and B. Grambow (1987). "The Long-Term Corrosion and Modelling of Two Simulated Belgian Reference High-Level Waste Glasses". In: *MRS Proceedings* 112. ISSN: 0272-9172. DOI: `10.1557/PROC-112-631`.

Van Iseghem, P. et al. (2004). "GLAMOR: A Critical Evaluation of the Dissolution Mechanisms of High-Level Waste Glasses in Conditions of Relevance for Geological Disposal". In:

Verney-Carron, A. et al. (2017). “Understanding the Mechanisms of Si–K–Ca Glass Alteration Using Silicon Isotopes”. In: *Geochimica et Cosmochimica Acta* 203 (Supplement C), pp. 404–421. ISSN: 0016-7037. DOI: `10.1016/j.gca.2017.01.030`.

Vienna, J. D., J. V. Ryan, S. Gin, and Y. Inagaki (2013). “Current Understanding and Remaining Challenges in Modeling Long-Term Degradation of Borosilicate Nuclear Waste Glasses”. In: *International Journal of Applied Glass Science* 4.4, pp. 283–294. ISSN: 20411286. DOI: `10.1111/ijag.12050`.

Wang, Y., C. F. Jove-Colon, and K. L. Kuhlman (2016). “Nonlinear Dynamics and Instability of Aqueous Dissolution of Silicate Glasses and Minerals”. In: *Scientific Reports* 6.1. ISSN: 2045-2322. DOI: `10.1038/srep30256`.

Weber, W. J. (2014). “Radiation and Thermal Ageing of Nuclear Waste Glass”. In: *2nd International Summer School on Nuclear Glass Wasteform: Structure, Properties and Long-Term Behavior, SumGLASS 2013* 7 (Supplement C), pp. 237–246. ISSN: 2211-8128. DOI: `10.1016/j.mspro.2014.10.031`.

Chapter 2

Solution-glass interface

2.1 Introduction

Considering the current discussions and decisions around phasing out of nuclear energy production (e.g., Germany) or the renewed interested in nuclear energy technology to fulfil climate goals, the safe storage of low- to high-level nuclear waste is relevant more than ever. The common proposition and current (cost-effective working) solution for storage of high-level nuclear waste is the use of a borosilicate glass waste form, in which radionuclides and their decay products are incorporated in the glass structure. In the history of glass corrosion studies a series of diffusion-based models for the mechanism of the corrosion process were proposed. These models are mainly based on the diffusion-controlled ion-exchange between the surrounding solution (H^+) and alkaline ions of the radionuclide-containing glass form, which is then followed by an *in situ* reconstruction of the residual glass (e.g., Grambow, 2006; Gin, 2014; Van Iseghem et al., 2004). A more recent model (Geisler et al., 2010; Geisler et al., 2015) adapted the interface-coupled dissolution-reprecipitation model, which is the current standard model for mineral-water reactions (A. Putnis, 2002; A. Putnis and C. V. Putnis, 2007), to explain reaction features like pattern formation in the corrosion rim found in archaeological as well as in experimental glasses (Geisler et al., 2010; Dohmen et al., 2013). An inherit problem of studying glass corrosion lies in the nature of the application of the material: being designed for long-term stability (i.e. $> 10^6$ yr) implies low reactivity and development of reaction rims of only few micrometers in laboratory time scales. To overcome this obstacle, researchers can either increase the duration of corrosion experiments (McLoughlin et al., 2006), use more aggressive settings, while keeping the results still applicable to nature, or move towards a lower scale using techniques with higher spatial resolutions, e.g., time-of-flight secondary ion mass spectrometry (ToF-SIMS) (Gin et al., 2015a; Gin et al., 2015b), transmission electron microscopy (TEM) (Hellmann et al., 2012; Hellmann et al., 2015), and atom probe tomography (ATP) (Gin et al., 2013a; Gin et al., 2017). In this study, atomic-force microscopy (AFM) was used as the tool of choice to observe *in situ* surface modifications on freshly broken glass surfaces with a variety of solutions and settings at the nanoscale. In general, one of the great advantages of AFM is that it directly delivers *in situ* information in real-time on the reactions taking place at the solution-solid interface on a nanometre scale; no other technique so-far is able to delivers these kind of information. On the other hand, observations are restricted to the first reaction steps of the corrosion process occurring at the solid surface, which, however, operate usually well within the applicable lab time scales. Furthermore, fluid-cell based AFM allows to control over the chemistry of the running solution by regular *in situ* exchange. Release of ions by dissolution of the glass parent phase will almost always change the chemical characteristics of the running solution, and, in turn, influence the glass corrosion process. To mitigate this interlinked effect, single pass flow-through setup provide a more stable bulk solution chemistry by constant solution renewal. With the surrounding physiochemically conditions fixed, the next point of interest is the solution-solid interface. Ruiz-Agudo and co-workers (2016) showed that supersaturation at the solution-solid interface without saturation of the bulk solution, resulting in the formation of silica-rich layers, could explain the discrepancy between silicate dissolution rates measured in the laboratory and field. The formation of concentration gradients for ions and pH were hereby observed to be inversely related to the flow rate of the solution. This study aims to investigate the role of the fluid boundary layer at the solution-solid interface for the initial and long-term glass corrosion process by AFM and single-pass flow-through (SPFT) experiments at silica-undersaturated conditions. Freshly broken glass pieces of the International Standard Glass (ISG) and an in-house ternary borosilicate glass (TBG) were *in situ* corroded in a flow-through fluid cell AFM setup with different running solutions. The lack of crystalline order of glass exacerbated the visualization of dissolution features by AFM analysis. However, surface precipitates could be observed *post mortem*, which most likely formed from a supersaturated interfacial fluid layer. Furthermore, flow rate dependent changes in the solution stoichiometry were observed with highly concentrated salt solutions in SPFT experiment with the TBG glass, but not with pure water as experimental solution.

2.2 Methods

2.2.1 Glass synthesis

The TBG glass was synthesized in a platinum crucible at 1400° C for 3 hours from SiO_2, B_2O_3, and Na_2CO_3 powder that was mixed in the proportion to reach a target glass composition of 60 mol% SiO_2, 20 mol% Na_2O, and 20 mol% B_2O_3. The glass was molten a second time after crushing and milling it in a ball mill to ensure chemical homogeneity. After quenching the melt in a pre-heated stainless steel mould, it was tempered at ~560° C for 6 hours, and then letting it cool down by switching off the oven. The International Simple Glass (ISG) is a six-component alumino-borosilicate glass (60.1 mol% SiO_2, 1.7 mol% ZrO_2, 3.8 mol% Al_2O_3, 16.0 mol% B_2O_3, 5.7 mol% CaO, 12.7 mol% Na_2O) developed with the idea of being used as a reference benchmark glass to enable comparability of studies on nuclear waste glass corrosion (Gin et al., 2013b). It was produced in a 50 kg batch by MoSCI Corporation (Rolla, MO, USA) in May 2012 and distributed in 500 g glass ingots.

2.2.2 AFM

In situ experiments were performed using a *Digital Instruments Nanoscope III Multimode* AFM equipped with a fluid cell, and working in contact mode under ambient conditions (20 °C) at the Institute for Mineralogy, University of Münster, Germany. Obtained data was analysed with the *NanoScope Analysis 1.7* software. Glass samples were crushed and suitable, millimetre-sized, ideally flat pieces were selected. In comparison to preparation of minerals, which often hold cleavages and thus enable flat cleaving of faces, the glasses broke in rounded shapes and regularly showed feather-like fractures at the surface. Crushing the glass samples was preferred over (fire-)polishing or other means of sample preparation to not alter the glass surfaces. Samples were checked for suitability with the AFM in air before inserting any solution.

The following solutions were used for the corrosion experiments: distilled water (R $>18\,\Omega\,\mathrm{cm}^{-1}$), HCl (0.1 & 0.01 M), NaOH (0.3 mM & 0.01 M), NaCl (0.5 M), KOH (0.016 mM), and a silica-saturated solution. All but the silica solution were of-the-shelf solutions, only adjusted by dilution with distilled water. The silica solution was prepared by melting KOH with amorphous silica in a ratio of 2:1. The resulting K-silicate was added to distilled water to the amount needed to reach saturation of amorphous silica at room temperature and a pH of 7, which was adjusted by addition of HNO_3. Samples were left in approx. 10 mL of solution post analysis, and revisited the next day. Therefore, sample pieces were taken from the solution and excess water was carefully absorbed with a torn paper tissue. Additionally, surface precipitates were imaged by SEM.

2.2.3 SPFT

For the SPFT experiments, TBG glass coupons of $10 \times 10 \times 1$ mm^3 were cut and polished with 1 µm diamond paste. Coupons were then placed onto sieves in 50 mL polytetraflu-

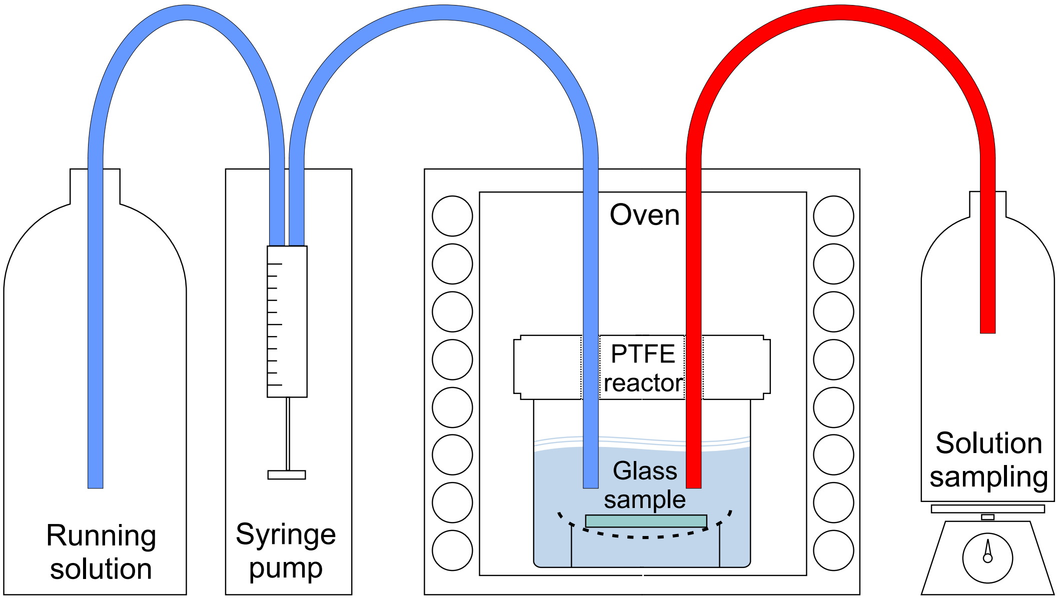

Figure 2.1: Experimental setup of SPFT experiments (visualization not to scale). Fresh running solution on the left is being transferred by syringe pump into sample container located in heated oven (only one of five depicted here), where the glass sample is placed onto a PTFE sieve. With each pump step of fresh solution into the sample container, solution is also transferred to the individual collection container on the right, where the pH and volume are measured manually.

oroethylene (PTFE) containers, which were stored in individual oven chambers at 90 °C and were connected via an in- and outlet with the solution delivering syringe pump system (*J-KEM Scientific* 1400) and individual PET containers for solution collection and later analysis (Fig. 2.1). For each solution, five experiments could be performed in parallel with each outlet delivering a different volume of solution every 60 seconds. As such, average flow rates from 0.5 to 5.0 mL/h were achieved. Solutions were collected over intervals of two to three days, and pH and the solution volume were measured. These volumes were used to correct for the actual flow rates as small discrepancies were noted.

Solution compositions were analysed by inductively-coupled plasma emission spectroscopy (ICP-OES) with an *Thermo Jarrell Ash* Atom Scan 25 at the Institute for Mineralogy, University of Münster, Germany. Solution samples were therefore acidified with HNO_3 and analysed with the following wavelength: boron (249.678 and 249.772 nm), sodium (588.995 and 589.592 nm), and silicon (251.611 and 288.158 nm). The standard deviation estimated from multiple measurements for silicon and boron is $\leq \pm 1\%$.

Surfaces of the corroded glass samples were analysed by optical microscopy, a *TESCAN* VEGA secondary electron microscope (SEM), and a *JEOL* Superprobe JXA-8200 electron microprobe (EMP) attached with an energy-dispersive x-ray detector (EDX) at the Steinmann Institut, University of Bonn, Germany.

2.3 Results

2.3.1 AFM

Reaction with distilled water

The initial surfaces appeared grainy with most samples exhibiting an initial roughness R_q of around 1 nm. After finding a suitable spot, distilled water was first used to cleanse the surface of debris from the crushing process.

Within minutes of contact with distilled water, image signal quality improved and a clear image of the surface could be received. Reaction of the surface is quicker with the TBG glass than with the ISG, but ultimately both glasses reveal the same textural features after some minutes of flushing with distilled water (2 mL flush in-between two images): the surfaces consist of rounded, convex shapes with a diameter of 100-200 nm and a height between 10-20 nm. The initial dissolution of the glass concentrates on minimizing the overall surface roughness and removal of particles on the surface, while general textural features like, e.g., ridges are preserved. When enlarging the tip-scanning-area, it is discernible that the tip or the atomic force between tip and surface influences the reaction behaviour of the scanned glass area. In general, the previously scanned area appeared blurred out. In one particularly flat area of an ISG sample, the dissolution of ridges by segmentation into round sub-units (Fig. 2.4) could be observed. On an ISG sample (Fig. 2.3b), which was submerged in distilled water for 98 h at room temperature and subsequently dried, spheres of 2 µm could be observed by SEM (Fig. 2.5). Thereby the larger sphere itself consists of smaller, about 100 nm-sized spheres. Such colloid aggregates were not directly observed by AFM and thus might be a result of agglomeration of the smaller spheres during drying.

Reactions under alkaline and acidic conditions

After having observed the initial re-equilibration of the glass surface by distilled water, these surfaces of both glasses were subsequently treated with alkaline (NaOH) and/or acidic (HCl) solutions to monitor reaction due to changes in pH. When brought into contact with a NaOH solution with a pH value of 10.5, the previously observed influence of

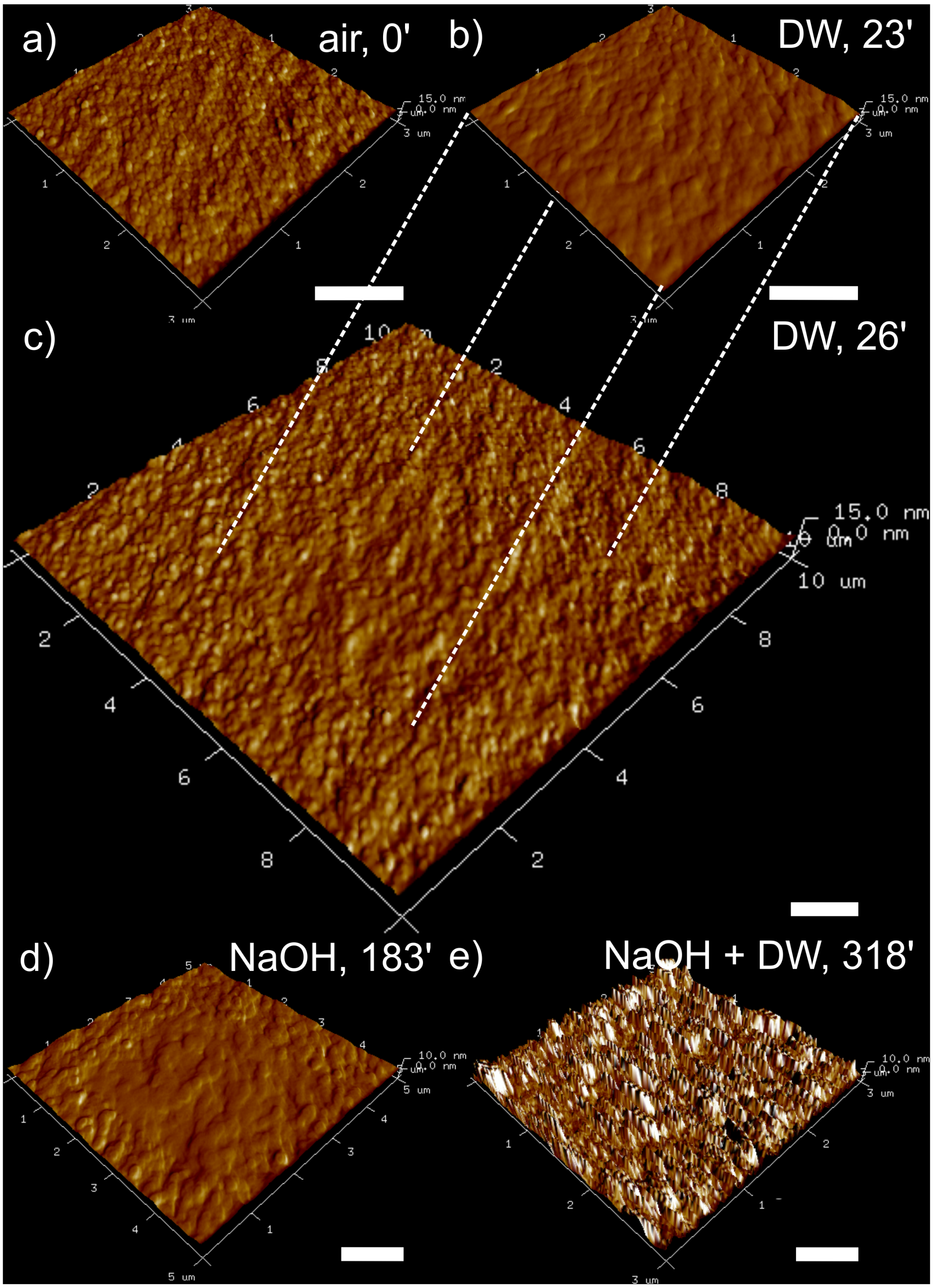

Figure 2.2: AFM images as composites of height map overlain with deflection texture: **a)** Initial broken ISG samples surface appears grainy, **b)** but is smoothed out within minutes in contact with distilled water while continued scanning and intermittent solution renewal. **c)** Enlarging the scanning area reveals that the 'smoothing' must be induced by the atomic forces of the scanning tip of the AFM. **d)** This reaction appears stronger in alkaline conditions, where the sudden addition of distilled water and the consequent lowering of pH results in direct precipitation **(e)**. Scale bars = 1 µm.

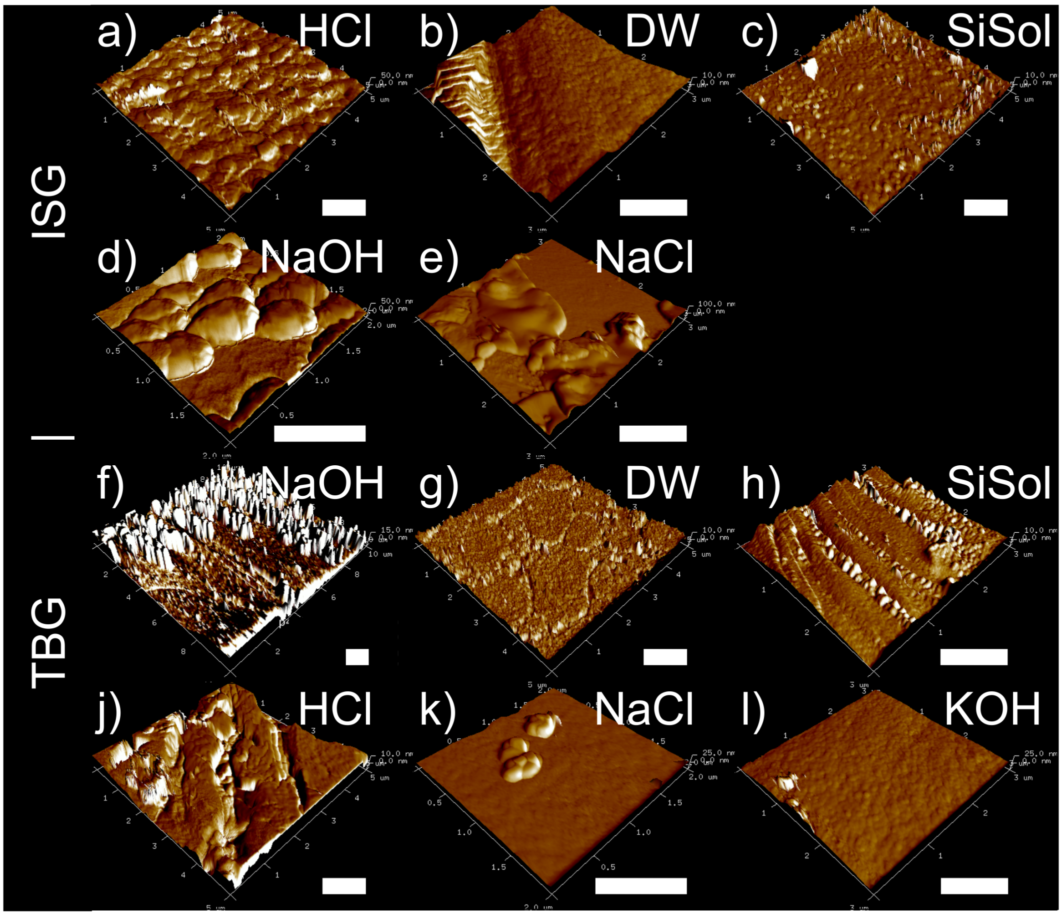

Figure 2.3: Precipitation observed by AFM on ISG (a-e) and TBG (f-l) glass samples. Total time in solution (and pH): ISG - **a)** 3364 h (1.9), **b)** 98 h (5.5), **c)** 99 h (7.0), **d)** 24 h (10.5), **e)** 22 h (5.0, 0.5 *M*); TBG - **f)** 24 h (10.5), **g)** 97 h (5.5), **h)** 98 h (7.0), **j)** 18 h (1.1), **k)** 21 h (5.0, 0.5 *M*), **l)** 18 h (9.2). Scale bars = 1 µm.

the scanning tip onto the surface appeared even more pronounced for the ISG glass. The scanning area appeared to be covered with a blurry layer in contrast to the surrounding surface (Fig. 2.2d), but after the tip was lifted up for ~1.5 h, the first image taken after restarting scanning shows a clear surface consisting of well-defined round sub-units of similar size (Ø = ~100-200 nm). By comparing the height maxima in both images it could be insured that only little x-y-drift occurred in the meantime. In contrast the TBG glass, not only dissolution but also precipitation below the previously scanned area was observed after zooming out. The precipitates seemed to be rather fragile, as they are dragged along by the tip in the continuing scans. No further characterization was possible due to the small size and instability. The ISG is by design more corrosion resistant than the TBG glass. Hence, the pH was increased to 12, which lead to enhanced dissolution depicted by a stronger relief of the surface. The round sub-units were more isolated and revealed a plateau-like appearance. Furthermore, the tip influence is more intense as seen by an increased contrast between continuously scanned areas and their surroundings (Fig. 2.2d). Similar to previous observations with the TBG glass, fine (re-)precipitation can be seen at higher pH, which mostly appears as noisy signal in the adjacent area around the primarily scanned area as the tip's interaction forces prevent precipitation underneath it. However, precipitation could also be forced by injection of distilled water, drastically lowering the pH level and overreaching silica saturation this way (Fig. 2.2e). As before, the precipitates are too small for detailed characterization and were dragged along the surface by the tip. Congruent glass dissolution is to be expected in solutions with pH levels above 10 due to the higher silica solubility. Hence, both glasses were treated with a less alkaline solution of KOH (pH = 9.2). KOH was chosen for direct comparisons with other experimental data sets (not shown here). In contrast to the plateau-like appearance at pH 9.2, subunits of the surface appeared to be more rounded (again) and the surface to have less distinct relief.

Both glass samples were also treated with HCl to test the reaction in the low pH range, where silica solubility is low and silica surface negativity is compensated by free H^+ from solution (isoelectric point at a pH value of ∼2), which generally revealed similar surfacial features.

Salt and silica solutions

In comparison to the previous tested solutions, the TBG glass and the half-saturated salt solution (0.5 *M* NaCl) shows similar reaction affinity (tip sensitive in the beginning), while the subunit size appeared in the end rather large and flat (300 µm). Unexpectedly, the sample revealed a homogeneously rough surface the next day (Fig. 2.3k), with only a few precipitated droplets. With the ISG glass, no other surface reactions than the initial surface reconfiguration and smoothing could be observed. Both glass types were also treated with silica-saturated solution at pH 7. For the TBG glass, after 20 min, sporadic precipitates in the shape of small droplets were observed, but in general the image quality was quite noisy. The ISG samples revealed no new significant observations. Both samples were left in solution for four nights. The TBG samples showed afterwards more sporadic precipitation of little roundish lumps, especially at feather-like cracks (Fig. 2.3h) in comparison to the samples treated with distilled water. The ISG

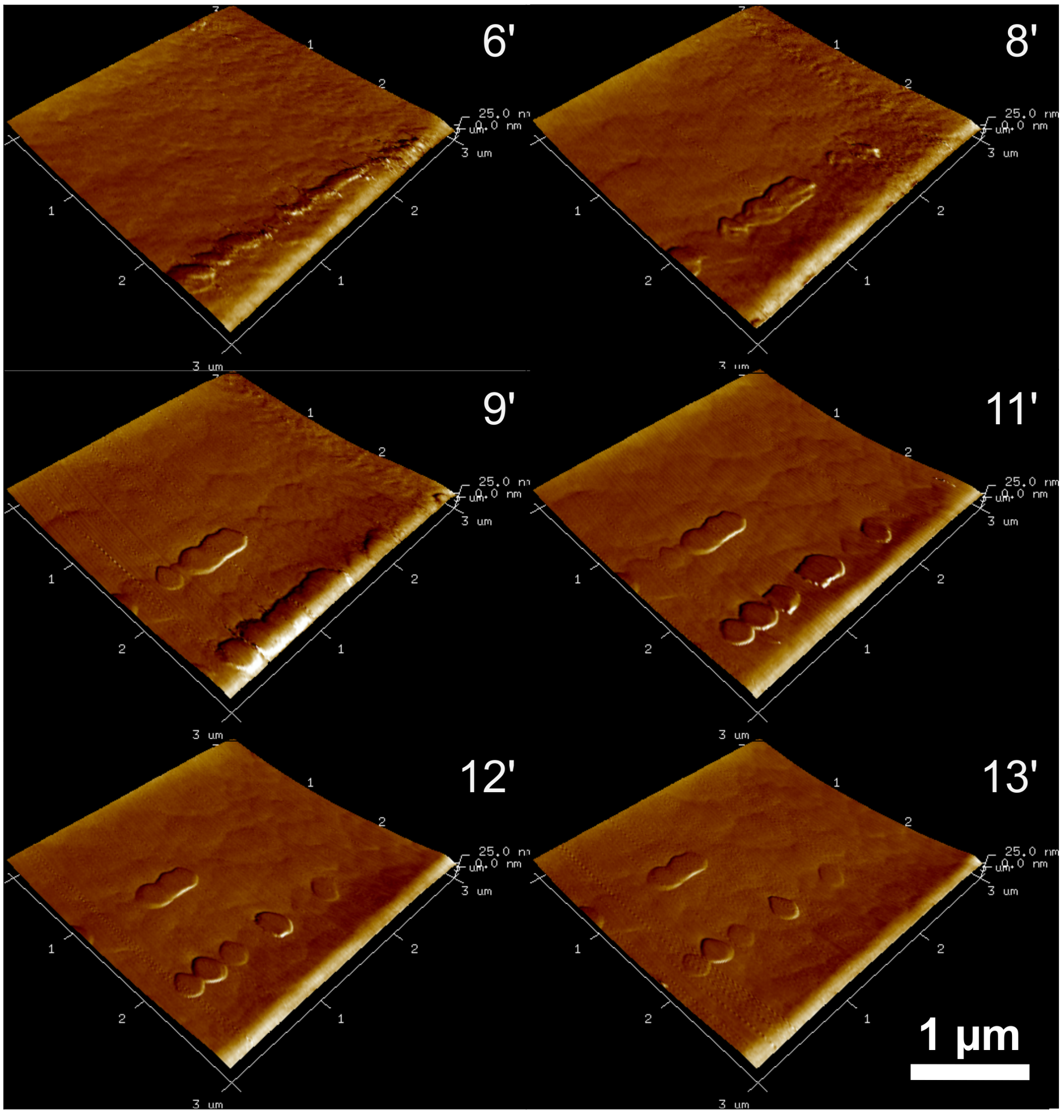

Figure 2.4: Rearrangement and dissolution of ridge structures on ISG glass sample in distilled water.

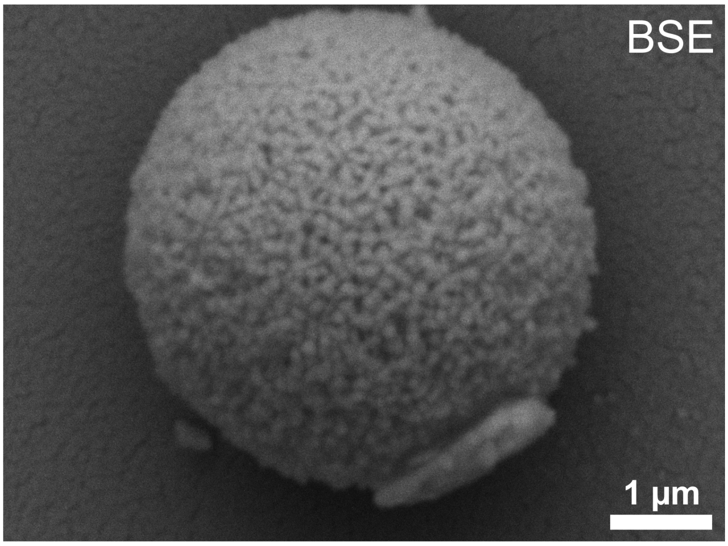

Figure 2.5: SEM image of colloid aggregate of amorphous silica consisting of smaller spheres observed on dried ISG sample, which was submerged in distilled water for 98 h at room temperature.

sample shows less precipitation in shape of lumps, but a rather droplet-like surface with some lumps (Fig. 2.3c).

Thus, in general it can be said that all fresh surfaces of the glasses show an immediate reaction of surface reconfiguration when brought into contact with distilled water. Furthermore, the tip interaction has a significant effect on the apparently unstable surface of the scanned area of interest. Over the course of the experiments, initially grainy and rough surfaces are smoothed out with rounded, convex features ('subunits') characterizing the surface. Precipitates are for once observed as material transported by the tip at the edges of the scanning area as well as by lowering the silica solubility by pH changes during the experiment. Most pronounced and divers are precipitates after longer contact time between solution and glass samples and subsequent solution removal (Fig. 2.3). The amount and shape of the precipitates change with the solution composition, saturation, and pH as it strongly influences silica precipitation (Iler, 1979).

2.3.2 SPFT

Single-pass flow-trough experiments were conducted with the less corrosion resistant TBG glass in distilled water and concentrated salt solutions (13.3 and 26.5 wt% NaCl solutions) to further investigate the existence and potential effect of a fluid boundary layer at the

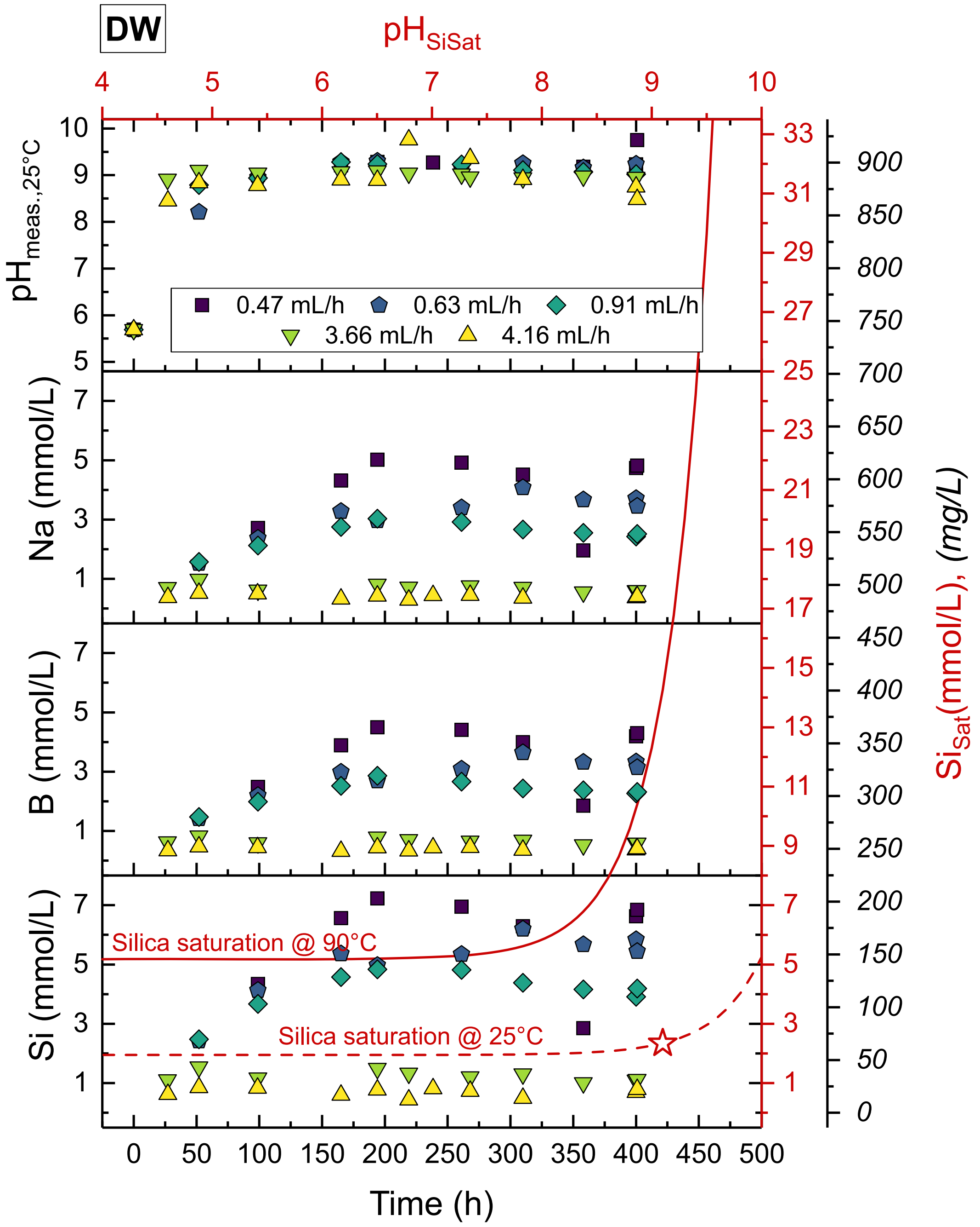

Figure 2.6: Evolution of pH (measured at room temperature), and sodium, boron and silicon in solution over time in the DW experiment (as analysed by ICP-OES). Flow rates are corrected for measured throughput. Silicon concentrations for saturation with respect to amorphous silica and pH (red axes) given for 25 °C (dashed line) and 90 °C (bold line) were calculated with PHREEQC (Parkhurst and Appelo, 2013) and the standard interaction theory database (SIT). Star marks the corresponding silicon saturation concentration for the average bulk pH.

glass surface during borosilicate glass corrosion. The AFM experiments allowed making observations of initial surfacial reactions at the nanoscale. The SPFT experiment were designed to investigate two questions: (1) Is the dissolution congruent or not?, and (2) whether silica will precipitate at the dissolution surface despite steady solution renewal that keeps the bulk solution undersaturated with respect to amorphous silica.[1]

The evolution of pH and concentrations of sodium, boron, and silicon over the time of the experiment appears to be well in accordance with results of similar experiments with other glasses (e.g., see Icenhower et al., 2008): The concentration of glass components increased initially, but after about 200 hours a steady state between element input by glass dissolution and removal by solution renewal was established (see Fig. 2.6). The change in pH, mainly caused by the release of sodium from the glass into solution, followed this trend accordingly. Noticeably, a steady state seems to have been reached for the experiments run at high flow rates (3.66 and 4.16 mL/h) immediately after the start of the experiment. In general, it can be said that the lower the flow rate, the higher is the concentration of glass components in solution. Comparing silicon and boron concentrations against each other (Fig. 2.9), it appears that the corrosion of the TBG glass with distilled water is congruent, meaning the solution reveals the same stoichiometry as the pristine glass. As changes in the sodium concentration could not be measured against the high NaCl concentrations of the brines in the following experiments, the Si/Na or B/Na ratios are not shown here, but they also show the same congruency.

Results of the two experimental series with highly concentrated salt solution appear similar to those of the distilled water experiments with high flow rates ($\geq$ 4 mL/h) (see Figs. 2.7 and 2.8), with the only difference being that the concentrations measured in the collected solution are lower by a factor of about two. Naturally, the millimolar changes in sodium concentrations over time due to glass dissolution could not be measured by ICP-OES against the high sodium chloride contents of the running solutions. Nonetheless, the evolution of pH reveals a steady state for the NaCl-13 solution experiment already from the beginning of the experiment and a minimal increase over time for the NaCl-27 solution (applies to all flow rates). Furthermore, the Si/B ratios measured in solution have again the same stoichiometry as the pristine glass (see insets Fig. 2.9).

In contrast to the described experiments in distilled water (all flow rates) and the high flow rate experiments with the concentrated salt solutions, a divergence from the stoi-

---

[1] *The presented experimental data here were obtained under personal supervision of a master's thesis (Gref, 2014).*

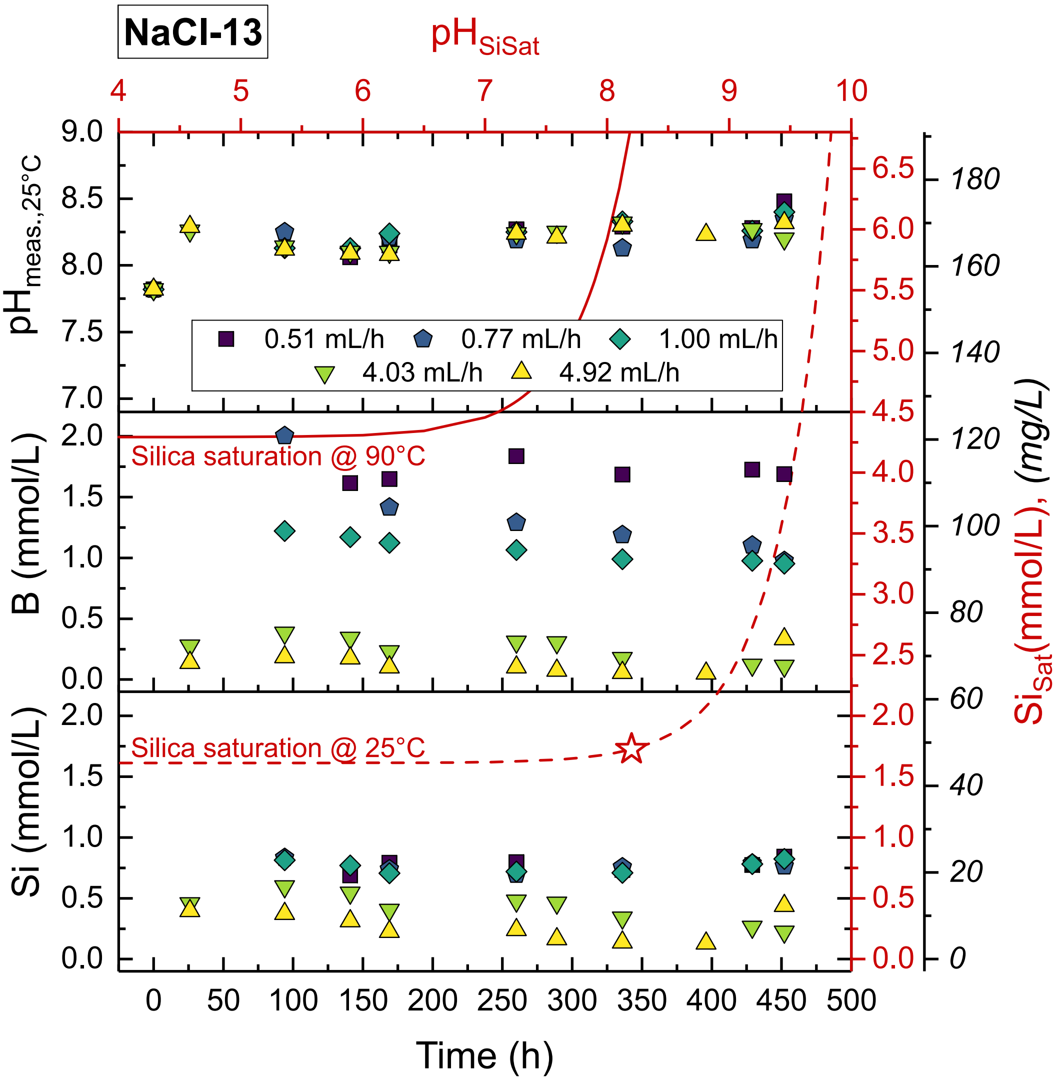

Figure 2.7: Evolution of pH (at room temperature), boron and silicon in solution over time in the NaCl-13 experiment (as analysed by ICP-OES). Flow rates are corrected for measured throughput. Silicon concentrations for saturation with respect to amorphous silica and pH given for 25 °C (dashed line) and 90 °C (bold line) were calculated with PHREEQC (Parkhurst and Appelo, 2013) and the standard interaction theory database (SIT). Star marks the corresponding silicon saturation concentration for the average bulk pH.

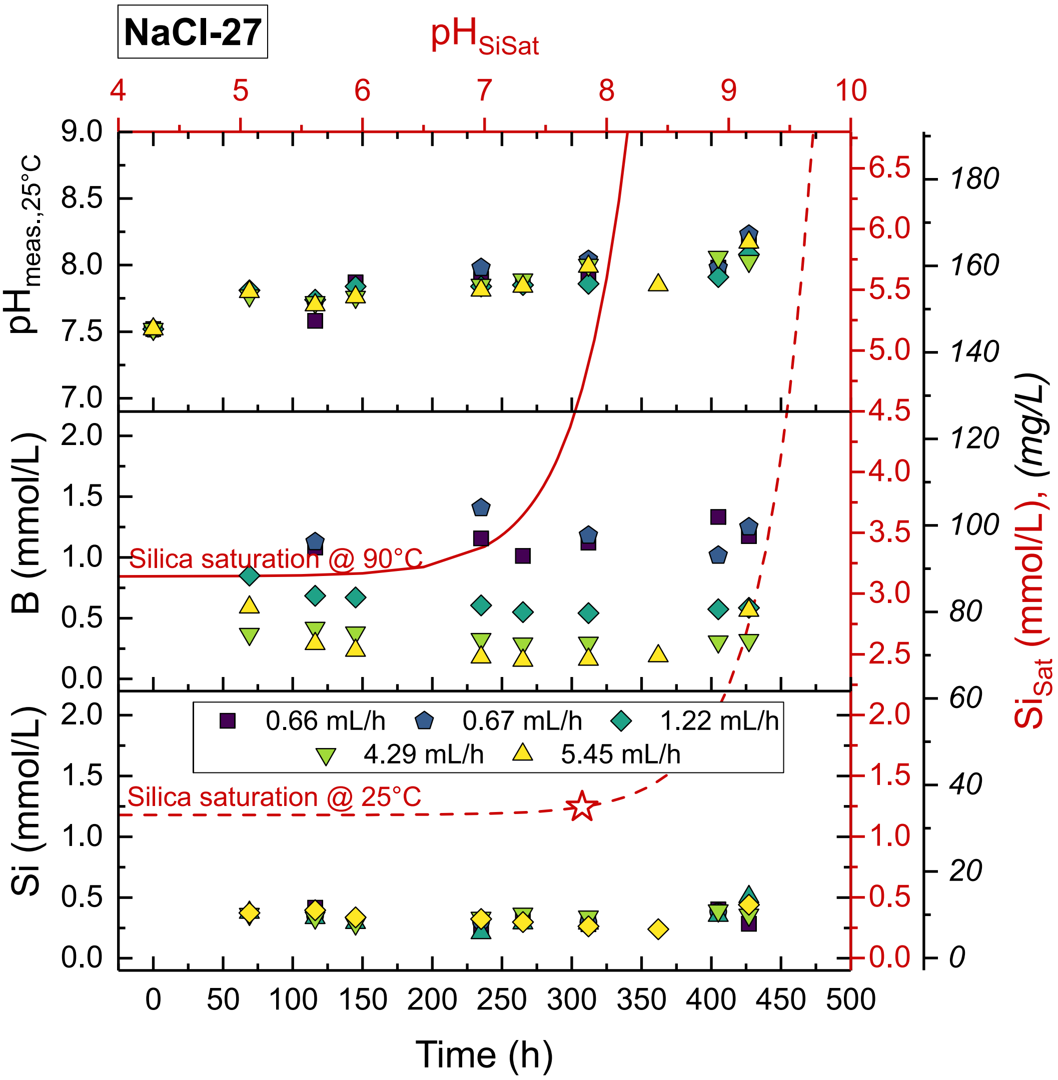

Figure 2.8: Evolution of pH (at room temperature), boron and silicon in solution over time in the NaCl-27 experiment (as analysed by ICP-OES). Flow rates are corrected for measured throughput. Silicon concentrations for saturation with respect to amorphous silica and pH given for 25 °C (dashed line) and 90 °C (bold line) were calculated with PHREEQC (Parkhurst and Appelo, 2013) and the standard interaction theory database (SIT). Star marks the corresponding silicon saturation concentration for the average bulk pH.

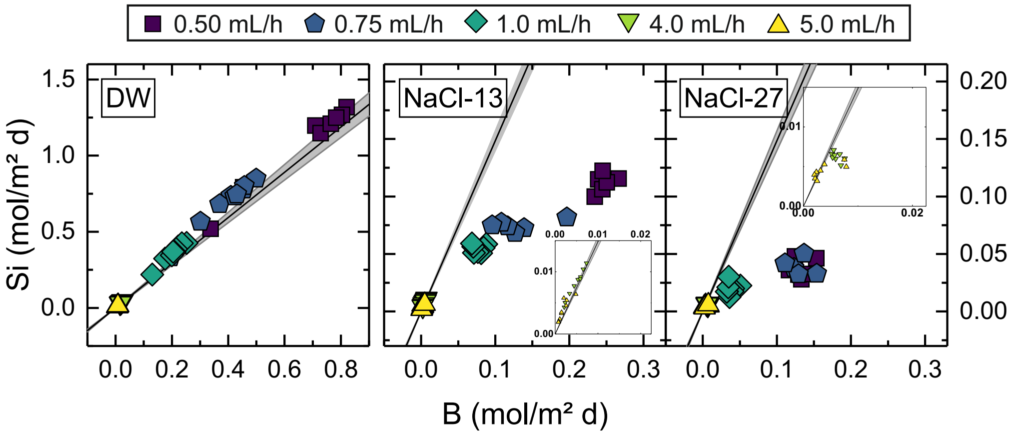

Figure 2.9: Silicon vs boron content in solution in comparison to stoichiometry of initial TBG glass. Running solution: distilled water (left), NaCl13 (centre), NaCl27 (right). Concentrations were corrected for the geometrical surface areas of the individual sample coupons. Linear (black line) represents stoichiometry of initial glass, grey area indicates standard deviation (N≥100) of analysis by (WDX-)EMP. Nominal flow rates are given.

chiometry of the pristine glass was measured in solutions from both salt solution experiments at lower flow rates (see Fig. 2.9). For the NaCl-13 solution, the Si/B ratios of the low flow rate runs reveal a systematic lack of silicon in comparison to the composition of the pristine glass (avg. $Si/B_{solution}$: 0.32 ± 0.02, Si/B_{glass}: 1.48 0± 0.08). The average Si/B ratio of the NaCl-27 experiments (0.17 ± 0.03) is also below the ratio of the pristine glass. Bulk silica saturation of the concentrated salt solutions can be ruled out as reason for the apparent incongruency of the corrosion process at lower flow rates, as silica saturation was not reached, neither at experimental conditions nor at room temperature (cf. Figs. 2.7 and 2.8). However, for all flow rates, silicon concentrations (as well as boron concentrations and pH) were lower for experiments run in concentrated salt solutions than those run in distilled water, indicating that NaCl reduces the corrosion kinetics. This observation stands in contrast to similar experiments run by Icenhower & Dove (2000), where the introduction of solutions with 0.3 wt% NaCl (= 0.05 molal) enhanced the corrosion by a factor of 21.

Looking at the surfaces *post mortem* by naked eye, all samples appeared slightly milky, less translucent and exhibited opalescence. Samples of the NaCl-13 and NaCl-27 runs were rewashed with distilled water after drying, because salt crystals were still found on

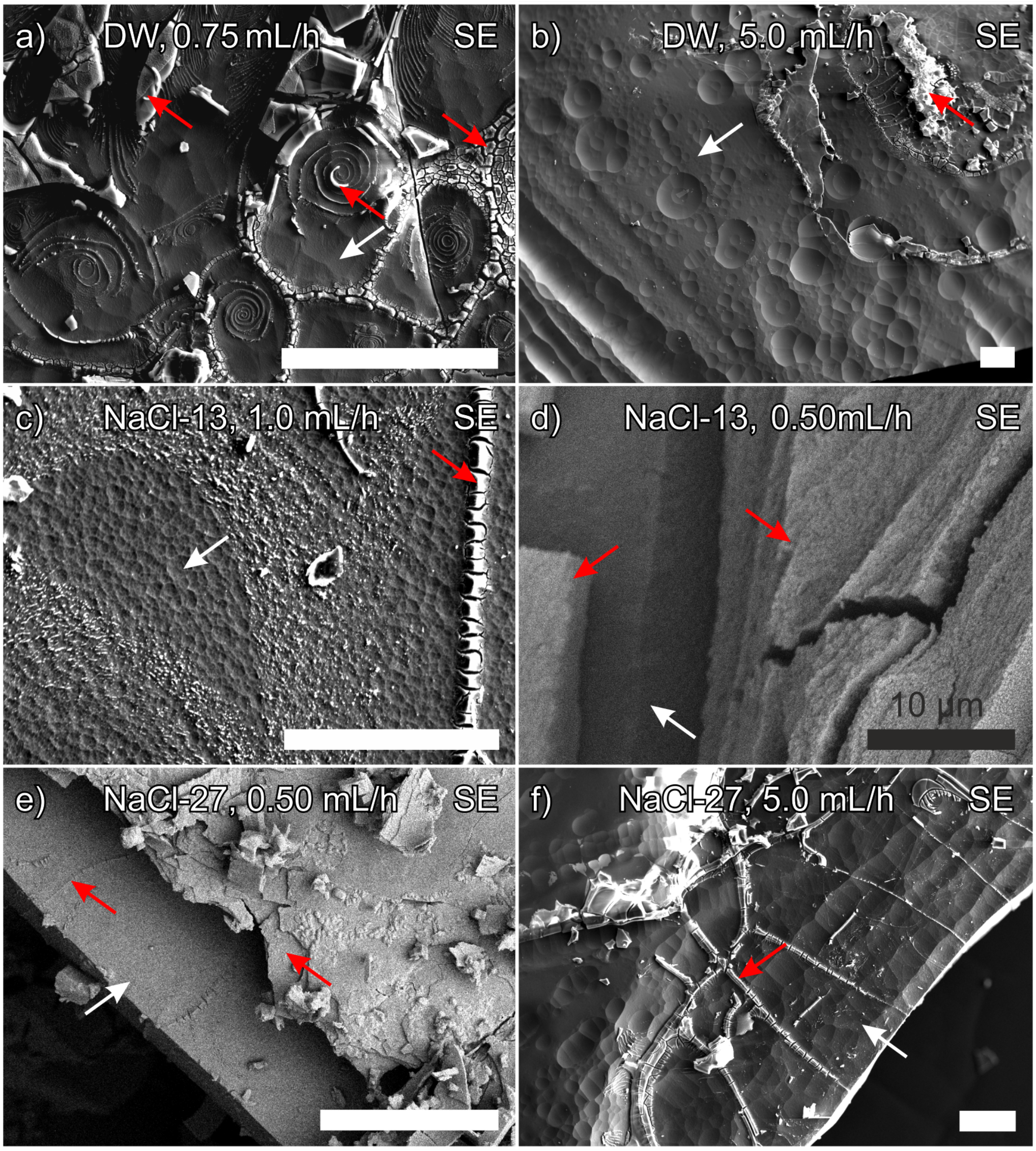

Figure 2.10: Secondary electron images of surfaces of corroded glass samples. Red arrows denote silica analysed by EDX, white arrows point to sodium-bearing glass. (White) Scale bars = 200 µm. The specific formation mechanism of the spiral shapes in a) is unclear, but might be a drying effect.

the surface. Overall, the corrosion layer appeared brittle and detached easily from the underlying glass. Observation by SEM and EMP analysis revealed extensive rounded etch pits of varying diameter on the surfaces (see Fig. 2.10), which resemble those found on experimentally altered ternary borosilicate glass samples (Geisler et al., 2015). While most etch pits occur seemingly randomly at the surface, some reproduce former elongated scratches from the grinding and polishing process (see Fig. 2.10b). Silica was identified by EDX analysis on most samples (see red arrows in Fig. 2.10), where the corrosion layer was preserved. It can cover the whole surface, but also forms intriguing features in direct contact with the corroded glass surface, e.g. spirals (Fig. 2.10a) or spine-like structures (Fig. 2.10e/f). The latter were also observed in the AFM experiments (see Fig. 2.3b).

2.4 Discussion

From the results of both the AFM and SPFT experiments, the following observation can be made: (1) glass corrosion stars immediately after the glass has come into contact with water, (2) silica precipitation occurs under (nominally) undersaturated conditions with respect to the bulk solution, and (3) a non-stoichiometric solution composition was observed hat depends on the flow rate.

Both types of glass, the simple ternary borosilicate glass and the more corrosion-resistant, six component ISG immediately reacted in contact with distilled water, whereby the initially rough surface was smoothed out. From enlarging the scanning area, it is obvious that the tip of the cantilever is caused unintended interactions with the reacting surface. However, although this is an artefact of the analytical technique, it reveals how sensitive the glass surface is when in contact with water. Such reaction was not observed during the initial dry scanning of the samples. Within the ongoing discussion about the underlying reaction mechanism of borosilicate glass (for nuclear waste disposal), the soft surface can be interpreted in several ways: (1) a so-called leached glass is supposedly undergone ion-exchange reactions resulting in hydrolysis of the glass, forming a gel-like phase (e.g., Frugier et al., 2008; Rebiscoul et al., 2004). As a result, the tip could, by scanning across the surface, have rearranged the weakly bonded gel phase. within the framework of the dissolution-precipitation-based corrosion model (Geisler et al., 2010; Geisler et al., 2015; Hellmann et al., 2015; A. Putnis, 2015), the tip forces could have easily rearranged the precipitated amorphous silica within the scanned area. Which of the model represents the glass replacement reaction taking place here, cannot conclusively be stated on basis of the AFM observation. However, it should be noted that precipitation at the surface was observed at several stages of these experiments.

The precipitates observed by AFM are interpreted to be amorphous silica for several reasons: (1) SiO_2 is the major component in all glasses, but (2) has a low solubility in acidic to mildly alkaline conditions, in contrast to (3) sodium and boron; (4) formation of silica spheres as observed by SEM (Fig. 2.5). However, for the ISG glass, minor amounts of zirconium and aluminium-based precipitates cannot be ruled out. Considering that the glass samples for the AFM experiments were rather small (< 4 mm in diameter, < 1 mm thick) and the experiments were conducted at room temperature with regular solution renewal, saturation of the bulk solution with respect to amorphous silica can be ruled out as well. For the SPFT experiments, only at low flow rates in the distilled water experiments, silica saturation might have been reached during the course of the experiment. However, as the pH could only be measured at the outlet at room temperature, the exact pH at running conditions and therefore the level of saturation can only be estimated. At high flow rates and in the salt solutions, silica saturation was not reached. Nonetheless, silica precipitation was observed in both experimental setups. Thus, an explanation for how silica can precipitate in undersaturated conditions is needed. Setting the discussion about the underlying corrosion mechanism aside for a moment, a similar reasoning is required for the ion exchange and hydrolysis-driven model (Frugier et al., 2008). In this model the stability of *in situ* formed, silica-rich gel phase in undersaturated conditions must be explained. The observed change in solution stoichiometry within the two salt solution SPFT experiments provides some evidence. As already stated, the stoichiometry of the solution composition matches that of the glass composition for the runs with distilled water for all flow rates and also for the high flow rates of the salt solution runs Fig. 2.9. However, at lower flow rates the solutions are systematically lacking silicon. While pH is overall lower for the salt solutions, indicating a lower sodium release and as such a slower corrosion rate in these solutions, major differences in pH between flow rates could not be detected. And as silicon concentrations are low enough, bulk solution saturation can also not explain the lack of silicon at these flow rates.

Ruiz-Agudo and co-workers (2016) have conducted static and flow-through experiments to study the replacement of silicates during weathering by using wollastonite as an example. Although, wollastonite is a crystalline mineral phase and not an amorphous glass, but the weathering (or corrosion) product is also an amorphous silica-rich layer. Using a Mach-Zehnder phase-shift interferometer and micro-electrodes for *in situ* pH and Ca^+ measurements, the authors could show experimentally that for stagnant solution conditions strong concentration gradients between the solution-solid interface and the bulk solution develop. Under stagnant conditions, transport of dissolved species is limited to diffusion, which allows for local supersaturation at the solution-solid interface, triggering the reprecipitation of the least soluble species, i.e., amorphous silica. Note that quartz is expected to precipitate from a thermodynamical view, but amorphous silica is kinetically favoured. The result of such a small-scale, local supersaturation and reprecipitation of amorphous silica is that on the macro-scale the overall reaction will appear to be incongruent dissolution, not an interface-coupled dissolution and precipitation process. Without the *in situ*, small-scale observation, the formulation of the reaction mechanism solely hinges on bulk solution analysis and the *post-mortem* examination of the altered solid. Traditionally, altered, silica-rich surfaces on silicates such as wollastonite were thus (falsely) interpreted to be leached layers (e.g., Casey et al., 1993). If *leaching*, i.e., ion exchange, hydralization of the crystalline material, and later restructuring, is obviously not responsible for the formation of silica-rich alteration layers for mineral phases, then the same should be plausible for amorphous systems showing the same alteration/corrosion product. The dissolution kinetics and mechanics might slightly differ between crystalline and amorphous material as long-ranged ordered crystal surfaces dissolve at high-energy kink or step sites, which a glass does not provide. On the other side, glass does not form perfectly (flat), low-energy crystal terraces, but will rather have a rumbled surface (Dove et al., 2008). Additionally, glass will contain residual strain from the quenching process, which further increases its reactivity.

Thus far, concentration gradients were shown for stagnant conditions, where mass transport is limited to diffusion through the solution, but not for (very) high flow rates (up to 120 mL/h) (Ruiz-Agudo et al., 2016). The occurrence of a strong concentration gradient enabling local supersaturation is depending on the interplay between dissolution rate and rate of mass transport/removal (by diffusion or flow). Experiments performed in this study range from stagnant to high flow regimes (5 mL/h). Solution analyses of the SPFT experiments revealed thereby a transition between congruent (at high flow rates) and apparently incongruent dissolution (at low flow rates) in the salt solution series. It seems thus plausible to argue that if flow rates are low enough that mass transport by diffusion becomes dominant, a strong concentration gradient between the corroding glass surface and bulk solution should have emerged, forming a solution boundary layer. A change in the flow regime, from laminar flow at low rates to turbulent flow at higher flow rates, seems to be a plausible cause for the disruption of the concentration gradient. However, the experimental setup used here is only a mixed flow design without continuous flow. Instead, the syringe pump inserts individual amounts of solution in regular intervals to achieve the overall renewal rates. As such, strong flow pulses may cause short-time turbulent flow within the reactor, whereas the concentration gradients between glass surface and bulk solution are undisturbed by weak pulses of the lower flow rates.

For such hypersaline solution, it was shown by isotope tracer experiments with $H_2{}^{18}O$, using Dead Sea water composition, that in such solutions self-diffusion of water is about 25% lower at ambient temperatures (Yechieli and Ronen, 1996). Kowacz and co-workers (2010) - working on the effect of different background electrolytes on the formation of barite - stated that at high electrolyte concentration, the high affinity of water to solvent molecules (other ions, e.g., Na^+ and Cl^-) affect the bulk solvent structure dynamics such that water will be less mobile and less prone to hydrate solutes like, in this case, silicic acid ($Si(OH)_4$). This, in turn, slows down the diffusional transport of dissolved silica allowing local supersaturation at the corroding glass interface. Hence, on one side the salt in solution is slowing down the overall reaction rate (see pH and B concentrations, Fig. 2.6-2.8), but on the other side it also enables the build up of strong concentration gradients at the glass interface by suppression of mass transport. Additionally, an increase in salt concentration in solution lowers the sol stability and gel time for amorphous silica (Iler, 1979), meaning that polymerization and precipitation of amorphous silica is favoured in highly concentrated salt solutions. Nonetheless, if flow rates are high (or strong) enough, this interfacial fluid layer might be disturbed, and silica saturation will not be reached. Once a sufficient layer of amorphous silica has been precipitated on the glass surface, the transport properties of the (nano-)porous material control the corrosion rate and thus the element release (Geisler et al., 2015).

Of course, it can be argued that strong concentration gradients (specifically for silicic acid) at low flow rates diminish the affinity for silicon dissolution from the glass network, thus ion exchange and hydration of the glass network could become dominant (Van Iseghem and Grambow, 1987; Frugier et al., 2008). In that case, the silica-rich surface layers would resemble a so-called residual glass, which formed from the *in situ* reconstruction of the chemically leached gel phase. However, this would imply that initially enough silicon was released into the nearby solution (by congruent dissolution), but not wholly transported into the bulk solution to establish a strong concentration gradient, and that this gradient is maintained stable over time by further release of silicon from the glass network.The implications of these findings for the long-term disposal of high-level nuclear waste in a borosilicate glass matrix are two-fold. First, the precipitation of amorphous silica in undersaturated conditions enabled by the implied concentration gradients underpins a corrosion mechanism controlled by interface-coupled dissolution-reprecipitation (Geisler et al., 2010; Geisler et al., 2015; Hellmann et al., 2015; A. Putnis, 2015). Secondly, specifically the results of the salt solution experiments are relevant for one of the possible (German) geological disposal scenarios, the storage of vitrified nuclear waste in salt formations. In the worst case scenario of a groundwater breach, the high salt concentrations in solution will lower the overall silica solubility and mobility, promoting the quick formation of amorphous silica-rich corrosion layers, which, in turn, then controls the corrosion progress and ultimately slows it down (Geisler et al., 2015).

2.5 Conclusions

The dual approach by AFM and SPFT experimental corrosion of glasses delivered strong evidence for a significant compositional difference between the interfacial and bulk solution, influencing the overall corrosion progress. The implied development of concentration gradients can explain the observed precipitation of amorphous silica under nominally undersaturated conditions (in the bulk solution). It further diminishes the need for two different reaction mechanisms (congruent dissolution and ion exchange coupled with *in situ* reconstruction of a 'leached' gel phase) to explain both congruent and (apparently) incongruent dissolution behaviour of the same glass at different conditions. Congruent dissolution of the glass with subsequent precipitation of amorphous silica at the reaction interface (as proposed by Geisler and co-workers (2010; 2015)) also allows to unify the corrosion of glass with aqueous alteration and replacement reactions observed in crystalline system (Hellmann et al., 2012; A. Putnis, 2015).

2.6 References

Casey, W. H., H. R. Westrich, J. F. Banfield, G. Ferruzzi, and G. W. Arnold (1993). “Leaching and Reconstruction at the Surfaces of Dissolving Chain-Silicate Minerals”. In: *Nature* 366, p. 253.

Dohmen, L., C. Lenting, R. O. C. Fonseca, T. Nagel, A. Heuser, T. Geisler, and R. Denkler (2013). “Pattern Formation in Silicate Glass Corrosion Zones”. In: *International Journal of Applied Glass Science* 4.4, pp. 357–370. ISSN: 20411286. DOI: `10.1111/ijag.12046`.

Dove, P. M., N. Han, A. F. Wallace, and J. J. De Yoreo (2008). “Kinetics of Amorphous Silica Dissolution and the Paradox of the Silica Polymorphs”. In: *Proceedings of the National Academy of Sciences* 105.29, pp. 9903–9908.

Frugier, P. et al. (2008). “SON68 Nuclear Glass Dissolution Kinetics: Current State of Knowledge and Basis of the New GRAAL Model”. In: *Journal of Nuclear Materials* 380.1-3, pp. 8–21. ISSN: 00223115. DOI: `10.1016/j.jnucmat.2008.06.044`.

Geisler, T., A. Janssen, D. Scheiter, T. Stephan, J. Berndt, and A. Putnis (2010). “Aqueous Corrosion of Borosilicate Glass under Acidic Conditions: A New Corrosion Mechanism”. In: *Journal of Non-Crystalline Solids* 356.28-30, pp. 1458–1465. ISSN: 00223093. DOI: `10.1016/j.jnoncrysol.2010.04.033`.

Geisler, T., T. Nagel, M. R. Kilburn, A. Janssen, J. P. Icenhower, R. O. Fonseca, M. Grange, and A. A. Nemchin (2015). “The Mechanism of Borosilicate Glass Corrosion Revisited”. In: *Geochimica et Cosmochimica Acta* 158, pp. 112–129. ISSN: 00167037. DOI: `10.1016/j.gca.2015.02.039`.

Gin, S. (2014). “Open Scientific Questions about Nuclear Glass Corrosion”. In: *Procedia Materials Science* 7, pp. 163–171. ISSN: 22118128. DOI: `10.1016/j.mspro.2014.10.022`.

Gin, S., J. Ryan, D. Schreiber, J. Neeway, and M. Cabié (2013a). “Contribution of Atom-Probe Tomography to a Better Understanding of Glass Alteration Mechanisms: Application to a Nuclear Glass Specimen Altered 25years in a Granitic Environment”. In: *Chemical Geology* 349-350, pp. 99–109. ISSN: 00092541. DOI: `10.1016/j.chemgeo.2013.04.001`.

Gin, S. et al. (2013b). “An International Initiative on Long-Term Behavior of High-Level Nuclear Waste Glass”. In: *Materials Today* 16.6, pp. 243–248. ISSN: 13697021. DOI: `10.1016/j.mattod.2013.06.008`.

Gin, S. et al. (2017). “Atom-Probe Tomography, TEM and ToF-SIMS Study of Borosilicate Glass Alteration Rim: A Multiscale Approach to Investigating Rate-Limiting Mechanisms”. In: *Geochimica et Cosmochimica Acta* 202, pp. 57–76. ISSN: 00167037. DOI: `10.1016/j.gca.2016.12.029`.

Gin, S., P. Jollivet, M. Fournier, F. Angeli, P. Frugier, and T. Charpentier (2015a). “Origin and Consequences of Silicate Glass Passivation by Surface Layers”. In: *Nature Communications* 6, p. 6360. ISSN: 2041-1723. DOI: `10.1038/ncomms7360`.

Gin, S., P. Jollivet, M. Fournier, C. Berthon, Z. Wang, A. Mitroshkov, Z. Zhu, and J. V. Ryan (2015b). “The Fate of Silicon during Glass Corrosion under Alkaline Conditions: A Mechanistic and Kinetic Study with the International Simple Glass”. In: *Geochimica et Cosmochimica Acta* 151, pp. 68–85. ISSN: 00167037. DOI: `10.1016/j.gca.2014.12.009`.

Grambow, B. (2006). “Nuclear Waste Glasses - How Durable?” In: *Elements* 2.6, pp. 357–364. DOI: `10.2113/gselements.2.6.357`.

Gref, E. (2014). “Bestimmung Der Vorwärtsauflösungsraten von Borosilikatgläsern Mithilfe von Durchflussexperimenten”. Master thesis. Bonn: Bonn. 68 pp.

Hellmann, R., S. Cotte, E. Cadel, S. Malladi, L. S. Karlsson, S. Lozano-Perez, M. Cabié, and A. Seyeux (2015). “Nanometre-Scale Evidence for Interfacial Dissolution–Reprecipitation Control of Silicate Glass Corrosion”. In: *Nature Materials* 14.3, pp. 307–311. ISSN: 1476-1122, 1476-4660. DOI: `10.1038/nmat4172`.

Hellmann, R., R. Wirth, D. Daval, J.-P. Barnes, J.-M. Penisson, D. Tisserand, T. Epicier, B. Florin, and R. L. Hervig (2012). “Unifying Natural and Laboratory Chemical Weathering with Interfacial Dissolution–Reprecipitation: A Study Based on the Nanometer-Scale Chemistry of Fluid–Silicate Interfaces”. In: *Chemical Geology* 294-295, pp. 203–216. ISSN: 00092541. DOI: `10.1016/j.chemgeo.2011.12.002`.

Icenhower, J. P. and P. M. Dove (2000). “The Dissolution Kinetics of Amorphous Silica into Sodium Chloride Solutions: Effects of Temperature and Ionic Strength”. In: *Geochimica et Cosmochimica Acta* 64.24, pp. 4193–4203.

Icenhower, J. P., B. P. McGrail, W. J. Shaw, E. M. Pierce, P. Nachimuthu, D. K. Shuh, E. A. Rodriguez, and J. L. Steele (2008). “Experimentally Determined Dissolution Kinetics of Na-Rich Borosilicate Glass at Far from Equilibrium Conditions: Implications for Transition State Theory". In: *Geochimica et Cosmochimica Acta* 72.12, pp. 2767–2788. ISSN: 00167037. DOI: 10.1016/j.gca.2008.02.026.

Iler, R. K. (1979). *The Chemistry of Silica: Solubility, Polymerization, Colloid and Surface Properties and Biochemistry of Silica.* John Wiley & Sons. 896 pp. ISBN: 978-0-471-02404-0.

Kowacz, M., M. Prieto, and A. Putnis (2010). "Kinetics of Crystal Nucleation in Ionic Solutions: Electrostatics and Hydration Forces". In: *Geochimica et Cosmochimica Acta* 74.2, pp. 469–481.

McLoughlin, S. D., N. C. Hyatt, R. J. Hand, and W. E. Lee (2006). "Corrosion of Archaeological Model Glasses after 32 Years of Burial at Ballidon". In: *MRS Proceedings.* Vol. 932. Cambridge Univ Press, pp. 1–1.

Parkhurst, D. L. and C. Appelo (2013). *Description of Input and Examples for PHREEQC Version 3: A Computer Program for Speciation, Batch-Reaction, One-Dimensional Transport, and Inverse Geochemical Calculations.* US Geological Survey.

Putnis, A. (2002). "Mineral Replacement Reactions: From Macroscopic Observations to Microscopic Mechanisms". In: *Mineralogical Magazine* 66.5, pp. 689–708. ISSN: 14718022, 0026461X. DOI: 10.1180/0026461026650056.

Putnis, A. (2015). "Sharpened Interface". In: *Nature Materials* 14, p. 261.

Putnis, A. and C. V. Putnis (2007). "The Mechanism of Reequilibration of Solids in the Presence of a Fluid Phase". In: *Journal of Solid State Chemistry* 180.5, pp. 1783–1786. ISSN: 00224596. DOI: 10.1016/j.jssc.2007.03.023.

Rebiscoul, D., A. Van der Lee, F. Rieutord, F. Né, O. Spalla, A. El-Mansouri, P. Frugier, A. Ayral, and S. Gin (2004). "Morphological Evolution of Alteration Layers Formed during Nuclear Glass Alteration: New Evidence of a Gel as a Diffusive Barrier". In: *Journal of Nuclear Materials* 326.1, pp. 9–18. ISSN: 00223115. DOI: 10.1016/j.jnucmat.2003.10.015.

Ruiz-Agudo, E., H. E. King, L. D. Patiño-López, C. V. Putnis, T. Geisler, C. Rodriguez-Navarro, and A. Putnis (2016). "Control of Silicate Weathering by Interface-Coupled Dissolution-Precipitation Processes at the Mineral-Solution Interface". In: *Geology* 44.7, pp. 567–570. ISSN: 0091-7613, 1943-2682. DOI: 10.1130/G37856.1.

Van Iseghem, P. and B. Grambow (1987). “The Long-Term Corrosion and Modelling of Two Simulated Belgian Reference High-Level Waste Glasses”. In: *MRS Proceedings* 112. ISSN: 0272-9172. DOI: `10.1557/PROC-112-631`.

Van Iseghem, P. et al. (2004). “GLAMOR: A Critical Evaluation of the Dissolution Mechanisms of High-Level Waste Glasses in Conditions of Relevance for Geological Disposal”. In:

Yechieli, Y. and D. Ronen (1996). “Self-Diffusion of Water in a Natural Hypersaline Solution (Dead Sea Brine)”. In: *Geophysical research letters* 23.8, pp. 845–848.

Chapter 3

Dynamics of glass corrosion

3.1 Introduction

Conventional procedures to study the aqueous corrosion of minerals and glasses consist of at least two steps. First, the corrosion itself is induced by experimental alteration of the solid of interest in the laboratory under controlled physico-chemical conditions, or a naturally corroded sample is collected in the field. Secondly, after sample preparation specific to the applied analytical technique, the sample characterization is performed *post mortem*. Depending on the variety and type of applied analytical techniques, several steps of sample preparation are needed, e.g., cross-sectioning for analysis by electron microprobe (EMP) followed by thin foil/wedge preparation by focused ion beam milling (FIB) for transmission electron microscopy (TEM) or atom probe tomography (ATP). Structural and chemical alteration by preparation of the sample has to be considered when interpreting the analyses. In general, *post mortem* analyses have therefore two major disadvantages: (1) Sudden change of environmental conditions by the termination of the experiment (=quenching) and subsequent drying, sawing, and milling may alter the corrosion product, and (2) the quenched sample represents only one point in time in a dynamic process with potentially multiple reaction steps. For *post mortem* analysis, the latter can only be overcome by performing several experiments in parallel and quenching these at different time steps, making it difficult, however, to correlate textural observations as new samples possibly, having slightly different properties, have to be used for each time step.

Specifically for silicate glass corrosion, quenching and drying the sample is crucial as the main corrosion product is a hydrous amorphous silica gel (e.g., Frugier et al., 2008; Rebiscoul et al., 2005; Geisler et al., 2015, and references therein), which is generally prone to structural and chemical changes such as condensation and/or polymerization, loss of water, and/or cracking due to cooling, changes in pH, and dehydration (Iler, 1979). Surface coatings of secondary minerals, that are a common phenomena observed with chemically more complex glasses (e.g., Vernaz et al., 2001), could to some extend be the result of rapid supersaturation by quenching the experiment to room temperature. For instance, this has to be taken into account in the ongoing discussion about the role of secondary mineral precipitates for the potential corrosion rate resumption in the scenario of long-term disposal of vitrified nuclear waste (Gin, 2014). Due to a number of the recent experimental studies utilizing isotope tracer analyses (Geisler et al., 2010;

Geisler et al., 2015; Gin et al., 2015b; Gin et al., 2015a; Verney-Carron et al., 2017), high resolution TEM imaging (Hellmann et al., 2012; Hellmann et al., 2015), and ATP (Gin et al., 2017), the overall mechanistic framework of silicate glass corrosion has been questioned recently. Thus, *in situ* studies overcoming the above mentioned shortcomings of *post mortem* analyses might become essential for the formulation of a coherent corrosion mechanism. However, only a limited number of analytical techniques are available that allow studying solid-water reactions *in situ* without disturbing the reaction.

Atomic force microscopy (AFM) has as *in situ* technique become a vital tool for the characterization of reaction interfaces in mineral-water replacement processes in the last decades (e.g., Gratz et al., 1991; C. V. Putnis and Ruiz-Agudo, 2013, and references therein). However, it is by design limited to morphological changes at the surface of the solid of interest as well as to ambient temperature, which are not applicable for the simulation of long-term storage of corrosion-resistant glasses commonly performed at 90 °C. Hence, only few studies used this *in situ* approach (e.g. Donzel et al., 2003; Abraitis et al., 2000, see also Chapter 2, p. 31). Another *in situ* approach is the *in situ* measurement of ions and pH with microelectrodes in solution during experimental corrosion/alteration of wollastonite (Ruiz-Agudo et al., 2016) that was used to investigate the reaction dynamics and formation of amorphous silica layers as corrosion product. However, the 'open reactor' design limits the applicability to ambient temperatures and relative short run times. Nonetheless, the study makes as strong case for the reaction being governed by the formation of strong solute concentration gradients between the corroding interface and the bulk solution, which is arguably transferable to the corrosion of silicate glasses as well (see Chapter 2, p. 31). In light of these findings, the only major *in situ* data regularly obtained during glass corrosion experiments are aliquot analyses of the bulk solution, which are, however, less meaningful when discussing the underlying corrosion mechanisms.

The goal of this study was to establish a new analytical *in situ* technique that allows the observation of glass corrosion in space and time by confocal micro-Raman spectroscopy. The latter was chosen for multiple reasons: (1) using a laser as probe enables the measurement of the glass sample and its corrosion product(s) through a laser-transparent window within an otherwise closed system, which is need to run the experiment at elevated temperatures. As mentioned above, at room temperatures glass corrosion rates are too low for measurements within laboratory timescales. (2) The lateral resolution of confocal Raman spectroscopy (~1 µm) allows in combination with an automated XYZ stage space-resolved mapping of the corrosion progress by obtaining a full Raman spectrum at each imaging point (=hyperspectral Raman spectroscopy (HRS)). (3) With the advent of charge-coupled device (CCD) multichannel detectors and advances in CPU-based processing power, modern state-of-the-art micro-Raman spectroscopy systems are now sensitive and powerful enough to collect large amount of spectral data in real time. (4) Lastly, the spectroscopic data obtained provide structural (and by implication chemical) information of the (unimpaired) corrosion product over the course of the whole experiment. The ability to *in situ* characterize the silicate glass corrosion product, i.e., a gel of hydrous amorphous silica, is the main advantage here, since silica undergoes structural changes over time depending on a variety of (interlinked) parameters like pH, temperature, and solution chemistry, in particular during quenching and drying (Iler, 1979).

To achieve this goal, a fluid cell (FC) was designed and built from PTFE, which is equipped with a temperature control by external heating and an inert thermocouple located at the bottom of the cell. In this first prototype, the ternary borosilicate glass (TBG) also acted as lid atop the fluid cell. Therefore, a blind hole was drilled from the bottom of the glass lid leaving an actual window thickness of ~180 µm. The side walls of the blind hole were chosen as the solution-glass interface to be observed during the experiment as the lateral resolution of confocal Raman spectroscopy is considerably higher than its depth resolution. With 0.1 *M* HCl as running solution, the formation and dynamic polymerization of an amorphous silica corrosion rim including the occurence of a water-rich zone at the reaction interface between corrosion rim and glass was studied at 70 °C over an experimental duration of 10 days. These first results of fluid cell based confocal hyperspectral Raman spectroscopy (FC-HRS) show the high potential of this technique for space- and time-resolved corrosion experiments and shed new light on the mechanism of the silicate glass corrosion process.

3.2 Material & Methods

3.2.1 Glass sample

The glass was synthesized in a platinum crucible at 1400°C for 3 hours from SiO_2, B_2O_3, and Na_2CO_3 powder that was mixed in the proportion to reach a target glass composition

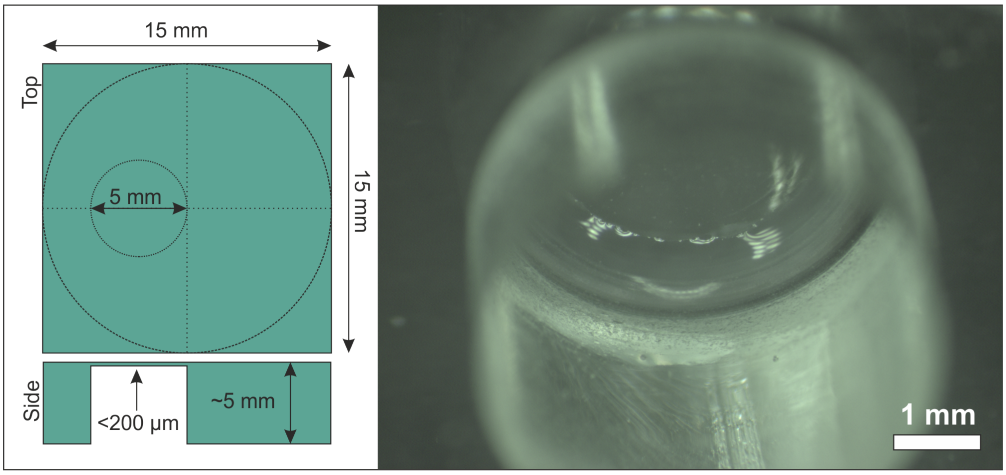

Figure 3.1: Glass lid of the fluid cell. Left: Schematic with dimensions, right: Micrograph taken from the bottom of the glass cuboid into the blind hole.

of 60 mol% SiO_2, 20 mol% Na_2O, and 20 mol% B_2O_3. The glass was molten a second time after crushing and milling it in a ball mill to ensure chemical homogeneity. After quenching the melt in a pre-heated stainless steel mold, it was tempered at ∼560 °C for 6 hours, letting it cool down by switching off the oven. The lid was prepared by cutting a $10 \times 10 \times 5\,\mathrm{mm}^3$ large piece from the raw glass monolith. An approximately 4 mm deep and 5 mm wide blind hole was then drilled into the center of the glass plate using a diamond drill. The internal surface was carefully polished with 3 µm diamond paste to minimize surface roughness. All faces were then carefully ground and polished, reducing the bottom of the blind hole to a thickness of $180 \pm 10\,\mu\mathrm{m}$. After the experiment, the glass sample was washed with distilled water and dried at 60°C over night. To avoid highly Raman scattering epoxy resin in the sample, the hole was stabilized by injecting a dense gypsum paste for grinding and polishing.

3.2.2 Experimental setup

For the *in situ* experiment, we designed and built a special PTFE-based fluid cell for which the borosilicate glass under investigation directly acts as the lid of the cell (Fig. 3.1). The blind hole in the center of the lid, with the window sealing the cell off to the top, permits measuring the formation of the reaction educt, product(s) and the solution in a horizontal plane across the glass hole wall as schematically shown in Fig. 3.2. Such arrangement gives a significantly better resolution in direction of the reaction front movement then conventional confocal depth profiling. As corrosion agent a 0.1 *M* HCl solution with a pH of 1 at room temperature was chosen, since it is known from previous experiments with this glass composition that a several tenth of micrometer-thick corrosion rim will form within a few days (Donzel et al., 2003; Dohmen et al., 2013). Over the course of the experiment, the pH increased to a value of 7.9 due to the release of sodium (and boric acid) from the glass into the solution. Note here that the blind hole can be considered as a wide crack in which supersaturation of silica may occur earlier than in the underlying bulk solution.

3.2.3 Raman spectroscopy

The measurement were carried out with an *Horiba Scientific HR800* Raman spectrometer equipped with an *Olympus BX41* microscope in 180° backscatter geometry and a solid-state Nd:YAG laser ($\lambda = 532.08$ nm) as excitation source at the Steinmann Institute of the University of Bonn, Germany. The scattered Raman light was collected in the frequency range between 200 and 4000 cm^{-1} by an Peltier-cooled electron-multiplier charge-coupled device detector, having a low thermal and read-out noise and high quantum efficiency, after having passed through a 500 µm confocal aperture and a 100 µm spectrometer entrance slit and being dispersed by a grating of 600 grooves/mm. With this analytical setup the spectral resolution was 3.5 cm^{-1}, as given by the full width at half maximum of Ne lines. The accuracy of the spectrometer was monitored by the O_2 and the N_2 band from the air between glass and objective at 1555

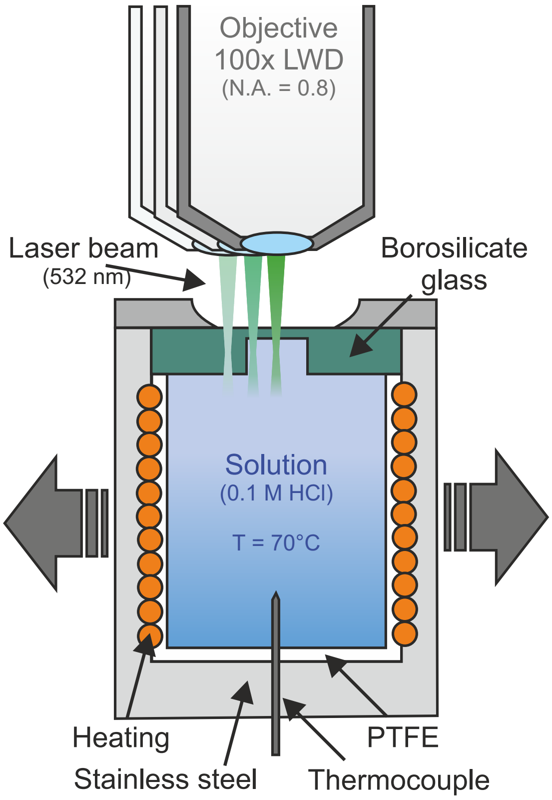

Figure 3.2: Schematic representation of the experimental setup. For illustration, relative movement between objective and fluid cell is presented here, while in reality the objective is fixed to the microscope, and the XYZ stage, on which the fluid cell is mounted, is the only moving part.

and 2331 cm^{-1}, respectively (Fig. 1b). The intensities were corrected for the overall instrument response function (known as white light correction). After filling the fluid cell with the solution and closing it with the glass lid, the cell was placed on a motorized x-y-z mapping stage of the Raman spectrometer with a step size of 0.1 and 0.5 µm in x,y and z direction, respectively, and heated to 70 ± 1 °C. A LWD 100x objective with a numerical aperture, NA, of 0.8 and a working distance of 3.4 mm was used. Since the glass water interface could not be seen in optical images, the interface was searched by measuring the OH frequency region between 2800 and 4000 cm^{-1} and scanning in x-y-z direction. About one hour was needed to find the optimal analytical position and parameters for the measurements. The progress of the corrosion was measured at a depth of ~250 µm below the glass surface, where the spatial resolution is several orders worse than the resolution close to the surface (see below).

The x-y dimension of the imaged area was initially 135×7.5 µm^2 with pixel spacing of 3.0 and 2.5 µm in x and y direction, respectively, but was increased to 250×7.5 µm^2 after about 77 hours using the same pixel spacing. The imaged area was increased, because it was realized that it did not extend into the solution and pristine glass at the same time, because a several micrometer-thick OH-rich silica zones had already developed unexpectedly within the first hour. The beam power was initially set to ~430 mW at the surface of the glass lid, but was then increased to ~610 mW to compensate for lower count times per pixel over an enlarged imaging area. The total counting time per pixel of an image was initially 30 times for 1 second, but was decreased to 20 times 0.7 seconds, yielding total image acquisition times of ~70 and 60 min, respectively. Altogether, 68 x-y images were collected within about 250 hours.

3.2.4 Determination of the lateral resolution

The diffraction-limited theoretical lateral and depth (or axial) resolution at the glass surface was 0.8 ($= 1.2\ \lambda/\mathrm{NA}$) and 3.3 µm ($= 4\ \lambda/(\mathrm{NA})^2$), respectively. However, the measurements were made about 250 µm below the glass surface as measured by confocal depth scans. The latter are corrected for refraction effects using Eq. 6 given in N. J. Everall (2000b) from NA, the refractive index of the glass (= 1.55), and assuming that the objective was fully filled by the Gaussian laser beam so that it reduces its intensity by 1 - e^{-2} (thereby transmitting ~ 86.7% of the laser intensity). Here, the spatial resolution is several orders worse than the theoretical resolution given above due to refraction of the laser beam at the air-glass interface, spherical aberration, and due to diffraction effects (N. J. Everall, 2000b; N. J. Everall, 2000a; Baldwin and Batchelder, 2001). Nevertheless, from the H_2O/OH intensity distribution across the glass-water interface the lateral resolution was empirically estimated to be 10 ± 1 µm using a 500 µm confocal hole. The decrease of lateral resolution with depth mainly reflects the dramatic decrease of the refraction-limited depth resolution, i.e., the dramatic increase of the length of the region illuminated by the incoming laser beam. This length depends mainly on NA and the refraction index of the glass and can reach several tenth of micrometers when focusing deep into the sample (N. J. Everall, 2000b; N. J. Everall, 2000a; Baldwin and Batchelder, 2001). Thus, the empirically determined lateral resolution is affected by the topography of the reaction front and a non-parallel orientation of the front plane with respect to the laser beam axis. Although close to the surface the depth resolution decreases linearly with the depth of the focal point, at depths of several hundreds of micrometers the depth resolution does not in fact monotonically worsen anymore (Baldwin and Batchelder, 2001). Here, a confocal aperture effectively restricts the volume from which a Raman scattering signal is primarily detected and thus also improves the lateral resolution. The choice of a confocal hole size of 500 µm reflects the best compromise between the spatial resolution and the overall Raman intensity.

3.2.5 Data reduction

All Raman spectra were corrected for effects of the elastic scattering of the excitation beam (Long, 1977),

$$I = I_{obs} \cdot \nu_0^3 \cdot \left[1 - exp\left(\frac{-hc\nu}{kT}\right)\right] \frac{\nu}{(\nu_0 - \nu)^4} \tag{3.1}$$

where I_{obs} is the measured intensity, h is the Planck constant, c is the speed of light, k is the Boltzmann constant, T is the absolute temperature, ν_0 is the wavenumber of the incident laser beam (in cm^{-1}), and ν is the measured wavenumber (in cm^{-1}). See also Neuville and Mysen (1996) or Behrens et al. (2006) for application of the Long (1977) correction. The spectral analyses were then performed in the typical frequency regions of O-Si-O bending and Si-O stretching modes, as well as of OH stretching vibrations: (1) 200 to 600 cm^{-1}, (2) 750 to 1100 cm^{-1}, and (3) 2800 to 4000 cm^{-1}. In these frequency regions a cubic background was first subtracted and the integrated intensities were determined for the bands of interest by summing up the intensity multiplied by the spectral width within a certain frequency region using the *LabSpec 6* software. Due to imaging misalignment, missing data points between 30<x<75 µm and 65<t<77 µm had to be interpolated by an Akima spline (fitted in y-direction (time)). Deconvolution of the spectral regions by least-squares fitting of spectroscopic functions to the experimental profiles was not performed, since intensity integration appeared more robust as no physical model is needed to fit the multitude of overlapping vibrational modes (Fig. 3.3). For visualization of the four-dimensional x-y-t-intensity space of the recorded spectral maps (Fig. 3.4), the first of three lines in x-direction (y=-2.5) per time step was chosen (as x-y-mapping was performed first in x and then y-direction).

3.3 Results & Discussion

3.3.1 Spectral analysis

Raman spectroscopy on borosilicate glass provides insights into its structural network organization, mainly on the connectivity of Si-O bonds. The degree of polymerization is reflected by the distribution of Q^n species in the amorphous structure, where Q^n depicts a silica tetrahedron and n the number of linkages over the oxygen corners to adjacent silica tetrahedra. With $n = 0$ (Q^0), the silica tetrahedron is fully isolated from the remaining silica network, sharing no corner with another silica tetrahedron. On the other side, Q^4 represents a four-corner-shared tetrahedron in a three-dimensional silica network. The connectivity of Q^n species is also referred to as number of non-bridging oxygens (NBO), whereby a bridging-oxygen being the corner- or edge shared oxygen(s) of adjacent tetrahedrons. A non-bridging oxygen may be connected to glass network modifiers (e.g. Na^+) within the glass or interacting with an atmosphere or solution at the glass surface.

Figure 3.3 includes a Raman spectrum of the pristine ternary Na borosilicate glass with O-Si-O bending and Si-O stretching modes in the spectral range from 200 to 2800 cm^{-1}, second order bands between 2400 and 2800 cm^{-1} (To et al., 2008). Furthermore, the ν_5 symmetric B-O stretching modes of planar metaborate ring structures were detected near 630 cm^{-1} (Wu and Lee, 1997) and the symmetric stretching modes of the above mentioned Q^n species between 900 and 1250 cm^{-1}, with the Q^3 having the highest intensity. Bond vibrations of BO_3 units in boroxol rings and the stretching band of molecular oxygen (1555 cm^{-1}) and nitrogen (2331 cm^{-1}) from air between objective and glass surface were

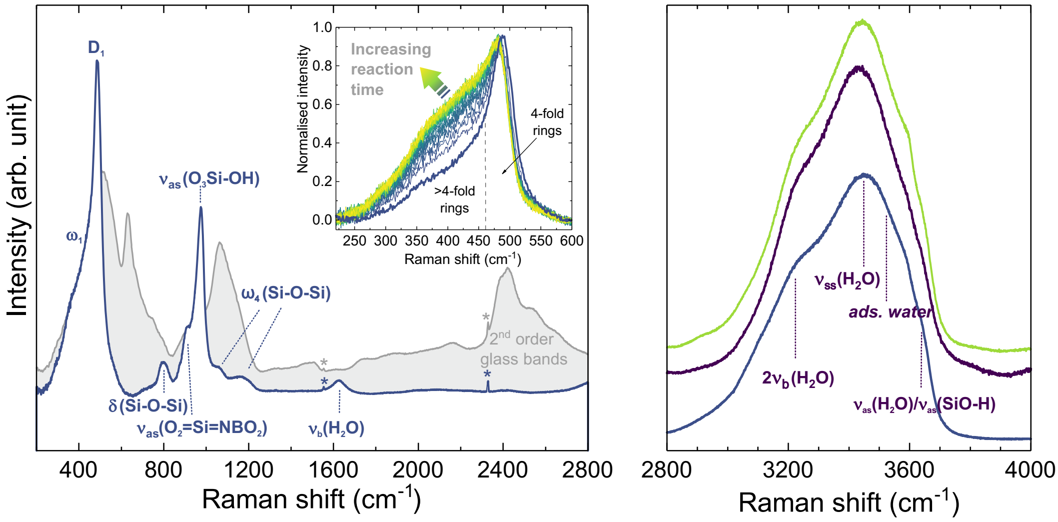

Figure 3.3: Representative background-corrected Raman spectra from amorphous silica (blue spectrum), formed within the first hours of the experiment near the glass surface, and from the silicate glass (light grey spectrum), showing the typical glass bands with second order bands between 2300 and 2900 cm^{-1}. Raman modes are for silica are assigned after Aguiar et al. (2009). The stars (*) mark bands from O_2 (1555 cm^{-1}) and N_2 (2331 cm^{-1}) of the air between glass and objective. Inset diagram shows a series of Raman spectra in the frequency range between 200 and 600 cm^{-1} that were taken at different times at the same location (cf. Fig. 3.4a). The blue and yellow spectra represent the first and last measurement at that location, respectively. Note that with increasing reaction time, the intensity near 430 cm^{-1} increases significantly, reflecting the formation of 5- and 6-fold silica rings with time. Moreover, the ν_s(SiO–H) band is not visible in all spectra (purple spectrum), indicating an inhomogeneous distribution of silica inner surface OH groups that are linked via hydrogen to a water molecule (cf. Fig. 3.4b).

also detected. While the occurrence of exemplary the Q^n species can be expected within the spectral range of 850 to 1250 cm^{-1}, exact band assignment in Raman spectra of silicate glasses is not straightforward and cannot be generalized due to the large range of chemical composition and complexity (Parkinson et al., 2008).

The chemical composition of borosilicate glasses is the major control on the degree of polymerization of the glass network as reflected by the Raman intense Q^n bands. However, for the chemically simple, amorphous silica, the increase in polymerization is best seen in the increase of siloxane ring sizes observed by ω_1 symmetric breathing mode vibrations in the low spectral region (Fig. 3.3) as the intensity of the Q^n speciation is comparatively low. In detail, the spectrum of the here found amorphous silica is generally characterized by a red-shifted, sharp D_1 band around 490 cm^{-1} attributed to four-fold siloxane rings. The absence of the D_2 band indicates that smaller, three-fold siloxane rings did not occur. The D_1 band exhibits an asymmetry shown by a slight broadening of the left shoulder, which can be attributed to siloxane rings of higher orders ($\geq$ five-fold)

Table 3.1: Overview of important Raman modes found in amorphous silica.

Raman shift (cm^{-1})	Mode	Description
430	ω_1	Symmetric breathing modes of ≥5-fold Si-O-Si rings$^{\#}$
450-490	δ_{rock} (Si-O-Si)	Silica rocking bands$^{\#}$
~488	*D1*	Defect band & symmetric breathing modes of planar 4-fold Si-O-Si rings$^{\#}$
601	*D2*	Defect band & symmetric breathing modes of planar 3-fold Si-O-Si rings$^{\#}$
860	ν_{as} ($O_2Si{=}NBO_2$)	Asymmetric stretching of $Q^{2\#}$
967-970	ν_{as} (O_3Si-NBO)	Asymmetric stretching modes of Q^3
	ν_{as} (O_3Si-OH)	Surface silanol groups^{+}
1060-1170	ω_4	Si-O-Si stretching modes$^{\#}$
~1630	ν_b (H_2O)	Bending mode of 'free' water & water H-bonded to H^+ of silanol group^{+}
3250	$2\nu_b$ (H_2O)	First overtone of water bending mode*
3450	ν_{ss} (H_2O)	Symmetric stretching mode of water*
3520		Superimposition of OH vibrations of adsorbed water molecules and vicinal/geminal silanol groups *
3610	ν_{as} (H_2O)	Asymmetric stretching mode of water*
3615	ν_s (SiO-H)	Stretching mode of silanol groups (H-bonded to O of water)$^{+}$
~3680	ν_s (Si-OH)	Stretching mode of vicinal/geminal silanol groups$^{\#}$
3750	ν_s (Si-OH)	Stretching mode of isolated silanol groups$^{\#}$

$^{\#}$Aguiar et al. (2009), $^{+}$Davis and Tomozawa (1996), *Anedda et al. (2003)

(Aguiar et al., 2009). As expected, modes of the metaborate ring structures found in the pristine glass cannot be observed in the amorphous silica, but further Si-O-Si bending modes are observed between 750 and 850 cm^{-1}. The symmetric stretching modes (ν_s) of the Q^n are detected, but are overlain by a sharp intense band around 975 cm^{-1}, which can be attributed to the symmetric stretching mode of the Si-O bond of silanol groups (Aguiar et al., 2009; Davis and Tomozawa, 1995). In the higher wavenumber region, the typical OH and H_2O vibrational modes of water and surface silanol groups can be seen (Fig. 3.3). A summary of the important vibrational modes in the measured spectral range for amorphous silica can be found in Table 3.1.

To study the structural changes of the precipitated amorphous silica in space and time, a set of band intensity ratios was defined. First of all, the polymerization of the corrosion rim was monitored by the integrated intensity of the ω_1 symmetric breathing modes of 5-fold and higher siloxane ring structures between 250 and 460 cm^{-1}, which was divided by the total integrated breathing mode intensity from all siloxane ring structures measured between 250 and 600 cm^{-1} (see Table 3.1. The relative fraction of adsorbed water onto the amorphous silica was determined by the ratio of the integrated intensity between 3500 and 3550 cm^{-1}, where the superimposed OH vibrations of adsorbed water molecules and vicinal/geminal silanol groups (Anedda et al., 2003) are found, over the integrated intensity of the total H_2O/OH bands measured between 2800 and 3800 cm^{-1}. Additionally, the relative fraction of (solely) surface silanol groups in the amorphous silica was estimated from ratio of the integrated intensity of the sharp Si-OH band between 935 and 1010 cm^{-1} over the surrounding vibrational modes of the Q^n species of silica between 850 and 1250 cm^{-1}. Lastly, the relative content of water species in the analysed volume was determined by the ratio of the integrated intensity of the OH groups measured between 3000 and 3750 cm^{-1} and the integrated intensity of the intense silica vibrational modes measured between 250 and 1250 cm^{-1}. Note that all these parameters are not a correct quantitative measure of the actual fractions. In the absence of a detailed understanding of the silica structure and its Raman spectrum, however, these ratios are easily determinable parameters that can be used to monitor structural changes in silica as a function of space and time, which is relatively independent of spectrum quality and physical assumptions. As such, it is also appears as the more approachable and robust method to analysis the large number of about 5000 complex Raman spectra obtained in the experiment.

3.3.2 Corrosion dynamics

By the time the first mapping step was finished (1+1 h experimental setup + imaging), an hydrous amorphous silica layer of about 90 µm had already formed (Fig. 3.4). The formation progress of this gel was therefore not directly recorded. However, any solid state diffusion-controlled glass hydrolysis and ion exchange process can be excluded from producing such a layer as they are two slow to work over these length scale within a few hours. Accordingly, it can be assumed that the gel precipitated from solution by an interface-coupled dissolution-precipitation process. Hereby, the congruent dissolution releases glass constituents into solution, with the possibility of saturating the adjacent solution at the solution-glass interface with respect to amorphous silica, especially in the

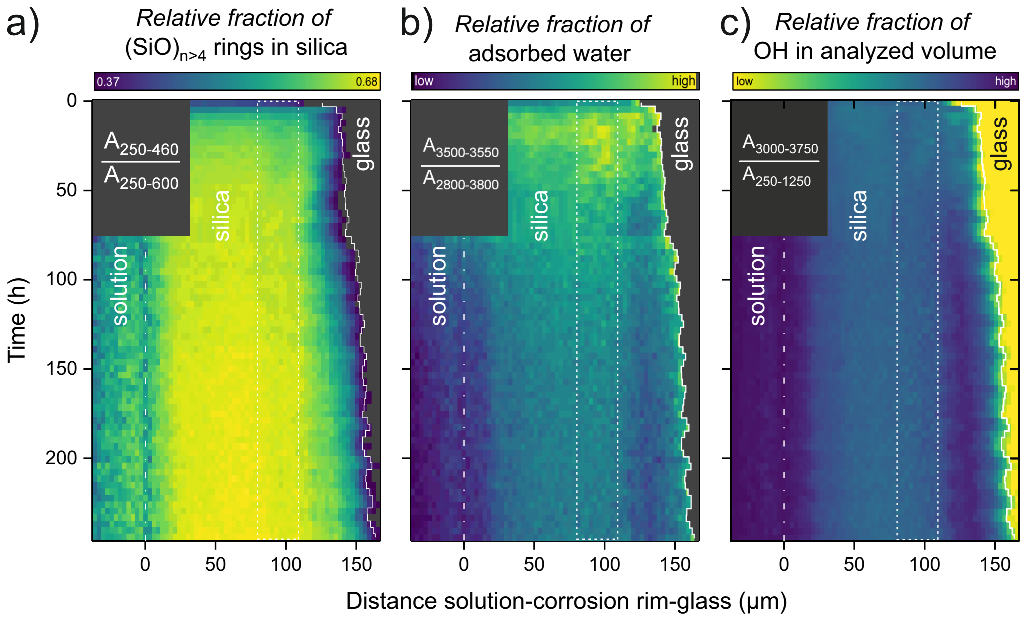

Figure 3.4: False-color Raman images rendered from the recorded spectra over time, showing the spatial distribution of (a) the relative fraction of 5- and 6-fold rings in silica, (b) the relative fraction of adsorbed water on the silica surface, and (c) OH groups in the analysed volume. The images were obtained by color-coding the ratios $A_{250\text{-}460}/A_{250\text{-}600}$, $A_{3500\text{-}3550}/A_{2800\text{-}3800}$, and $A_{3000\text{-}3750}/A_{250\text{-}1250}$, where A represents the accumulated and background-corrected intensity in the frequency range given as index (in cm^{-1}). Dashed line marks location of the time profiles shown in Fig. 3.5. Dashed lines encase profile location shown in Fig. 3.5, white lines represent the location of the retreating silica/glass interface, which is derived from sigmoidal fits of the intensity of the OH bands. Gray areas in the top-left were initially not imaged. Glass areas in a) and b) are also shown in grey as the presented parameter are not applicable for glass.

case of acidic (to low-alkaline) solutions, where overall silica solubility is low in the first place (Iler, 1979). Moreover, the solution volume within the hole may be saturated much faster than the underlying solution (Fig. 3.2). Such local saturation at an dissolving interface was observed in experiments on the replacement of wollastonite by amorphous silica (Ruiz-Agudo et al., 2016) as well as in the SPFT experiments within this study (see Chapter 2, p. 31). The principle idea behind the local saturation is that during dissolution a concentration gradient between bulk solution and dissolving interface will develop if the release rate of Si from the glass is higher than the transport of Si into the bulk solution. In the latter study, the interfacial solution also showed a distinctively higher pH value than the surrounding solution (due to the release of calcium by the dissolution of wollastonite, $CaSiO_3$. In case of this experiment here, the release of sodium from the glass into the interfacial solution should have increased the pH, which only effectively changes the solubility of amorphous silica starting from a value of pH $>$ 9 at 70 °C, but shifts the polymerization of silica into the domain of rapid aggregation (pH 2 - 7, Iler, 1979). Hence, nanoparticles of silica from the condensation of monomeric silicic acid to dimers and oligomers/cyclic structures in solution would quickly cross-link to form a gel through the ongoing reaction of silanol groups to siloxane bridges represented by the following equation:

$$\equiv Si\text{-}OH + HO\text{-}Si\equiv \;\rightleftharpoons\; \equiv Si\text{-}O\text{-}Si\equiv + H_2O \tag{3.2}$$

The aggregation of particles is particularly preferred in the presence of sodium, which neutralizes the negative surface charge of silica particles in the electric double layer (Iler, 1979).

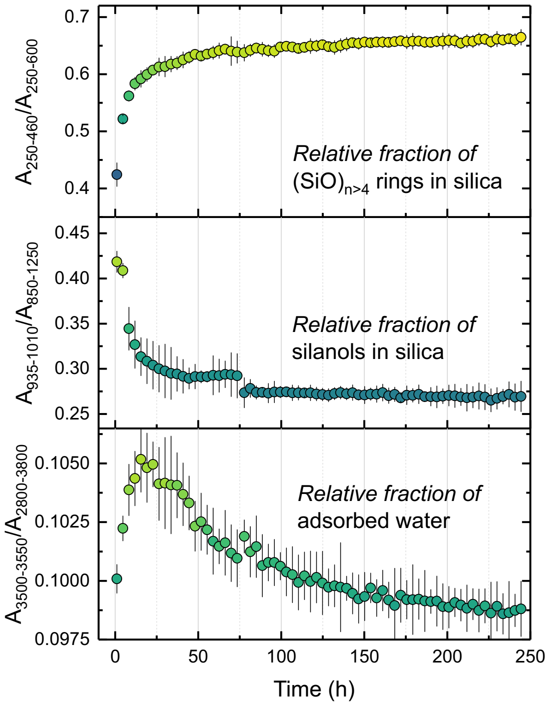

Figure 3.5: Time dependence of the ratios $A_{940\text{-}1000}/A_{750\text{-}1250}$ (top), $A_{250\text{-}460}/A_{250\text{-}600}$ (centre), and $A_{3560\text{-}3620}/A_{3000\text{-}3750}$ (bottom) taken from the locations encased by the dashed lines (average over 10 pixel) in Fig. 3.4. Errors are given as 2 s.d. .

Within the next 10 hours, the hydrous silica gel polymerizes and aggregates indicated by a red-shift of the D_1 band at the very beginning and the strong increase in Si-O-Si ring structures of higher orders (Figs. 3.3 and 3.4). At the same time, the relative fraction of surfacial silanol groups in the gel decreases in an anti-correlated fashion (Fig. 3.5), which can be interpreted as the result of the ongoing polymerization and silica sphere size growth. With increasing degree of polymerization, surface curvature of the silica spheres should change as well. With an increase in surface curvature, the interaction of surface silanol groups is in turn decreased and silanol groups become isolated. Isolated silanol groups are, however, less likely to bind free water molecules, as water molecules are preferentially adsorbed on complex interacting vicinal and geminal silanol

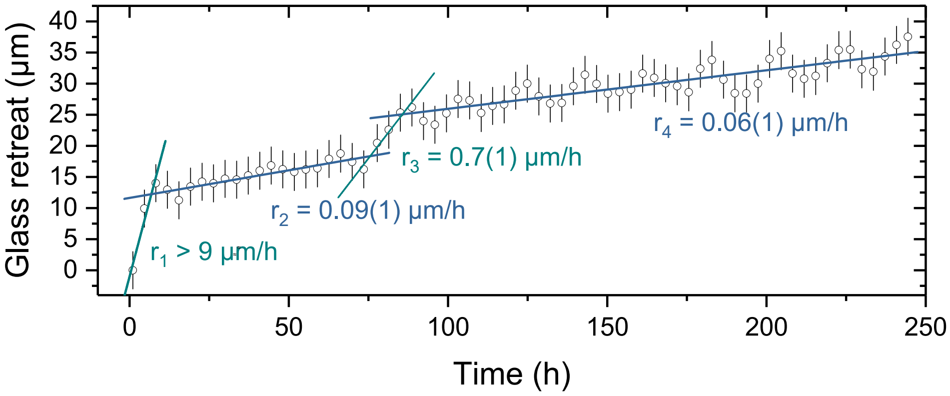

Figure 3.6: Retreat of the silica-glass interface as a function of time, showing four different kinetic regimes. The given rates r_2, r_3, and r_4 were obtained by a linear least-squares fit to the data. However, r_1 was estimated considering that a $\sim$90 µm thick silica had already formed before the first image was taken. The glass retreat is given by the shift of the position of silica-glass interface compared to its position in the first image at t = 1.0 h. The undulation on the fitted position is an artefact of the mechanical XYZ table.

groups (Brinker and Scherer, 1990). After Anedda et al. (2003), the Raman band at 3520 cm^{-1} represents a superimposition of several silanol-related vibrations: O-H vibrations from water molecules adsorbed at the surface, interacting silanols hydrogen-bonded to oxygen atoms of other silanols and/or adsorbed water molecules. These authors propose that the relative concentration of adsorbed water molecules and interacting vicinal and geminal silanol groups with respect to the isolated ones increases as the pore diameter decreases. The other way round, this means that water has be to be released from the surface, when the surface curvature increases, e.g. during silica sphere growth. As such, this dependency explains, why a relative increase of water adsorption can be seen in the initial gel within the first 10 hours, but a later decrease with the continuous polymerization and silica sphere growth (Fig. 3.5).

After about 75 hours, when the initial maturation progress levels out Fig. 3.5, a water-rich zone between the pristine glass and silica rim can be observed (Fig. 3.4), as indicated by the ratio of the integrated intensities of the OH bands over the lower spectral range of the solid silica ($A_{3000\text{-}3700}/A_{250\text{-}600}$). At this stage, an increase in the retreat rate of the glass interface can be observed for about 15 hours (Fig. 3.6), in which the water-rich zone apparently grows at the expense of the pristine glass.

The different corrosion rates, calculated here by the *in situ* measured glass retreat (Fig. 3.6), correlate well with the established rate regimes (e.g., Frugier et al., 2008; Frugier et al., 2017). The initial rate, r_1 (Fig. 3.6), corresponds to the fast forward disso-

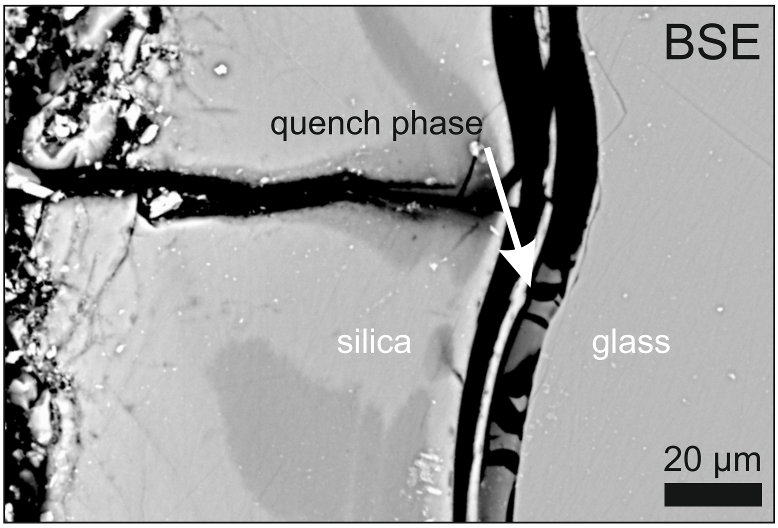

Figure 3.7: Backscattered electron image taken after the experiment from a polished section that was prepared from the dried glass window. Note the occurrence of a gap/crack marking the interface between the pristine glass and the silica corrosion rim.

lution rate (Stage I, Gin, 2014), which is evoked by the congruent dissolution of the glass network (Geisler et al., 2010; Geisler et al., 2015). The slowdown of the corrosion rate by about two orders of magnitude after the formation of the initial corrosion rim (r_2, Fig. 3.6) conforms with the residual rate regime (Stage II, Gin, 2014). Hereby, the rate is controlled by the transport properties of the corrosion rim (Geisler et al., 2015). In the literature, a later-stage resumption of the corrosion rate was reported and proposed to originate from the rapid formation of secondary minerals like phyllosilicates and zeolites at solution-silica interface (e.g., Gin and Mestre, 2001; Vienna et al., 2013; Fournier et al., 2014), which are supposed to cause an undersaturation of the (local) solution and a destabilization of the gel layer (Rajmohan et al., 2010; Gin et al., 2012). However, the formation of secondary phases was not observed during (Fig. 3.4) or after (Fig. 3.7) the here presented *in situ* experiment. The glass composition does not support the formation of secondary mineral phases like phyllosilicates and zeolites. Nonetheless, a short resumption of the corrosion rate was observed (r_3, Fig. 3.6), which here correlates with the formation of the water-rich zone at the corrosion rim-glass interface (Fig. 3.4c). A plausible explanation is for this is an increase in pH at the silica-glass interface caused by release of Na from the congruent glass dissolution and the transport limitation through the polymerized corrosion rim. As such, the interfacial (pore) solution is undersaturated with respect to amorphous silica and might temporarily increase the rate of congruent glass dissolution, after which the corrosion rate drops down to a residual level again (r_4, Fig. 3.6).

After the experiment was stopped, the water-rich zone between the pristine glass and the silica reaction rim is visible in backscattered electron (BSE) images (Fig. 3.7). Here, the formerly water-rich zone appears as a gap that is, after cooling and drying, partly filled with hydrous amorphous silica that appears dark-grey in the BSE image. Most importantly, the width of the gap with about 20 µm is the same as the *in situ* observed water-rich zone.

3.3.3 Implications for the Reaction Mechanism

The above described insights into the dynamics of borosilicate glass corrosion by an aqueous medium provide a series of observations to refine existing corrosion models. The most obvious feature of glass corrosion found in this study might be the development of the water-rich zone at the interface between glass and corrosion rim. Gaps or cracks between pristine glass and reaction rim are commonly found in dried samples from *ex situ* experiments (e.g., Anaf, 2010; Sterpenich and Libourel, 2001; Geisler et al., 2010; Geisler et al., 2015; Dohmen et al., 2013) and are explained by cracking or ripping apart due to shrinkage of the previously hydrous silica layer. However, in this study, the gap already exists during the experiments in form of a water-rich zone of similar extend and is part of the corrosion process rather than a by-product of sample treatment. The concentration of water or OH-bearing phases at the reaction interface is a common phenomenon and fundamental basis of mineral replacement by interface-coupled dissolution-precipitation (A. Putnis, 2002; A. Putnis and C. V. Putnis, 2007), which has been discussed to be applicable for the glass corrosion as well (Geisler et al., 2010; Geisler et al., 2015; Hellmann et al., 2012).

The development of the water-rich zone shows a strong correlation with the structural maturation of the initial corrosion rim (as shown above) seen by increasing polymerization and implied silica sphere size growth by the relative decrease of surface-adsorbed water molecules. Such maturation might slow down mass transport through the corrosion rim. Depending on the rate ratio between glass corrosion and mass transport, the pH can increase in the (pore) solution at the glass interface by continued release of sodium from the glass. This, in turn, self-enhances the corrosion rate as could be seen by the (temporary) resumption of corrosion, which is not an uncommon phenomena and currently discussed issue in the nuclear waste community (Ribet and Gin, 2004; Fournier et al., 2014; Frugier et al., 2017).

The sudden formation of the initial gel layer of about 90 µm within the first hour of the experiment is further evidence that the glass corrosion is proceeding by an interface-coupled dissolution-precipitation mechanism (Geisler et al., 2010; Geisler et al., 2015) and that this process is not restricted to high alkaline conditions as proposed by Gin et al. (2015b). Solid state diffusion-controlled hydrolysis and ion exchange reactions cannot facilitate glass corrosion over such a range within the short time frame.

Lastly, besides providing more insights into the fundamental reaction processes, the water-rich zone being seen as a structural weakness could explain the phenomenon of "flacking" or "scaling" often observed in archaeological glasses (Pearson, 1988).

3.3.4 Method review

As shown above, fluid cell hyperspectral Raman spectroscopy is capable to provide unique insights into (running) processes and interim stages of aqueous corrosion/alteration reactions, which are otherwise lost in standard *ex situ* experiments and *post mortem* analysis. Understanding this study as a proof of concept, FC-HRS (as of right now) has also its limitation and needed improvements, which shall briefly discussed here.

In the case of glass corrosion, preparation of a glass lid in dimension of 15 x 15 x 5 mm^3 is cost-wise and technically not too challenging, while for mineral-fluid reactions fracture-free and large enough crystals will be needed. Constructional modifications on the cell design or the use of an additional sealing window (e.g. corrosion-resistent sapphire glass) atop the crystal of interest might solve this problem. For more complex and therefore slower reacting glasses (or other materials), the fluid cell might be taken out and set aside to be then regularly be re-placed under the Raman microscope and measured. Preliminary test showed no problem with locating and adjusting to the original mapping location by using surface features of the glass lid, which ultimately should be improved by laser-etching marks onto the surface.

The use of oil immersion objectives with an N.A. close the glass of interest should enhance the depth resolution significantly (N. Everall, 2014). As explained in the methods section, the depth resolution is approximately by one magnitude lower then the lateral resolution, hence, the approach to measure in lateral and not confocal direction. A higher depth resolution will again minimize the sampling volume and as a consequence increase the spatial resolution further. With that either the signal-noise ratio of the Raman spectra would be increased or signal accumulation times can be lowered to allow faster mapping. To suppress the observed undulation of the XY positioning of the mechanical table, an optical encoder should be installed.

Feature-wise, newer prototypes of the fluid cell are already equipped with additional electrodes for impedance spectroscopy measurements to gain insights into the fluid chemistry at any time of the experiment. Additionally, in- and outlets allow sampling of the solution phase as well as manipulation of the solution chemistry during the experiment, e.g., by insertion of isotope tracer (D_2O) or acids/bases to change the pH.

The limiting factor for the common usage of FC-HRS will most likely be the requirement of a powerful laser system attached to the Raman spectrometer system. In this setup, a 532 Nd:YAG laser with an output power of max. 2 W was used, which results in approximately 0.6 W at the sample interface. No damaging effects of such high laser power on either starting material nor reaction product was observed, which is most likely due to the immersion in solution and thus rapid heat dissipation.

3.4 References

Abraitis, P. K., F. R. Livens, J. E. Monteith, J. S. Small, D. P. Trivedi, D. J. Vaughan, and R. A. Wogelius (2000). “The Kinetics and Mechanisms of Simulated British Magnox Waste Glass Dissolution as a Function of pH, Silicic Acid Activity and Time in Low Temperature Aqueous Systems”. In: *Applied Geochemistry* 15.9, pp. 1399–1416.

Aguiar, H., J. Serra, P. González, and B. León (2009). “Structural Study of Sol–Gel Silicate Glasses by IR and Raman Spectroscopies”. In: *Journal of Non-Crystalline Solids* 355.8, pp. 475–480. ISSN: 0022-3093. DOI: `10.1016/j.jnoncrysol.2009.01.010`.

Anaf, W. (2010). “Study on the Formation of Heterogeneous Structures in Leached Layers during the Corrosion Process of Glass”. In: *CeROArt. Conservation, Exposition, Restauration d’Objets d’Art*. CeROArt asbl.

Anedda, A., C. M. Carbonaro, F. Clemente, R. Corpino, and P. C. Ricci (2003). "Raman Investigation of Surface OH-Species in Porous Silica". In: *The Journal of Physical Chemistry B* 107.49, pp. 13661–13664. ISSN: 1520-6106, 1520-5207. DOI: `10.1021/jp036691d`.

Baldwin, K. and D. Batchelder (2001). "Confocal Raman Microspectroscopy through a Planar Interface". In: *Applied Spectroscopy* 55.5, pp. 517–524.

Behrens, H., J. Roux, D. Neuville, and M. Siemann (2006). "Quantification of Dissolved H2O in Silicate Glasses Using Confocal microRaman Spectroscopy". In: *Chemical Geology* 229.1-3, pp. 96–112. ISSN: 00092541. DOI: `10.1016/j.chemgeo.2006.01.014`.

Brinker, C. J. and G. W. Scherer (1990). *Sol-Gel Science: The Physics and Chemistry of Sol-Gel Processing*. San Diego: Academic press. ISBN: 978-0-12-134970-7.

Davis, K. and M. Tomozawa (1996). "An Infrared Spectroscopic Study of Water-Related Species in Silica Glasses". In: *Journal of Non-Crystalline Solids* 201.3, pp. 177–198. ISSN: 00223093. DOI: `10.1016/0022-3093(95)00631-1`.

Davis, K. and M. Tomozawa (1995). "Water Diffusion into Silica Glass: Structural Changes in Silica Glass and Their Effect on Water Solubility and Diffusivity". In: *Journal of Non-Crystalline Solids* 185.3, pp. 203–220.

Dohmen, L., C. Lenting, R. O. C. Fonseca, T. Nagel, A. Heuser, T. Geisler, and R. Denkler (2013). "Pattern Formation in Silicate Glass Corrosion Zones". In: *International Journal of Applied Glass Science* 4.4, pp. 357–370. ISSN: 20411286. DOI: `10.1111/ijag.12046`.

Donzel, N., S. Gin, F. Augereau, and M. Ramonda (2003). "Study of Gel Development during SON68 Glass Alteration Using Atomic Force Microscopy. Comparison with Two Simplified Glasses". In: *Journal of Nuclear Materials* 317.1, pp. 83–92. ISSN: 00223115. DOI: `10.1016/S0022-3115(02)01705-1`.

Everall, N. (2014). "Optimising Image Quality in 2D and 3D Confocal Raman Mapping". In: *Journal of Raman Spectroscopy* 45.1, pp. 133–138.

Everall, N. J. (2000a). "Confocal Raman Microscopy: Why the Depth Resolution and Spatial Accuracy Can Be Much Worse than You Think". In: *Applied Spectroscopy* 54.10, pp. 1515–1520.

Everall, N. J. (2000b). “Modeling and Measuring the Effect of Refraction on the Depth Resolution of Confocal Raman Microscopy”. In: *Applied Spectroscopy* 54.6, pp. 773–782.

Fournier, M., S. Gin, and P. Frugier (2014). “Resumption of Nuclear Glass Alteration: State of the Art”. In: *Journal of Nuclear Materials* 448.1-3, pp. 348–363. ISSN: 00223115. DOI: `10.1016/j.jnucmat.2014.02.022`.

Frugier, P. et al. (2008). “SON68 Nuclear Glass Dissolution Kinetics: Current State of Knowledge and Basis of the New GRAAL Model”. In: *Journal of Nuclear Materials* 380.1-3, pp. 8–21. ISSN: 00223115. DOI: `10.1016/j.jnucmat.2008.06.044`.

Frugier, P., M. Fournier, and S. Gin (2017). “Modeling Resumption of Glass Alteration Due to Zeolites Precipitation”. In: *Procedia Earth and Planetary Science* 17, pp. 340–343. ISSN: 18785220. DOI: `10.1016/j.proeps.2016.12.086`.

Geisler, T., A. Janssen, D. Scheiter, T. Stephan, J. Berndt, and A. Putnis (2010). “Aqueous Corrosion of Borosilicate Glass under Acidic Conditions: A New Corrosion Mechanism”. In: *Journal of Non-Crystalline Solids* 356.28-30, pp. 1458–1465. ISSN: 00223093. DOI: `10.1016/j.jnoncrysol.2010.04.033`.

Geisler, T., T. Nagel, M. R. Kilburn, A. Janssen, J. P. Icenhower, R. O. Fonseca, M. Grange, and A. A. Nemchin (2015). “The Mechanism of Borosilicate Glass Corrosion Revisited”. In: *Geochimica et Cosmochimica Acta* 158, pp. 112–129. ISSN: 00167037. DOI: `10.1016/j.gca.2015.02.039`.

Gin, S. (2014). “Open Scientific Questions about Nuclear Glass Corrosion”. In: *Procedia Materials Science* 7, pp. 163–171. ISSN: 22118128. DOI: `10.1016/j.mspro.2014.10.022`.

Gin, S. et al. (2017). “Atom-Probe Tomography, TEM and ToF-SIMS Study of Borosilicate Glass Alteration Rim: A Multiscale Approach to Investigating Rate-Limiting Mechanisms”. In: *Geochimica et Cosmochimica Acta* 202, pp. 57–76. ISSN: 00167037. DOI: `10.1016/j.gca.2016.12.029`.

Gin, S. and J. Mestre (2001). “SON 68 Nuclear Glass Alteration Kinetics between pH 7 and pH 11.5”. In: *Journal of Nuclear Materials* 295.1, pp. 83–96.

Gin, S., X. Beaudoux, F. Angéli, C. Jégou, and N. Godon (2012). “Effect of Composition on the Short-Term and Long-Term Dissolution Rates of Ten Borosilicate Glasses of Increasing Complexity from 3 to 30 Oxides”. In: *Journal of Non-Crystalline*

Solids 358.18-19, pp. 2559–2570. ISSN: 00223093. DOI: `10.1016/j.jnoncrysol.2012.05.024`.

Gin, S., P. Jollivet, M. Fournier, F. Angeli, P. Frugier, and T. Charpentier (2015a). “Origin and Consequences of Silicate Glass Passivation by Surface Layers”. In: *Nature Communications* 6, p. 6360. ISSN: 2041-1723. DOI: `10.1038/ncomms7360`.

Gin, S., P. Jollivet, M. Fournier, C. Berthon, Z. Wang, A. Mitroshkov, Z. Zhu, and J. V. Ryan (2015b). “The Fate of Silicon during Glass Corrosion under Alkaline Conditions: A Mechanistic and Kinetic Study with the International Simple Glass”. In: *Geochimica et Cosmochimica Acta* 151, pp. 68–85. ISSN: 00167037. DOI: `10.1016/j.gca.2014.12.009`.

Gratz, A., S. Manne, and P. Hansma (1991). “Atomic Force Microscopy of Atomic-Scale Ledges and Etch Pits Formed during Dissolution of Quartz”. In: *Science* 251.4999, pp. 1343–1346.

Hellmann, R., S. Cotte, E. Cadel, S. Malladi, L. S. Karlsson, S. Lozano-Perez, M. Cabié, and A. Seyeux (2015). “Nanometre-Scale Evidence for Interfacial Dissolution–Reprecipitation Control of Silicate Glass Corrosion”. In: *Nature Materials* 14.3, pp. 307–311. ISSN: 1476-1122, 1476-4660. DOI: `10.1038/nmat4172`.

Hellmann, R., R. Wirth, D. Daval, J.-P. Barnes, J.-M. Penisson, D. Tisserand, T. Epicier, B. Florin, and R. L. Hervig (2012). “Unifying Natural and Laboratory Chemical Weathering with Interfacial Dissolution–Reprecipitation: A Study Based on the Nanometer-Scale Chemistry of Fluid–Silicate Interfaces”. In: *Chemical Geology* 294-295, pp. 203–216. ISSN: 00092541. DOI: `10.1016/j.chemgeo.2011.12.002`.

Iler, R. K. (1979). *The Chemistry of Silica: Solubility, Polymerization, Colloid and Surface Properties and Biochemistry of Silica.* John Wiley & Sons. 896 pp. ISBN: 978-0-471-02404-0.

Long, D. A. (1977). *Raman Spectroscopy.* McGraw-Hill. 276 pp. ISBN: 978-0-07-038675-4.

Neuville, D. R. and B. O. Mysen (1996). “Role of Aluminium in the Silicate Network: In Situ, High-Temperature Study of Glasses and Melts on the Join SiO2-NaAlO2”. In: *Geochimica et Cosmochimica Acta* 60.10, pp. 1727–1737. ISSN: 0016-7037. DOI: `http://dx.doi.org/10.1016/0016-7037(96)00049-X`.

Parkinson, B., D. Holland, M. Smith, C. Larson, J. Doerr, M. Affatigato, S. Feller, A. Howes, and C. Scales (2008). “Quantitative Measurement of Q3 Species in Silicate and Borosilicate Glasses Using Raman Spectroscopy”. In: *Journal of*

Non-Crystalline Solids 354.17, pp. 1936–1942. ISSN: 00223093. DOI: `10.1016/j.jnoncrysol.2007.06.105`.

Pearson, C. (1988). *Conservation of Marine Archaeological Objects.* Elsevier. ISBN: 978-0-408-10668-9.

Putnis, A. (2002). "Mineral Replacement Reactions: From Macroscopic Observations to Microscopic Mechanisms". In: *Mineralogical Magazine* 66.5, pp. 689–708. ISSN: 14718022, 0026461X. DOI: `10.1180/0026461026650056`.

Putnis, A. and C. V. Putnis (2007). "The Mechanism of Reequilibration of Solids in the Presence of a Fluid Phase". In: *Journal of Solid State Chemistry* 180.5, pp. 1783–1786. ISSN: 00224596. DOI: `10.1016/j.jssc.2007.03.023`.

Putnis, C. V. and E. Ruiz-Agudo (2013). "The Mineral–Water Interface: Where Minerals React with the Environment". In: *Elements* 9.3, pp. 177–182.

Rajmohan, N., P. Frugier, and S. Gin (2010). "Composition Effects on Synthetic Glass Alteration Mechanisms: Part 1. Experiments". In: *Chemical Geology* 279.3-4, pp. 106–119. ISSN: 00092541. DOI: `10.1016/j.chemgeo.2010.10.010`.

Rebiscoul, D., P. Frugier, S. Gin, and A. Ayral (2005). "Protective Properties and Dissolution Ability of the Gel Formed during Nuclear Glass Alteration". In: *Journal of Nuclear Materials* 342.1-3, pp. 26–34. ISSN: 00223115. DOI: `10.1016/j.jnucmat.2005.03.018`.

Ribet, S. and S. Gin (2004). "Role of Neoformed Phases on the Mechanisms Controlling the Resumption of SON68 Glass Alteration in Alkaline Media". In: *Journal of Nuclear Materials* 324.2-3, pp. 152–164.

Ruiz-Agudo, E., H. E. King, L. D. Patiño-López, C. V. Putnis, T. Geisler, C. Rodriguez-Navarro, and A. Putnis (2016). "Control of Silicate Weathering by Interface-Coupled Dissolution-Precipitation Processes at the Mineral-Solution Interface". In: *Geology* 44.7, pp. 567–570. ISSN: 0091-7613, 1943-2682. DOI: `10.1130/G37856.1`.

Sterpenich, J. and G. Libourel (2001). "Using Stained Glass Windows to Understand the Durability of Toxic Waste Matrices". In: *Chemical Geology* 174.1–3. 6th International Silicate Melt Workshop, pp. 181–193. ISSN: 0009-2541. DOI: `http://dx.doi.org/10.1016/S0009-2541(00)00315-6`.

To, T. T., D. Bougeard, and K. S. Smirnov (2008). "Molecular Dynamics Study of the Vibrational Pattern of Ring Structures in the Raman Spectra of Vitreous Silica”. In: *Journal of Raman Spectroscopy* 39.12, pp. 1869–1877. ISSN: 03770486, 10974555. DOI: `10.1002/jrs.2052`.

Vernaz, E., S. Gin, C. Jégou, and I. Ribet (2001). “Present Understanding of R7T7 Glass Alteration Kinetics and Their Impact on Long-Term Behavior Modeling”. In: *Journal of Nuclear Materials* 298.1, pp. 27–36.

Verney-Carron, A. et al. (2017). “Understanding the Mechanisms of Si–K–Ca Glass Alteration Using Silicon Isotopes”. In: *Geochimica et Cosmochimica Acta* 203 (Supplement C), pp. 404–421. ISSN: 0016-7037. DOI: `10.1016/j.gca.2017.01.030`.

Vienna, J. D., J. V. Ryan, S. Gin, and Y. Inagaki (2013). “Current Understanding and Remaining Challenges in Modeling Long-Term Degradation of Borosilicate Nuclear Waste Glasses”. In: *International Journal of Applied Glass Science* 4.4, pp. 283–294. ISSN: 20411286. DOI: `10.1111/ijag.12050`.

Wu, K. and S.-Y. Lee (1997). “Ab Initio Calculations on Normal Mode Vibrations and the Raman and IR Spectra of the [B3O6] 3-Metaborate Ring”. In: *The Journal of Physical Chemistry A* 101.5, pp. 937–940.

Chapter 4

Corrosion rim-glass interface

4.1 Introduction

While surface, textural, and structural analyses of glass corrosion rims on all scales have already allowed identifying distinct reaction steps, there is a lack of information on - with the partial exception of *in situ* experiments (see Chapter 3, p. 57) - about the dynamics of a (multistage) corrosion process and the contribution of solution and glass components to the corrosion rim.

In general, corroded glass, if not revealing chemical or structural patterns, is build up by a so called 'hydrated glass' layer, which is void of alkaline elements and is located directly adjacent to the pristine glass, spatially followed by an amorphous layer of porous, silica-rich material (often called 'gel' in case of nuclear glass or 'palagonite' for natural glass) and (not obligatory) by a surface layer of secondary minerals. The hydrated glass is assumed to be the result of hydration following ion exchange of mobile glass constituents with inbound hydrogen by hydrolysis of the non-bridging Si-O-M bonds (M = B, Na, Ca). Reported widths of the hydrated layer vary strongly from nano- to micrometers (e.g., Ait Chaou et al., 2015; Gin et al., 2011; Gin et al., 2013a; Verney-Carron et al., 2008; Verney-Carron et al., 2010), and depends on glass composition, time, temperature, solution composition, pH and saturation with respect to individual phases, which in turn, are all interlinked and result in a specific corrosion rate. To explain the observed slowdown of the corrosion rate, a protective effect by pore closure in the gel layer or by reaction of the hydrated glass (passivating reactive interphase (PRI)) have been discussed (Frugier et al., 2008). In some cases, the corrosion rim detaches partly or entirely from the pristine glass (e.g., Dohmen et al., 2013; Geisler et al., 2010; Sterpenich and Libourel, 2001; Verney-Carron et al., 2008; Schalm and Anaf, 2016), which is also known as flaking (Pearson, 1988). While elements with a high solubility in aqueous solutions are transferred to the bulk solution, less soluble elements are retained in the corrosion rim (e.g., Valle et al., 2010). Until now, a general, coherent corrosion mechanism, which can account for the dynamic formation of the corrosion rim over a spectrum of different conditions and glasses compositions, natural and synthetic ones, is still under debate. The two (most recent) hypotheses for the formation of the corrosion rim are: (i) *in situ* silica recondensation of the alkaline-free, hydrated glass layer (e.g., Van Iseghem and Grambow, 1987; Bunker, 1994; Jégou et al., 2000; Grambow and Müller, 2001; Rebiscoul et al., 2004; Van Iseghem et al., 2004; Gin, 2014; Frugier et al., 2008; Gin et al., 2015a), and (ii) precipitation and polymerisation of amorphous silica coupled in space and time to the congruent dissolution of the glass (Geisler et al., 2010; Geisler et al., 2015; Hellmann et al., 2012). Valle and co-workers (2010) stated that the main difference of these models are the degree of equilibrium with recondensation only requiring a local, but precipitation a global thermodynamic equilibrium. This stands strongly in contrast to self-organization during precipitation reactions far from equilibrium in general (Nakouzi and Steinbock, 2016) and specifically in corroded glasses (e.g. Geisler et al., 2010; Dohmen et al., 2013; Wang et al., 2016, and references therein).

Isotope tracers are a powerful tool to investigate such dynamic processes in a wide range of replacement reactions. Most approaches to study replacement reactions so far are based on the examination of alteration products of either natural minerals or glass from hydrothermal experiments. In case of laboratory experiments, analysis of the accompanying run solution allows mass balancing the reaction. The advantage of using isotopes is that by tracing back the participation of different reservoirs (e.g., running solution, primary phase) in the formation of individual phases or layers during a reaction, new insights into the underlying mechanism can be gained. The basic procedure of using isotopes as reaction tracers in replacement processes is to enrich the experimental solution (or *vice versa* the educt itself) with a naturally non-abundant isotope of the element of interest, and then monitor the distribution of this isotope pair in the run product and/or solution. The idea behind this is that - beside small fractionation effects - all isotopes of an element behave structurally and chemically in the same way. For once, by measuring the ratio of tracer and naturally abundant isotope, the extend of exchange between solution and solid material can be quantified, but even more importantly, it can provide evidence for rupture of old and formation of new chemical bonds (with the tracers).

Isotope tracer experiments based on the initial work by O'Neil (1977) are nowadays a common technique to investigate reaction mechanisms in the field of mineralogy, with experiments in the early 2000s, where the solid solution-aqueous solution system KCl-KBr-H_2O was used as a model system to determine the underlying reaction mechanism. In this study, it could be shown that the solution-derived ^{40}K was abundantly incorporated into the replaced salt crystal (C. V. Putnis and Mezger, 2004). The latter was interpreted as a strong argument for the coupled dissolution of the ^{38}KBr crystal and the reprecipitation of (^{38}K,^{40}K)Cl. In a different case, the stability of the hafnium isotopic system during recrystallization of radiation-damaged (metamict) zircons by acidic aqueous solutions was tested using ^{180}Hf as tracer (Lenting et al., 2010). The results showed that the isotope tracer was not incorporated into the recrystallized zircon structure. Only Hf precipitates of the highly insoluble hafnium tracer were found on the surface and in small fissures. This led to the interpretation that the underlying reaction mechanism for the recrystallization ot the formerly amorphous zircon must be a proton-based diffusion-reaction mechanism.

Geisler and co-workers performed isotope tracer studies with silicate glasses (2010; 2015), whereby the authors used a simple ternary borosilicate glass as well as the more complex German nuclear waste glass WAK and a variety of isotope tracers. Laser-ICPMS and NanoSIMS analyses of the glass corrosion rims revealed abundant exchange of magnesium, oxygen, as well as silicon with their respective tracers in solution. However, while the oxygen isotope ratio across the corrosion rim is rather constant, magnesium and silicon isotope ratios are characterized by spiked profiles. Particularly, the evolution of the silicon isotope ratio seems to depend on the structure, porosity and permeability of the newly formed corrosion rim. If the corrosion rim appears dense, no silicon tracer was found in the corrosion rim, whereas, in porous sections higher amounts of the tracer were found. It has to be emphasized here that porous and dense corrosion rims were not only found in experiments with the same glass at different solution conditions, but also on different faces of a single glass monolith itself.

Jollivet et al. (2008) made similar observations in a setup, where the glass monolith was placed onto glass powder, resulting in morphologically and chemically different corrosion rims. The bottom face thereby was thinner, but exhibited a higher silica content, which was interpreted to have clogged the porosity and thereby prohibited the silicon isotope tracer to be incorporated. The corrosion rim of the bottom face revealed a higher silica content, while the extent of the rim was larger on the solution face. Valle et al. (2010) performed silicon and oxygen isotope tracer experiments on a subset of the French non-active SON68 nuclear waste glass. The authors report an extensive exchange of both silicon and oxygen isotopes between corrosion rim and solution, indicated for both isotope tracers by concentration gradients across the corrosion rims, which indicates thorough mixing of silicon and oxygen derived from solution and corroded glass. In contrast to a study by Gin et al. (2015) and conducted experiments in this study, the running solution was not saturated with respect to silica (Valle et al., 2010: 20 mg/L). The experiment in the tracer study on the ISG glass - a simplified version of the SON68 glass - by Gin and co-workers (2015) was saturated with respect to silica and did not show any noteworthy enrichment of silicon isotope tracer across the corrosion rim. Both studies (Valle et al., 2010; Gin et al., 2015a) argue that the silicon isotope exchange occurs via hydrolysis of Si-O-M bonds (M = Si, Al, Zr), which is thought to be favourable in dilute conditions. Hydrolysis is one of the driving forces in the diffusion-driven corrosion models. On the other hand, Icenhower and Steefel (2013) reported flow-through experiments showing that low amounts of silicon in solution (∼ 20 mg/L) are sufficient to drastically decrease the overall glass corrosion rate. It seems therefore unlikely that the rate of hydrolysis between those sets of experiments was very different, and therefore cannot be the reason for the different isotopic ratios. Lastly, a more recent study by "SON68 Glass Alteration under Si-Rich Solutions at Low Temperature (35–90° C): Kinetics, Secondary Phases and Isotopic Exchange Studies" showed clear uptake of a silicon tracer from a silica-rich synthetic groundwater solution during experimental corrosion of the SON68 glass.

It follows from these studies that the available results on different isotope tracers are not strictly coherent and can be explained by a single underlying reaction mechanism. The conceptual idea of this study was to use a wide range of isotope tracers to possibly cover all structural units of the corroding glass. Four glass compositions ranging from a simple ternary borosilicate glass to the six component International Simple Glass (ISG) (Gin et al., 2013b) were used to evaluate the role of composition for the underlying reaction mechanism. Furthermore, the isotope tracer experiments were performed on pristine as well as on precorroded glass samples to test the reactivity of the corrosion rim. For this reason, full saturation of the solution with respect to amorphous silica was chosen to suppress any re-dissolution of the precorroded samples.

The decoupling oxygen and hydrogen tracers at the corrosion rim-glass interface, which was previously postulated (Geisler et al., 2010; Geisler et al., 2015; Hellmann et al., 2012) and is now known from atom probe studies (Hellmann et al., 2015; Gin et al., 2017) to be atomically sharp, gives strong evidence for the corrosion mechanism to be based on the congruent dissolution of the glass coupled in space and time to the polymerization and precipitation of amorphous silica. Additionally, the so-called 'hydrated glass' can be traced back to be a quench phase from an interfacial (pore) solution, formed during quenching and drying the sample.

Results of this study are published in Lenting et al. (2018).

4.2 Methods

4.2.1 Glass synthesis

The ISG glass was produced by *MoSci Corporation*, USA, on the decision to establish an international benchmark glass for comparability of results between different experiment, laboratories and workgroups worldwide (Gin et al., 2013b). Other glasses (Table 4.1) were produced in-house from standard reagents mixed and milled, then melted in a platinum crucible at 1400 °C for 3 h, crushed and milled again to be re-melted. After quenching the melt in a pre-heated stainless steel mould, it was structurally relaxed at 560 °C for 6 h, letting it slowly cool down to room temperature over several hours by switching off the oven. Glass coupons of about 2 mm edge length were cut. All faces were then carefully ground and polished with 1 µm diamond paste to minimize surface roughness. The exact dimensions of each monolith were measured with a calliper to determine the geometric surface area.

4.2.2 Corrosion experiments

Corrosion experiments were performed on pristine and precorroded glasses of four different chemical compositions (Table 4.1). For the precorroded experiments, glass monoliths from a set of long-term experiments were extracted, where a total of 17 monoliths per glass were corroded in PTFE vessels of 180 mL volume at 90 °C for 7 months. However, experiments with the less-corrosion-resistant TBG glass were started later on the assumption of higher corrosion rates (Geisler et al., 2010). The monoliths were placed in in-house made PTFE holder with 5 mm blind holes for each monolith, touching only corners or edges, positioned at the bottom of the vessels. The fill level of each vessel was adjusted according to the total geometric surface of the individual glass monoliths to achieve a S/V ratio of $\sim 0.21\,\mathrm{m}^{-1}$. The reaction solution was half-saturated with respect to amorphous silica at 90 °C and pH 7 by dissolution of potassium silicate (K_2SiO_3) prepared as given in Gin et al. (2015). The pH value of each solution was checked regularly and if needed re-adjusted by addition of nitric acid/potassium hydroxide solution. The corrosion progress over time can be seen in Fig. 4.1, which is depicted by the evolution of pH and sodium concentration in solution. The isotope tracer solution was prepared to be fully-saturated with respect to amorphous silica at 90 °C and pH 7 to suppress re-dissolution. Potassium silicate was again produced, but this time with $^{30}SiO_2$. Further,

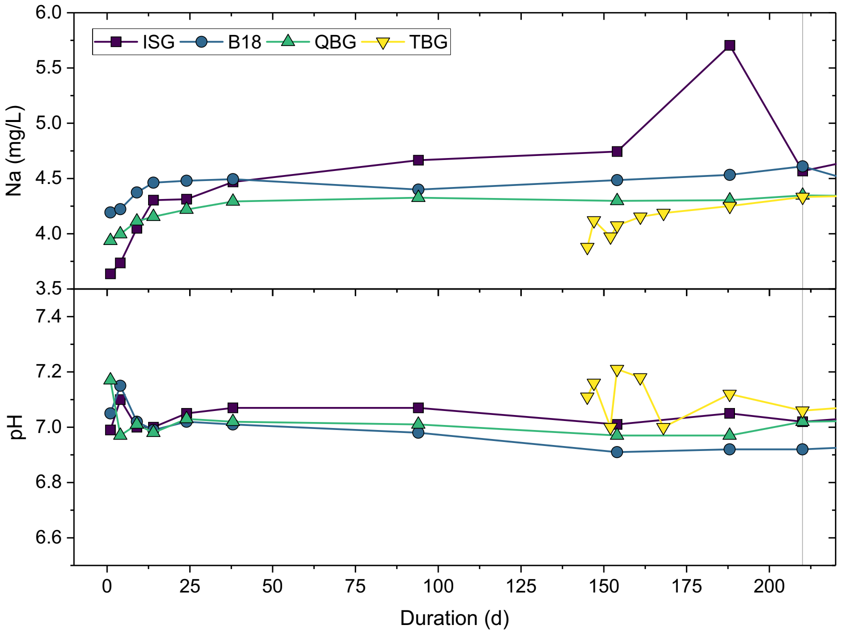

Figure 4.1: Na concentration (top) and pH (bottom) of precorrosion stage of experiments. pH was re-adjusted by addition of HNO_3 when necessary. Samples were transferred to tracer solution at day 210. Error (2 s.d.) within icon size.

$^{44}CaCl_2$ and $H_3{}^{10}BO_3$ were incorporated and $D_2{}^{18}O$ was used as solvent, while the pH was adjusted to 7 by addition nitric acid. The detailed (isotopic) solution composition is listed in Table 4.1. The precorroded monoliths were quickly rinsed in distilled water between transferring them from the running experiment set into smaller vessels for the tracer experiments. Each tracer experiment then contained one glass monolith with 1 mL of tracer solution ($S/V = 26 \pm 4\,m^{-1}$) encapsulated in an in-house built PTFE-lined cold-sealed vessels, running at 90 or 150 °C for three months. After quenching the cold-sealed vessels in air and checking for leakage by weighing, the glass monoliths were removed and rinsed in distilled water to suppress any late-stage precipitation and to remove excess running solution. Samples were then dried at 60 °C over night. Consequently to surface characterization by µRaman spectroscopy, samples were embodied in a resin mount, which was ground and then polished with 1 µm diamond spray to produce cross-sections of the pristine glasses and reaction rims. The TBG experiment at 90 °C with a pristine sample failed, and could not be repeated in time for NanoSIMS analysis, and the precorroded sample at 150 °C was fully altered, giving no possibility for cross-interface analysis.

4.2.3 µRaman spectroscopy

Raman spectra of the surface of the corroded samples were obtained by a confocal *Horiba* HR800 Raman spectrometer equipped with an *Olympus* BX41 microscope in 180° backscatter geometry at the Steinmann Institut of the University of Bonn, Germany, using a Nd:YAG laser (532.09 nm) with about 0.1 W laser output power, a 100× objective, a 600 grooves/mm grating, a confocal hole of 500 µm and a spectrometer entrance slit widths of 100 µm, yielding a spectral resolution of approx. 3.5 cm^{-1}. Samples were analysed over the range of 100 to 4000 cm^{-1} in three spectral windows, each measured for 20×3 s. All spectra were white-light corrected and the spectrometer was calibrated using the Ne line at 1707.04 cm^{-1}.

Data treatment of the Raman spectra was afterwards performed as follows: (i) the intensities of all measured spectra were normalized on the height of the intensity measured at the position of ~630 cm^{-1}, which is where the metaborate rings bands are observed in borosilicate glasses. (ii) To eliminate any underlying glass signal in the collected spectra, an averaged spectrum (n=10) of the individual pristine glass was adjusted to the intensity measured here, and consequently subtracted. This was necessary due to the small width of the surface layers and the larger depth resolution of the Raman measurements. (iii) Afterwards the cubic background spline was set and subtracted as well.

4.2.4 NanoSIMS

NanoSIMS analyses were performed on resin-mounted and cross-sectioned samples with a *CAMECA* NanoSIMS 50L at the Centre for Microscopy, Characterisation and Analysis at the University of Western Australia. The polished sample mounts were coated with gold to provide conductivity. Prior to each analysis, every area was pre-sputtered with the primary beam to a dose of more than 2×10^{17} cm^2. Isotope mapping was performed in three runs per location, two for positively charged ions with the oxygen source and after changing the ion source to caesium one for negatively charged ions (cross-analysed ions in bold):

O^-: $\mathbf{^{10}B}$, $\mathbf{^{11}B}$, ^{27}Na, ^{28}Si, $\mathbf{^{30}Si}$, ^{40}Ca, $\mathbf{^{44}Ca}$,

O^-: $\mathbf{^{10}B}$, $\mathbf{^{23}Na}$, ^{27}Al, $\mathbf{^{30}Si}$, ^{38}K, $\mathbf{^{44}Ca}$, ^{90}Zr,

Cs^+: ^{1}H, ^{2}H, $\mathbf{^{10}B}$, $\mathbf{^{11}B}$, ^{16}O, ^{18}O, ^{19}F.

For both sources, the beam diameter was approximately 100 nm and the impact energy was 16 keV. The high-resolution O- beam was obtained with a *Hyperion (H200) RF* plasma oxygen ion source. The beam current was approximately 3 pA for Cs^+ and 14 pA for O-. Images were carried out with a raster size of $10 - 50\,\mathrm{\mu m}^2$, with a resolution of 256 x 256 pixels and a dwell time of 25-60 ms per pixel. Line scans were acquired using the line scan beam control mode on the NanoSIMS. First, an image of the area was acquired over an area of $20 - 30\,\mathrm{\mu m}^2$, at a resolution of 256 x 256 pixels and with a dwell time of 1 ms/pixel. A line across the interface was then manually selected and scanned. The length of the line was in the range of 5 µm and the counting time was 2-6 seconds per step.

Multiple one- and two-dimensional isotope mappings for each set of isotopes were performed on all glass samples by manual or preprogrammed automated runs (over night). In a few cases mappings of the latter had to be discarded/repeated due to an incorrect focus (the focus cannot be adjusted in automated runs). Note that all sets of measurements have some isotopes (marked in bold above) in common to allow for direct data correlation. The second set with then three unmeasured isotopes were located directly adjacent to the first one to minimize beam damage for the third run in the original position again (reposition error: ± 2 µm). Fluorine, originating from the fresh PTFE linings of the reaction vessels, was also measured as an additional tracer. Data handling was performed with *ImageJ/Fiji* (Schindelin et al., 2012) and the *OpenMIMS* plugin (Gormanns et al., 2012), in which profiles were extracted from the isotope maps perpendicular to the reaction front, accumulating a width of 50 pixels per step. Then the sigmoidal-shaped ^{18}O profiles at the rim-glass interface were fitted with a double Boltzmann function. A double Boltzmann function was chosen over a single one to account for tailings some isotopes like boron reveal in the reaction rim. The inflection point of the ^{18}O fit close to the interface was then chosen as point of origin for data visualization. Consequently, coordinates of the two data sets measured by oxygen source were shifted by aligning the inflection points of the double Boltzmann fitted boron profiles, while also cross-checking the sodium profiles of the first two datasets for congruence. Hence, the data alignment around the interface can be taken as accurate, while the matching of the outer rim boundary may underlie minor discrepancies due to small variation in rim thickness and focus issues during automated runs. Moreover, as evident by a small gap between samples and embedding resin, the extended drying of the epoxy resin followed to shrinkage by which less consolidated material was ripped-off the sample surface.

4.2.5 FIB-STEM

An Electron-transparent thin foil was prepared from a corroded ISG-90/90 sample by utilizing a *Zeiss* NVision 40 cross beam station at the Forschungszentrum Jülich (IEK-6), Germany. The sample was coated with C to enhance the electrical conductivity. The lamella was extracted perpendicular to the surface including a layer of resin, corroded glass and pristine glass. To avoid beam damage by the Ga^+ beam, a protective layer of approximately 2 µm C was deposited on the glass surface. A thick slice of 1 µm was cut out of the sample (beam current 30 kV/300 pA) and attached to an *Oxford Instruments* Omniprobe TEM-grid. The lamella was stepwise thinned >100 nm using decreasing beam current for each step (30 kV/150 pA, 30 kV/80 pA, 30 kV/40 pA). Another thin foil of the QBG-90/150 experiment was prepared by using a *FEI* Helios Nanolab G3 UC focused ion beam-scanning electron microscope (FIB-SEM).

The FIB foils were investigated in a *FEI* Talos F200X (scanning) transmission electron microscopy ((S)TEM) equipped with four energy-dispersive X-ray detectors (Super-X EDX). The *FEI* Talos F200X TEM information limit is 0.12 nm. All FIB-SEM and TEM analyses were carried out at the Microscopy Square, Utrecht University, Netherlands.

4.3 Results

4.3.1 Raman spectroscopy of the corrosion rim

Before mounting the samples in epoxy resin and cross-sectioning, the outer corrosion surfaces were characterized by Raman spectroscopy, revealing typical spectral features of amorphous silica (see Fig. 4.2):

250-500 cm^{-1}: The lower spectral region around the D_1 defect band at $\sim$495 cm^{-1} shows an asymmetric flank towards lower frequencies due to oxygen breathing motions of higher silica ring structures (n>4). In pristine borosilicate glasses, this area is symmetric (Fig. 4.2).

850-1250 cm^{-1}: The Q^n species distribution differs from the pristine glass in the regard that it shifts to an increase in the Q^2 species, representing a lower degree of polymerization.

3000-3750 cm^{-1}: All measured outer corrosion surfaces reveal high intensities in the higher frequency range indicating significant amounts of OH-groups/water being contained in the silica corrosion rim.

For an in-depth description of the Raman spectrum of amorphous silica formed during glass corrosion, see the spectral analysis in Chapter 3 (Section 3.3.1, p. 65).
Although all Raman spectra of the corroded surfaces reveal amorphous silica to build up the corrosion rim, not all spectra seem to indicate the exact same structure of the amorphous silica across glasses as seen by the differences in the distribution of the Q^n species. This might have two reason: (i) background signal from the chemically and hence structurally diverse pristine glass, and (ii) pH and salinity at the corrosion interface will differ between experiments due to the chemical compositions and consequently unequal elemental release by dissolution. While pH and salinity control aggregation and polymerization of amorphous silica on one hand (Iler, 1979), on various elements released from the pristine glass can potentially be re-incorporated during silica condensation which further alters the structure.

4.3.2 Texture and thickness of the corrosion rim

Processed NanoSIMS maps and profiles of the corrosion rim-glass cross-sections are shown in Fig. 4.4-4.10 In general, the cross-sections cover the whole range of (i) the epoxy resin (embedding matrix), (ii) the outer part of the corroded glass, where secondary minerals might precipitate, (iii) the newly formed corrosion rim including the prior altered part in cases of precorroded glass samples, (iv) the interface between rim and glass, and (v) the pristine glass itself. The zone around the interface between corrosion rim and pristine glass is thereby characterized by a strong drop in the measured intensities of the network modifying sodium as well as network forming (and modifying) boron in direction of the corrosion rim as already seen in previous studies (e.g. Gin et al., 2015b; Gin et al., 2015a; Hellmann et al., 2015; Gin et al., 2016; Bouakkaz et al., 2016; Gin et al., 2017. Due to the ambiguity of structure and extend of the corrosion interface (zone), so far often defined by its diffusion profiles, the sharp drop in intensity of the inbound ^{18}O tracer was selected in this study as reference for the location of the interface for all samples. ^{18}O was chosen because it is an external tracer and no glass constituent (beside the natural abundance 0.2% of the total oxygen) and because the spatial resolution of the NanoSIMS is higher

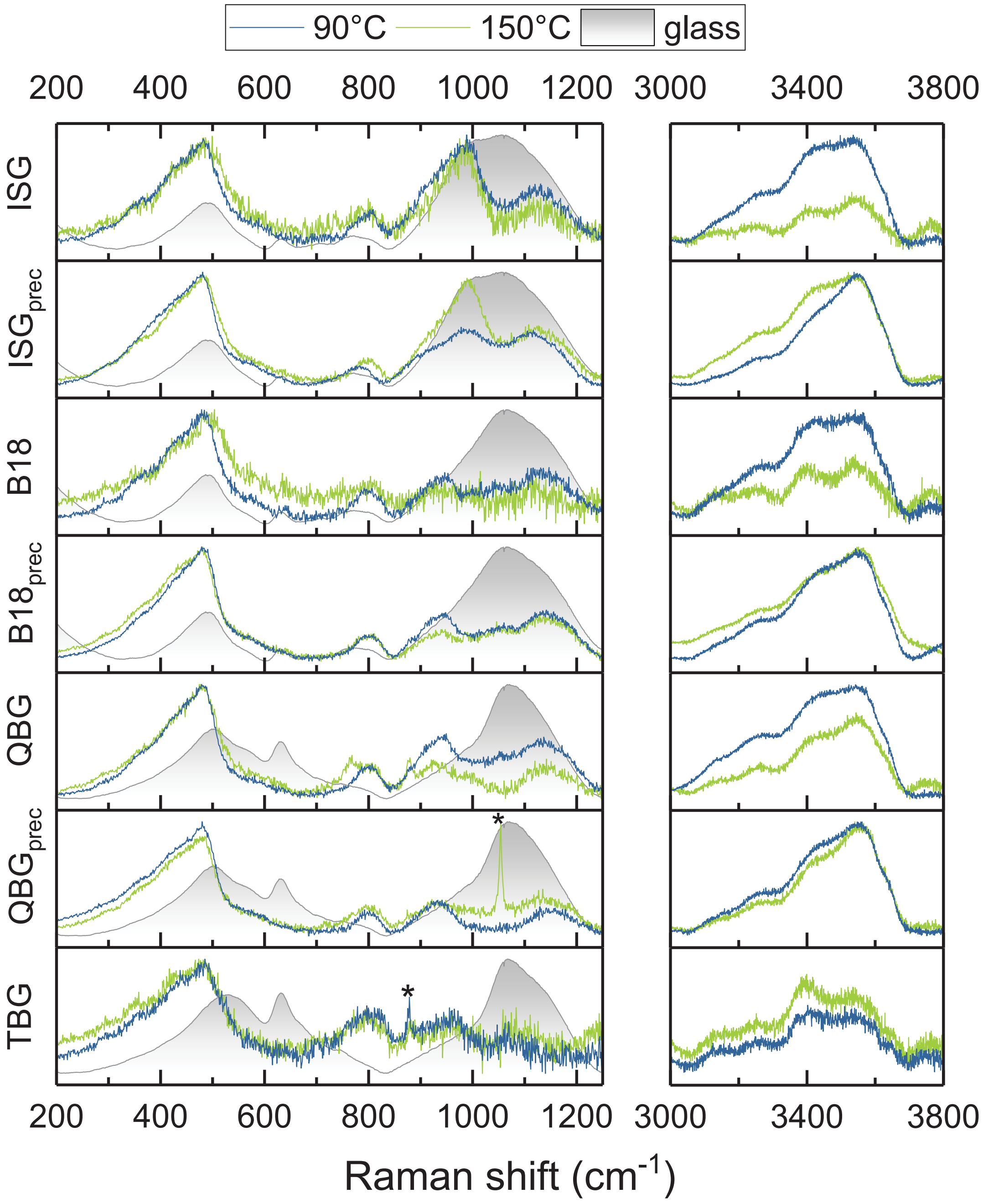

Figure 4.2: Raman spectra of pristine glasses (grey) and samples corroded at 90 °C (blue) and 150 °C (green). Asterisks mark unidentified Raman bands.

Table 4.1: Glass and solution compositions, experimental details and comparison of NanoSIMS analyses of corroded glass samples.

Glass composition	SiO_2 (mol%)	ZrO_2 (mol%)	Al_2O_3 (mol%)	B_2O_3 (mol%)	CaO (mol%)	Na_2O (mol%)	Density (g/cm^3)	
ISG	60.7(7)	1.7(1)	3.8(1)	16.0(8)	5.6(1)	12.3(15)	2.41(14)	
B18	60.7(14)		4.1(1)	17.6(8)	5.3(1)	12.3(2)	2.45(3)	
QBG	65.9(10)		4.2(1)	11.9(7)	0.09(1)	17.9(2)	2.48(2)	
TBG	65.3(3)			15.8(2)		18.7(3)	2.49(5)	
Solution composition	$pH_{init,RT}$	SA/V (mm^2/mL)	SiO_2 (mmol/L)	KOH (mmol/L)	BH_3O_3 (mmol/L)	$CaCl_2$ (mmol/L)	D/H	$^{18}O/^{16}O$
Precorrosion	7.0	2.7	2.2 (3.1% ^{30}Si)	6.0			0.0001	0.002
Tracer	7.0	24	5.9 (99% ^{30}Si)	12.1	4.1 (99% ^{10}B)	0.76 (97% ^{44}Ca)	0.225	0.231
Experiment	ISG				B18			
Temperature (°C)	90	150	90/90	90/150	90	150	90/90	90/150
Condition	pristine	pristine	precorroded	precorroded	pristine	pristine	precorroded	precorroded
Duration (months)	3	3	7+3	7+3	3	3	7+3	7+3
$pH_{final,RT}$	7.6	7.7	8.1	8.1	8.2	8.3	7.6	8.3
Rim thickness (µm)	1.63(11)	0.68(21)	2.97(25)	2.70(21)	1.74(02)	0.52(10)	3.10(27)	3.21(0.29)
Avg. $^{18}O/^{16}O$	0.04449(72)	0.08263(82)	0.03602(20)	0.05017(12)	0.1487	0.03439(10)	0.11791(24)	
Experiment	QBG				TBG			
Temperature (°C)	90	150	90/90	90/150	90	150	90/90	90/150
Condition	pristine	pristine	precorroded	precorroded	pristine	pristine	precorroded	precorroded
Duration (months)	3	3	7+3	7+3	3	3	2+3	2+3
$pH_{final,RT}$	7.7	8.0	8.3	8.4	n.a.	7.2	8.1	10.3
Rim thickness (µm)	1.54(37)	1.92(21)	2.42(07)	4.09(26)	n.a.	1.75(08)	0.45(9)	fully corroded
Avg. $^{18}O/^{16}O$	0.07709(38)	0.07774(28)	0.03263(12)	0.07587(28)	n.a.	0.05989(35)	0.07240(321)	0.116(35)

when using the Cs^+ source (<50 nm) instead of the O^- source (<200 nm).

Corrosion rim thickness

The corrosion rim thickness was derived by fitting the $^{18}O/^{16}O$ NanoSIMS images with the local thickness function of the *Fiji/ImageJ* software package (Schindelin et al., 2012). Comparing the individual widths (Table 4.1), a few observations can be made: (i) the rim thickness in the basic 90 °C experiments fall within a similar range between 1.54(37) µm (QBG) and 1.74(02) µm (B18), (ii) the respective experiments at 150 °C reveal a smaller width most likely caused by initial dissolution, (iii) the precorroded samples show naturally the largest width, up to a fully corroded sample of the TBG glass (not shown here).

Isotope & chemical alteration: The International Simple Glass

Starting with a closer look at the results of the reference experiment with the pristine *International Simple Glass* corroded at 90 °C (Fig. 4.4a), most glass constituents (Na, B, Si, Al, Zr) reveal a behaviour also reported in recent literature (Gin et al., 2015a; Gin et al., 2015b):

- **Sodium** is characterized by a sharp sigmoidal-shaped profile across the interface zone with a flat signal throughout the corrosion rim.
- **Boron** shows a profile similar to sodium at the interface, but the concentration of boron only slowly decreases towards the outer border of the corrosion rim.
- **Silicium** is relatively enriched in the corrosion rim.
- **Aluminium** and **zirconium** also appear to be slightly enriched in the corrosion rim and show a strong spike at the solution-corrosion rim boundary, i.e., at the sample surface.

Note that when applying any ablating analysis technique on a multi-phase sample, evaporation properties of the individual phases might differ strongly, i.e., the ablation of material from the hydrated corrosion rim might be more efficient than from the pristine glass resulting in an artificial, relative signal increase. Furthermore, the NanoSIMS intensity signals are not calibrated to the actual content in the analysed material. Under the assumption zirconium is immobile, it is often used as an internal standard. However, a concentration of zirconium is observed at the solution-rim boundary in these

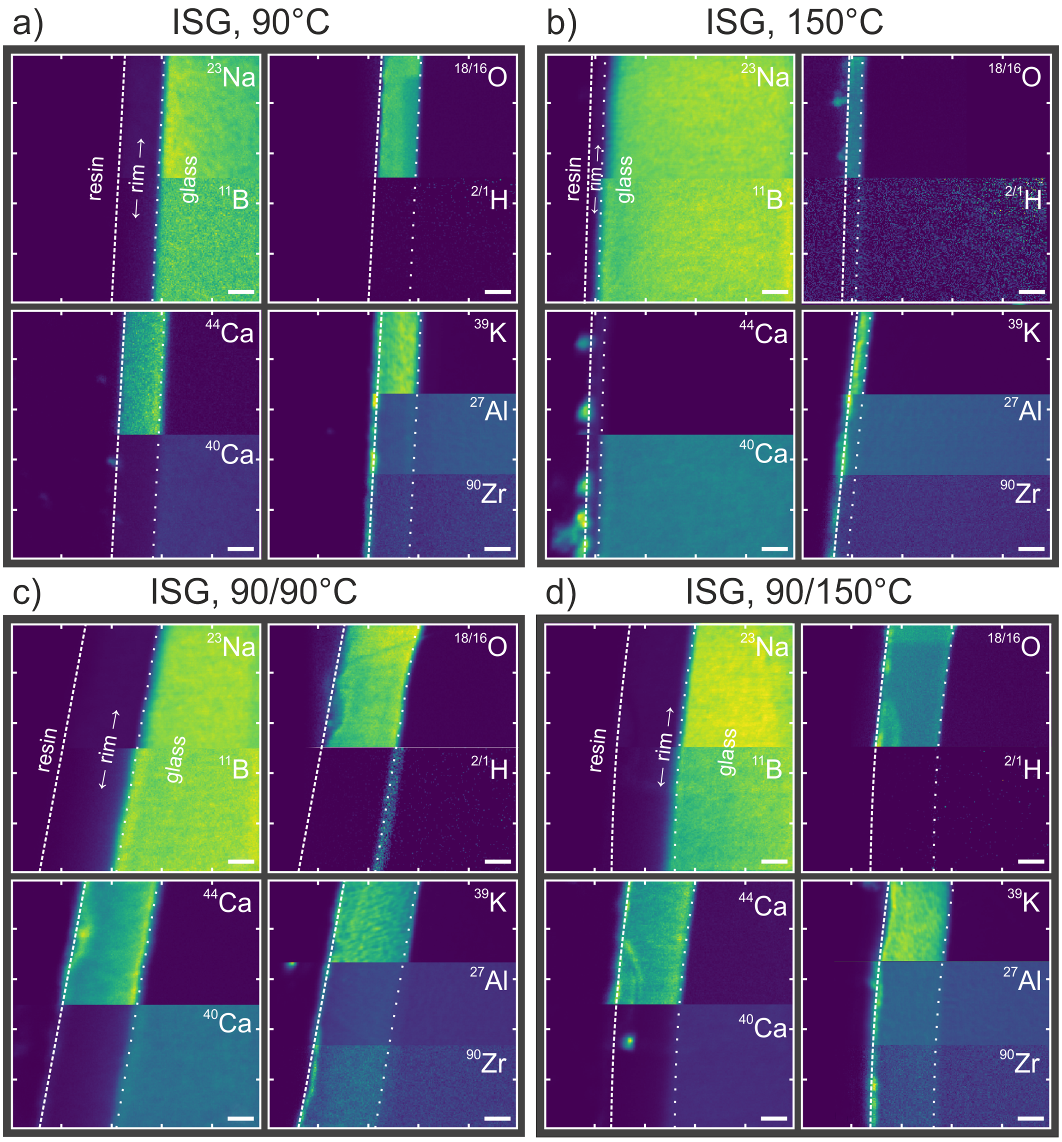

Figure 4.3: Montage of individual isotope distribution maps of corroded ISG samples obtained by NanoSIMS. Mapping areas are 10-by-10 µm^2, with each square here showing one isotope (ratio) in the upper and lower half (or thirds) of the same map. Dashed and dotted lines represent outer and inner corrosion rim interfaces defined by the ^{18}O/^{16}O profile. Scale bars = 1 µm.

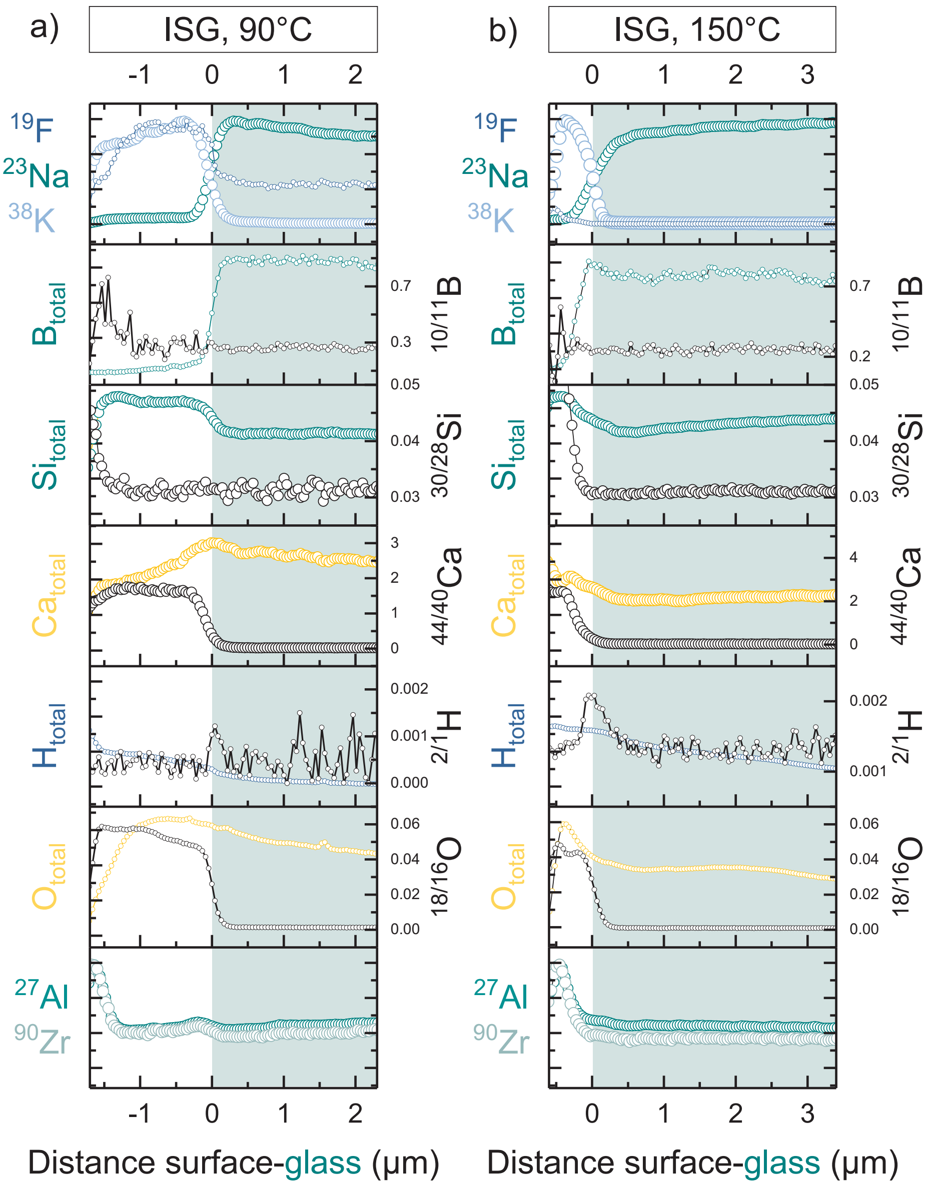

Figure 4.4: NanoSIMS profiles across corrosion rims of ISG altered at (a) 90 °C and (b) 150 °C over 3 months. Coloured Symbols represent normalized isotope counts (or sums of them), black circles and right ordinates represent isotope ratios. Origin of abscissa is set to the inflection point of the sigmoidal-shaped oxygen isotope ratio at the rim-glass interface. Symbol size represents estimated NanoSIMS probe diameter.

experiments, demonstrating that zirconium redistribution across the entire corrosion rim occurred, which was also observed under specific conditions by Gin et al. (2015a). Furthermore, only the ISG contains zirconium. Hence, a normalization to zirconium was not performed for the NanoSIMS data. The analysis of the tracer isotopes from solution revealed the following observations (see also Fig. 4.4a):

^{38}K: Potassium, used for the solution preparation, shows a anti-correlated profile to sodium.

^{19}F: Fluorine, dissolved from the PTFE lining of the reaction vessel, penetrates the entire corrosion rim with a sharp drop of intensity at the interface zone.

$^{10/11}$B: ^{10}B was introduced to the solution as tracer, but naturally 20 % of boron in the glass is also ^{10}B. In the corrosion rim a slight increase in the $^{10/11}$B ratio can be seen, but due to the low concentration of boron in the rim, the signal-noise ratio is quite low.

$^{30/28}$Si: Silicon isotope enrichment could not be detected within the corrosion rim, only at the surface of the corrosion rim. This coincides with recent findings by Gin et al. (Gin et al., 2015a) working on the same type of glass, but stands in contrast to results from isotope tracer studies on a ternary borosilicate glass (Geisler et al., 2015) and the French SON68 glass (Bouakkaz et al., 2016) (of which the ISG is the simplified version).

$^{44/40}$Ca: While the calcium isotopes show a concentration gradient within the corrosion rim, the $^{44/40}$Ca ratio plateaus over the range of the corrosion rim including the outer surface layer.

$^{18/16}$O: The oxygen isotope ratio gives a clear outline of the corrosion rim with sharp sigmoidal-shaped profiles on both sides. Note here again the lateral resolution of analysis is higher when using the Cs^{+} source.

$^{2/1}$H: Hydrogen isotopes reveal a rather unexpected behaviour While the ^{1}H shows a concentration gradient from high at the outer surface to low in the pristine glass, a weak intensity of the ^{2}H isotope could only be measured in the interface zone. In comparison to the other inbound tracer isotopes, the $^{2/1}$H peak is situated right in front of these in direction of the pristine glass body. D-H exchange in amorphous silica is highly surface area dependent (Suzuki et al., 2008). In accordance with Geisler et al. (2015), this finding indicates smaller silica spheres at the rim-glass interface than in the matured corrosion rim.

Comparing this tracer experiment on the ISG sample at 90 °C (Fig. 4.4a) to the one at 150 °C (Fig. 4.4b), the first observation will be the lower corrosion rim thickness as indicated by the ^{18}O isotope profiles (Table 4.1). As the tracer solution was saturated with respect to amorphous silica in the experiment at 90 °C, the degree of undersaturation at 150 °C allowed some initial forward dissolution of the pristine glass to take place, which explains the lower overall rim thickness (90 °C: 1.63(11) µm, 150 °C: 0.68(21) µm, Table 4.1). Further distinction and determination of the extend of individual zones in the corrosion rim suffer from signal overlap of apparent surfacial precipitates, corrosion rim and pristine glass due to the limited resolution of the analytical technique. However, following notes can be made: (i) fluorine has a strong intensity peak close to the sample surface and a smaller around the corrosion rim-glass interface. (ii) Based on the total concentrations of silicium, calcium, oxygen, and their respective isotope tracers two zones can be differentiated, an outer surface zone with strong tracer uptake and an inner corrosion rim zone, where ^{30}Si could not be detected, but ^{44}Ca and ^{18}O have infiltrated the rim. (iii) Deuterium again could only be detected at the rim-glass interface. Unfortunately, the analysis of the third set of isotopes including ^{27}Al and ^{90}Zr failed due to misalignment of mapping stage and the beam focus during the automated run.

Looking at the precorroded samples (Fig. 4.5), further observations can be made: (i) fluorine can be detected in the corrosion rim-glass interface zone in the 90 °C experiment, but only close to the surface in the 150 °C experiment, and (ii) no elemental or isotopic anomaly (e.g., low ^{18}O indicates the precorroded section of the rims). In comparison to the previously untreated samples, naturally the width of the corrosion rim is larger, but more importantly, the calcium isotope ratio shows a mixing signal of inbound ^{44}Ca and outwards moving ^{40}Ca.

Behaviour of mobile elements in other glass samples

Sodium shows a sigmoidal profile at the corrosion rim-glass interface throughout all experiments and glasses (Fig. 4.4-4.10), whereby its concentration is below the detection limit within the corrosion rim. The other well soluble glass constituent, i.e., boron, also shows a sigmoidal profile (in most cases) at the interface, but always with a tailing extending into the corrosion rim. The tailing is more pronounced in precorroded samples. However, in experiments with the quaternary QBG glass (Al-Na-B-Si) at 150 °C, boron is equally retained in the newly formed (section of the) corrosion rim. Specifically, the precorroded experiment at 150 °C gives the evidence for previous corrosion in the original, non-tracer solution: (i) boron intensity drops in the centre of the corrosion rim at approx. $-1.73\,\mu m$ from the rim-glass interface; (ii) at the same time, the intensity of calcium, originating only from the tracer solution, peaks around the same area.

Potassium, being introduced into the solution by the silica preparation, is always detected within and up to the interface zone, i.e., at the rim-glass interface, where it builds anticorrelated sigmoidal profiles with sodium. Similar to calcium and boron, the distribution of K also marks the two rim sections in the experiment with precorroded QBG at 150 °C.

The probably most mobile isotope deuterium (^{2}H), added to the solution as tracer, can only be found in the rim-glass interface zone. The maximum of the peak intensity though is slightly offset into the pristine glass in regard to the rim-glass interface defined by the ^{18}O profiles, and falls back to zero within a measurement steps. Unexpectedly, the corrosion rim itself reveals no deuterium signal, whereas, ^{1}H can be detected, which to an unknown fraction originated from the embedding resin.

Thus, while mobile species like sodium, potassium, deuterium and oxygen have clearly traversed the whole corrosion rim, calcium and boron mobility was controlled by some property of the corrosion rim and/or pore solution.

Behaviour of network former

Total silicon shows in all experiments a relative enrichment in the corrosion rim in comparison to the pristine glass, which is expected due to the higher ionization proneness of the hydrated species in the corrosion rim. The silicon isotopic composition changes merely in the surface regions, where silica condensation from the ^{30}Si containing solution may occur, which is in accordance with experiments on the ISG glass at similar conditions performed by Gin et al. (Gin et al., 2015a). However, this does not rule out silicon from the bulk solution entering the corrosion rim and isotope exchange to occur during glass corrosion in general as experiments on a ternary borosilicate glass by Geisler et al. (Geisler et al., 2010) reported corroded glass samples showing both, isotopically normal and enriched corrosion rims. In conclusion, this apparent contradiction was attributed

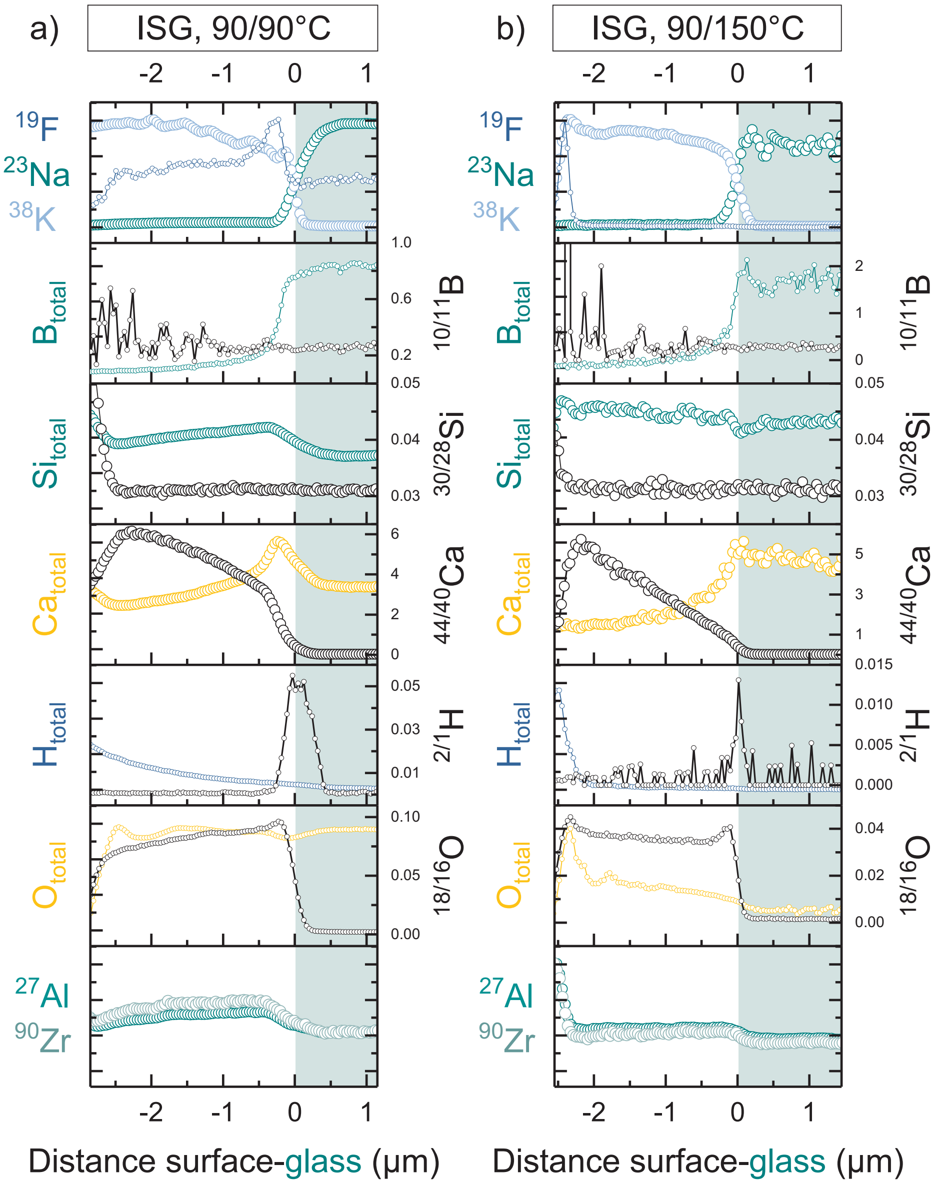

Figure 4.5: NanoSIMS profiles across corrosion rims of precorroded ISG altered at (a) 90 °C and (b) 150 °C over 3 months. Coloured Symbols represent normalized isotope counts (or sums of them), black circles and right ordinates represent isotope ratios. Origin of abscissa is set to the inflection point of the sigmoidal-shaped oxygen isotope ratio at the rim-glass interface. Symbol size represents estimated NanoSIMS probe diameter.

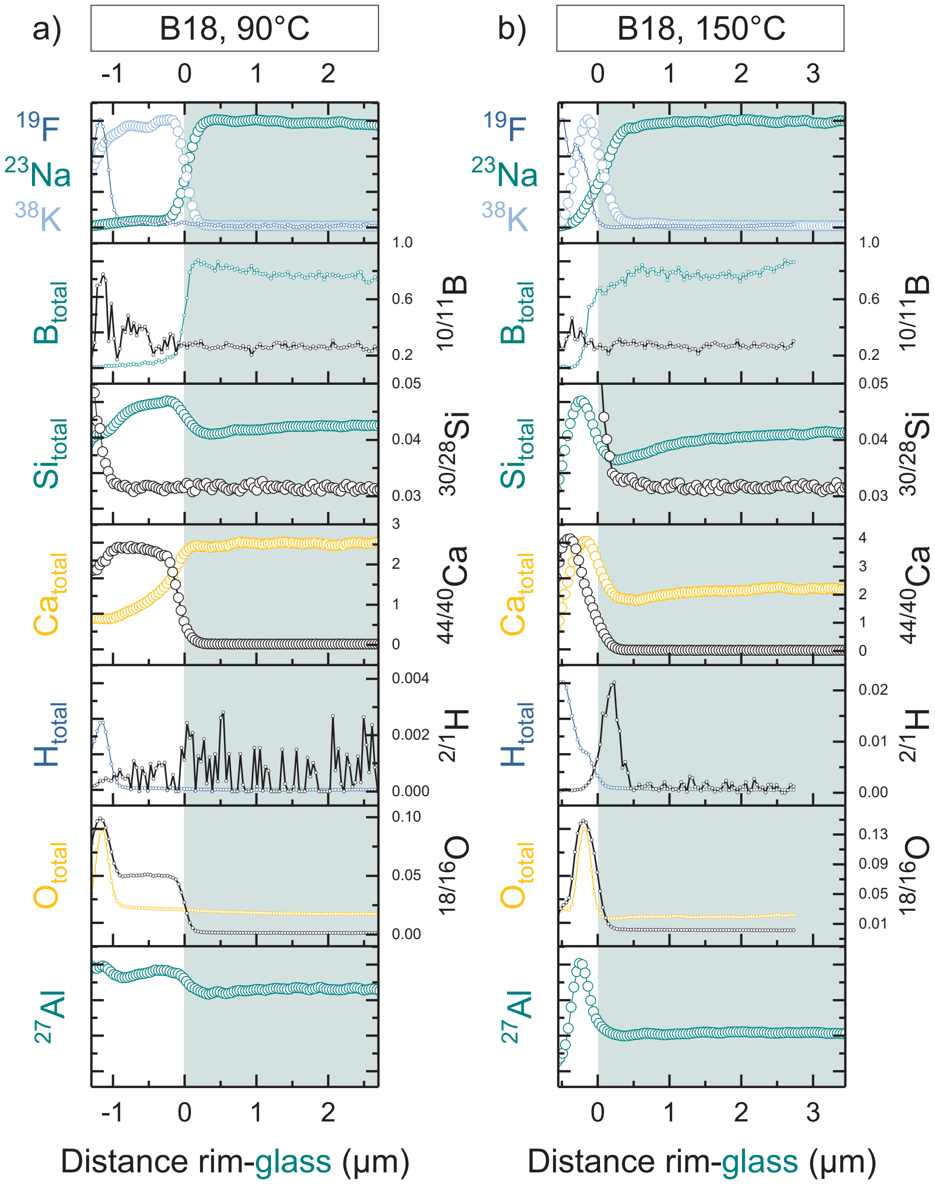

Figure 4.6: NanoSIMS profiles across corrosion rims of ISG altered at (a) 90 °C and (b) 150 °C over 3 months. Coloured Symbols represent normalized isotope counts (or sums of them), black circles and right ordinates represent isotope ratios. Origin of abscissa is set to the inflection point of the sigmoidal-shaped oxygen isotope ratio at the rim-glass interface. Symbol size represents estimated NanoSIMS probe diameter.

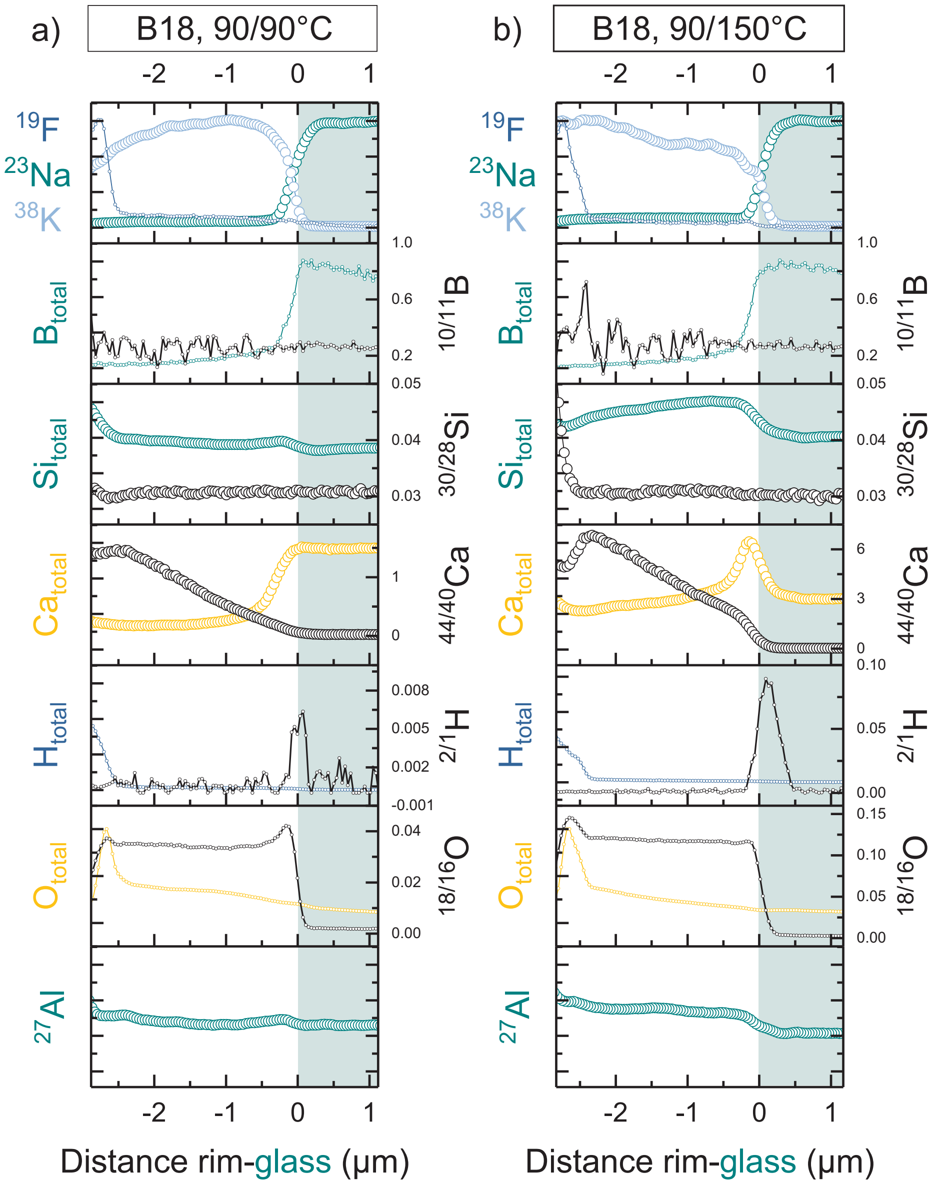

Figure 4.7: NanoSIMS profiles across corrosion rims of precorroded B18 altered at (a) 90 °C and (b) 150 °C over 3 months. Coloured Symbols represent normalized isotope counts (or sums of them), black circles and right ordinates represent isotope ratios. Origin of abscissa is set to the inflection point of the sigmoidal-shaped oxygen isotope ratio at the rim-glass interface. Symbol size represents estimated NanoSIMS probe diameter.

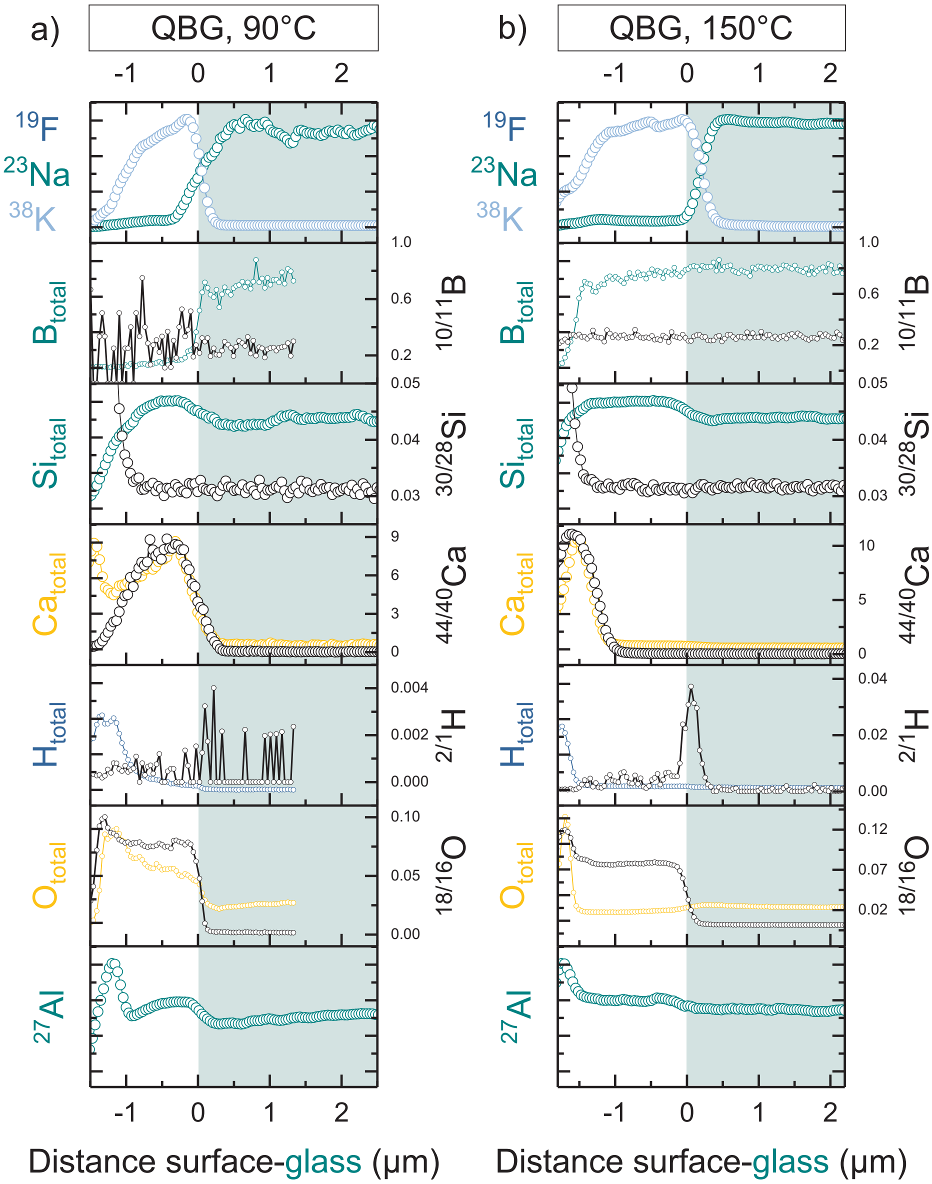

Figure 4.8: NanoSIMS profiles across corrosion rims of QBG altered at (a) 90 °C and (b) 150 °C over 3 months. Coloured Symbols represent normalized isotope counts (or sums of them), black circles and right ordinates represent isotope ratios. Origin of abscissa is set to the inflection point of the sigmoidal-shaped oxygen isotope ratio at the rim-glass interface. Symbol size represents estimated NanoSIMS probe diameter.

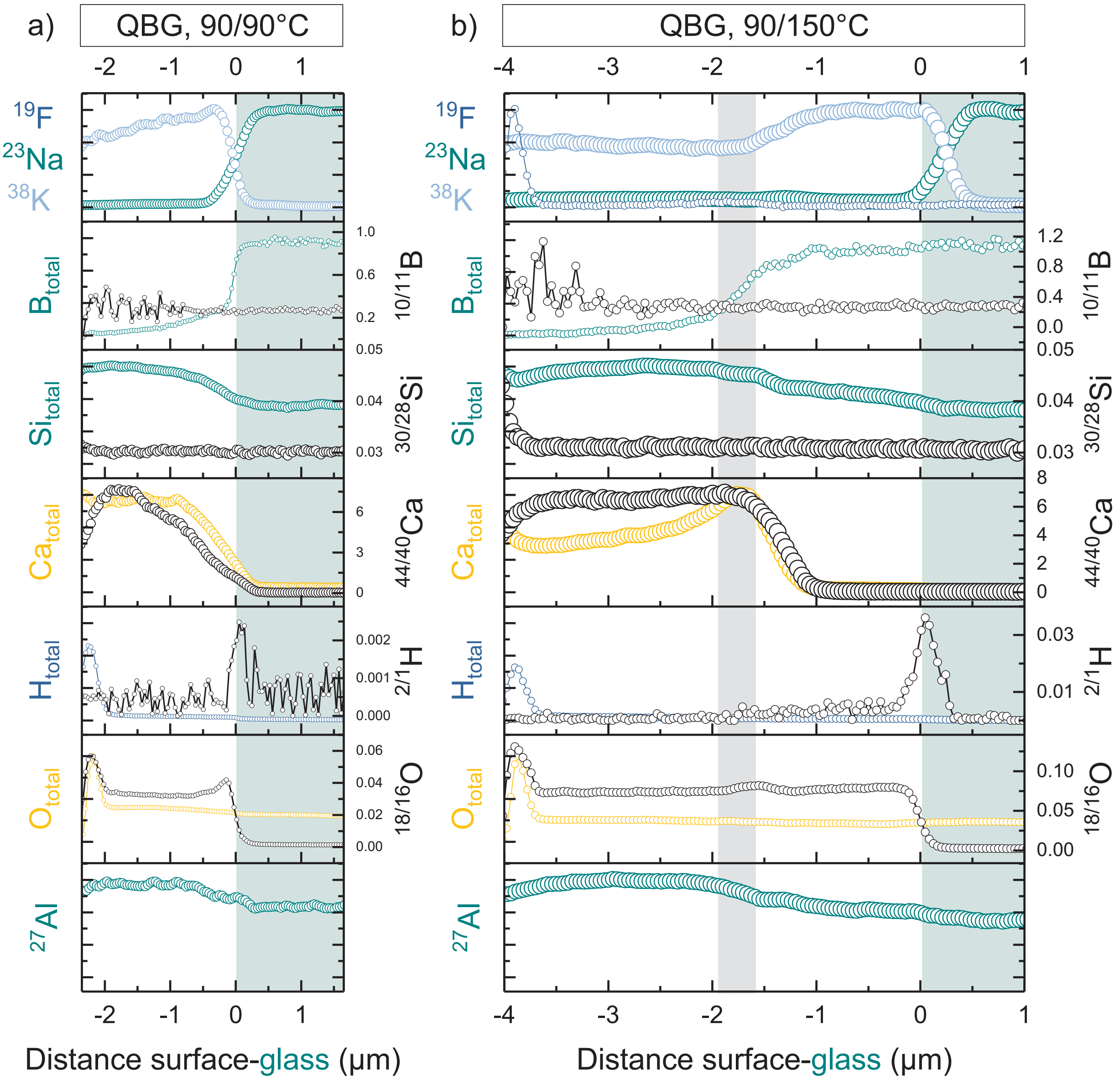

Figure 4.9: NanoSIMS profiles across corrosion rims of precorroded QBG altered at (a) 90 °C and (b) pristine TBG 150 °C over 3 months. Coloured Symbols represent normalized isotope counts (or sums of them), black circles and right ordinates represent isotope ratios. Origin of abscissa is set to the inflection point of the sigmoidal-shaped oxygen isotope ratio at the rim-glass interface. Symbol size represents estimated NanoSIMS probe diameter.

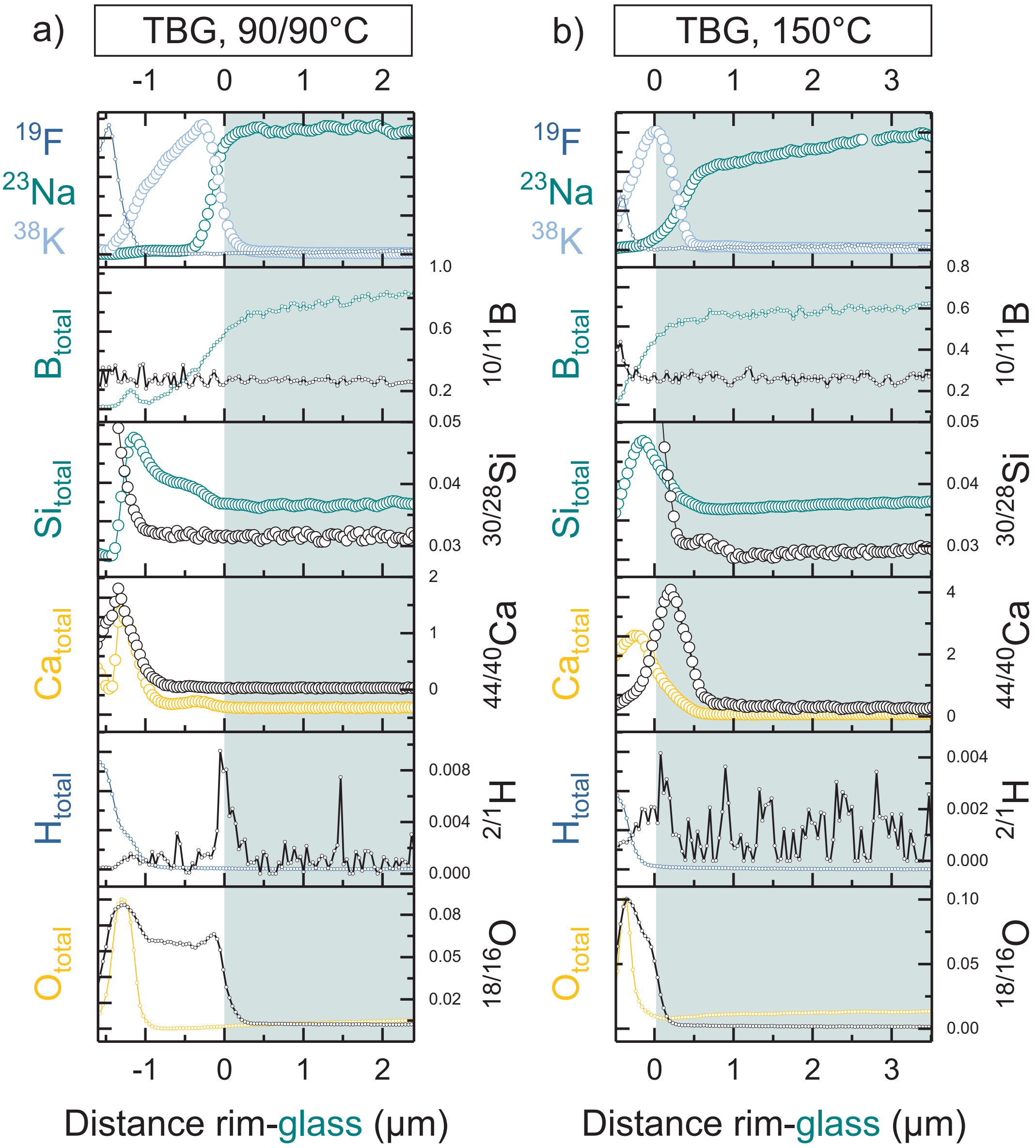

Figure 4.10: NanoSIMS profiles across corrosion rims of TBG altered at (a) 90 °C and (b) 150 °C over 3 months. Coloured Symbols represent normalized isotope counts (or sums of them), black circles and right ordinates represent isotope ratios. Origin of abscissa is set to the inflection point of the sigmoidal-shaped oxygen isotope ratio at the rim-glass interface. Symbol size represents estimated NanoSIMS probe diameter.

to the (individual) density and structure of the silica-rich corrosion rims controlling the accessibility and mobility of ions inside the corrosion rim. Aluminium and zirconium, as already observed with the 90 °C ISG experiment (Fig. 4.4) show no noticeable variations in the other experiments beside slightly higher intensities in the corrosion rim (likely due to ionization proneness) and intensity peaks at the surface (likely due to surface precipitates). Intensity peaks at the surface are normally ascribed to secondary phase precipitation of previously dissolved glass constituents, but no secondary phases could be detected by Raman spectroscopy. However, hydroxides (e.g., $Al(OH)_3$) are poor Raman scatterers and as such may have stayed undetected (especially if only present in low abundance).

Oxygen isotope exchange

The $^{18/16}O$ ratios were averaged over the plateau-like regions of the corrosion rim in the NanoSIMS profiles (values and number of averaged pixels given in Table 4.1). Beside

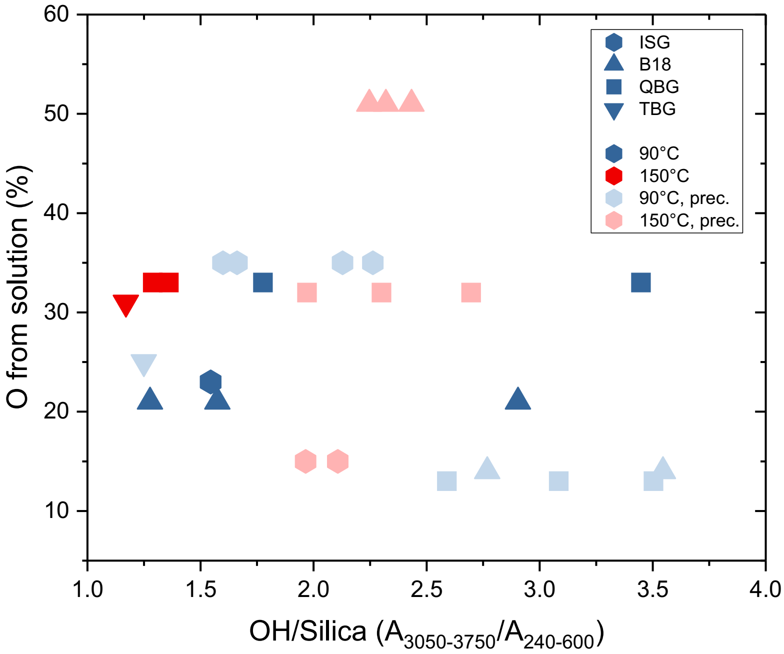

Figure 4.11: Fraction of oxygen originating from solution vs. relative water content in corrosion rim. The relative water content is derived as ratio of the integrated Raman scattering intensities of water and OH bands (3050-3750 cm^{-1}) and the silica intensity (240-600 cm^{-1}). Sample spots with OH/silica ratios below 1 are considered to contain no measurable water (due to the stronger Raman scattering cross-section of water).

one outlier (B18, 150 °C), most samples show stable ratios across the entire corrosion rim (Fig. 4.4-4.10). Assuming a linear mixture between oxygen from the glass with that from the bulk solution (initial $^{18/16}$O ratio $\approx$ 0.231), the isotope exchanges results in a range of 14 to 51 % of ^{18}O atoms originating from solution. Despite staying under high vacuum in the NanoSIMS for several days, to exclude the possibility to merely have measured ^{18}O-rich pore water in the corrosion rim, oxygen isotope values were checked against the intensity of water and OH bands measured by Raman spectroscopy. Raman analyses were performed on the surface of the corroded glass samples before NanoSIMS analysis, but the depth resolution with semi-transparent materials and the low thickness of the corrosion rim should allow for a relative estimate of the water/OH content. To correct for background and fluorescence, the water/OH intensities (3015 to 3715 cm^{-1} were normalized by division of the silica signal (240 to 600 cm^{-1}. A correlation between water/OH content and oxygen isotopic composition is not developed (Fig. 4.11).

4.3.3 The rim-glass interface

FIB sections across the whole corrosion rim and reaction interface were taken from two of the cross-sectioned precorroded samples, the 90 °C ISG and 150 °C QBG, to investigate the corrosion rim structure and the elemental distribution at the rim-glass interface with higher spatial resolution. A closer look at the reaction interface of the precorroded 90 °C ISG sample reveals the following phenomena: (i) the corrosion rim is characterized by a porous structure. Whether the visible pores are interstitial pores between silica spheres as proposed by Geisler et al. (2015) or secondary porosity in a gel-like material cannot not be stated with certainty due to the limits of the spatial resolution. (ii) A dense layer of about 100 nm thickness characterized by a high Z-contrast has formed between corrosion rim and pristine glass. While the transition of the corrosion rim into the dense layer seems to be continuous, the boundary of this layer to the pristine glass appears sharp within a few nanometres as for a phase boundary. EDX analyses from this region (Fig. 4.12a,f) confirm the previously made observations of element and isotope distributions around the reaction interface, but can be less ambiguously described at higher resolution. Sodium is characterized by the sigmoidal profile within the first few hundred nanometres of

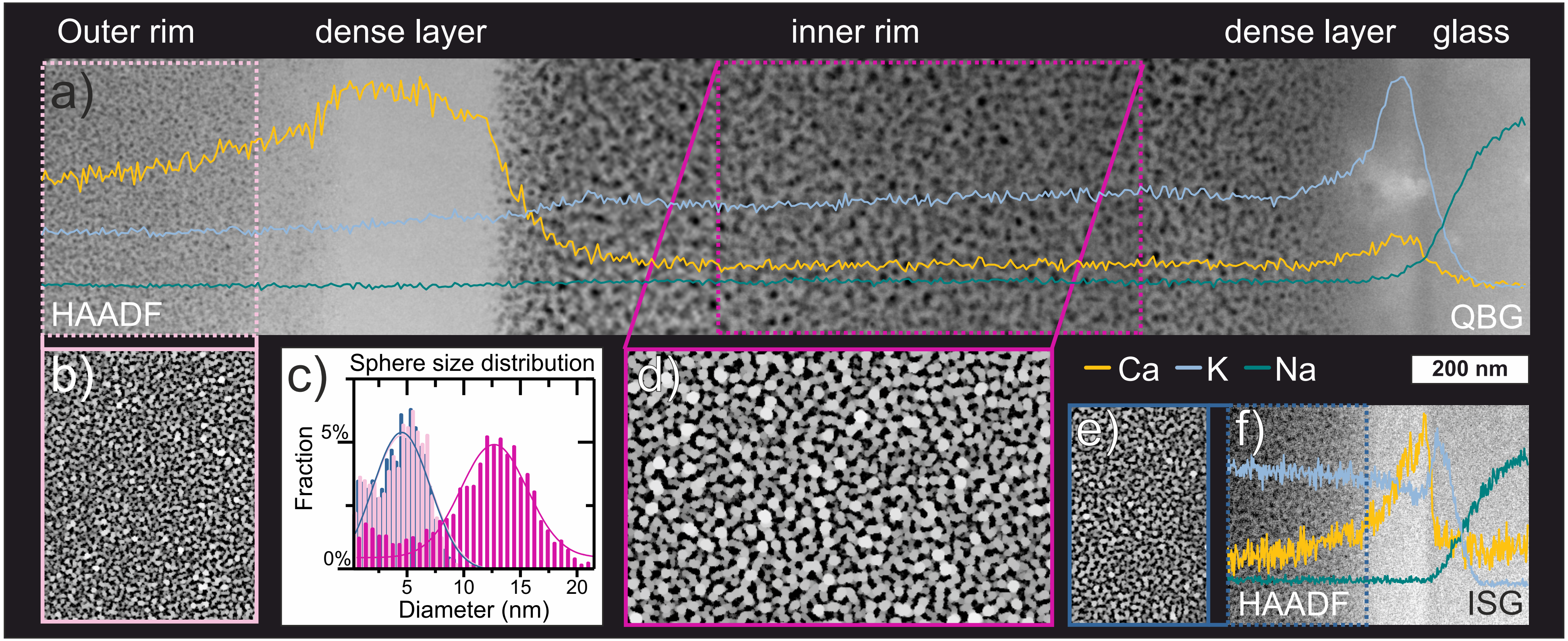

Figure 4.12: High-angle annular dark field (HAADF) STEM imaging and STEM-EDX analyses of corrosion rim-glass interface of precorroded samples (ISG (90/90 °C and QBG 90/150 °C). **a)** HAADF (panorama) image of precorroded QBG sample (rendered by image stitching), revealing two sections of the corrosion rim and superimposed EDX profiles (averaged from EDX maps (not shown here)). **b-e)** Sphere size analyses of corrosion rim (section), which was performed on HAADF STEM images of the porous sections (see dashed rectangles) with the *ImageJ/Fiji* software package (Schindelin et al., 2012) by first applying a FFT band pass filter to minimize illumination effects followed by an estimation of the sphere size diameter with a brightness threshold and the *Local Thickness* function. The latter is a routine finding the maximum diameter of spheres fitting into a given structure (b, d, e). **c)** Histograms of sphere size distribution fitted with Gauss functions. **f)** HAADF image and superimposed EDX profiles for precorroded ISG sample.

the glass itself. The intensity of potassium spikes right behind the interface, reaching approximately 100 nm into the glass. However, calcium concentrations increase from the corrosion rim towards the interface with no Ca signal from the underlying glass body. The position of the calcium intensity peak correlates well with the extend of the high Z-contrast zone between rim and glass seen in Fig. 4.12f. The remaining measured elements show no further anomalies. Whereas the precorroded ISG sample shows no major chemical or structural heterogeneities throughout the corrosion rim, TEM(-EDX) analysis of the second precorroded sample, the quaternary QBG glass which was corroded at 150 °C during the isotope tracer phase, exhibits two distinct reactions zones in the corrosion rim. HAADF imaging reveals porosity of two size distributions with about three times larger silica spheres in the inner part formed at 150 °C (Fig. 4.12b-d), which are divided by an approximately 300 nm wide dense zone that is similar to the high Z-contrast zone at the rim-glass interface also seen in the ISG sample. Furthermore, the pore size again seems to increase from the rim-glass interface towards the rim. The extend and position of these layers correlate well with the chemical profiles obtained by NanoSIMS (Fig. 4.9b) and TEM-EDX analysis (Fig. 4.12a), showing that the inbound transfer of calcium stopped at the first dense layer, while potassium penetrates through the entire corrosion rim and the outbound boron is retrained in the newly formed corrosion layer.

4.4 Discussion

The here presented results from new corrosion experiments are in general agreement with results reported in the recent literature. Glass compositions, pH and solution saturation, and overall experimental setup and analysis technique often vary from study to study. For this reason, the ISG glass is now used as a reference and benchmark glass. Concentration profiles of typically analysed elements like boron and sodium here show similar sigmoidal shapes across the corrosion rim-glass interface as seen in experiments where the corrosion rim was analysed by other techniques like EMP or ToF-SIMS. Due to recent TEM and atomic probe tomography work (Gin et al., 2017; Hellmann et al., 2015), concluding that the so-called diffusion profiles possibly being an artefact of the insufficiently small probe size of previously used analytical techniques, the here presented results have to be discussed in this light. As ^{11}B was measured with both ion sources, it can be used to illustrate the dependence of the width of the sigmoidal profile across the rim-glass interface on the probe size (Fig. 4.13; see also Section 1.3.3, p. 20). While the caesium source allows for lateral resolutions of down to 50 nm, the oxygen source delivers about 100 to 150 nm. ^{11}B measured by caesium source appears - even-though noisier due to the worse ionization potential of normally positively charged glass constituents by the caesium ions - sharper than those profiles measured by the oxygen source. The probe size is crucial to correctly measure chemical profiles across the rim-glass interface to then draw conclusions concerning the underlying reaction mechanism. Recent atom probe tomography data from corroded ISG glass presented by Gin et al. (2017) are in strong contrast to their previous works with spatially lower resolving analytical techniques (e.g., Frugier et al., 2008; Gin et al., 2013a; Gin, 2014, and references therein), in which the rim-glass interface was perceived as sigmoidal-shaped ion profile and as a consequence interpreted as diffusion zone. The atomic resolution of the atom probe, however, revealed this interface to be a nanometre-sharp interface, which is in line with the ICDP model (Geisler et al., 2010; Geisler et al., 2015; Hellmann et al., 2012). The residual nanometre-wide transition zone (Gin et al., 2017) is no further interpreted by the authors as diffusion zone, but attributed to a nanometre-sized roughness of the interface, but a mechanistic origin for this is not presented. An interface roughness is, however, to be expected from any dissolution front, either in amorphous or crystalline systems. Numerous AFM studies on mineral crystals have shown that dissolution is facilitated along etch pitches, screw dislocation, and/or step edges of a surface, resulting in a multitude of possible geometric shapes of a dissolution front depending on the individual site's dissolution rates at given environmental conditions (e.g. C. V. Putnis and Ruiz-Agudo, 2013; Ruiz-Agudo et al., 2012; Ruiz-Agudo et al., 2014). This process is not stopped after congruent dissolution of the initial outer surface of the parent phase and precipitation of a daughter product via

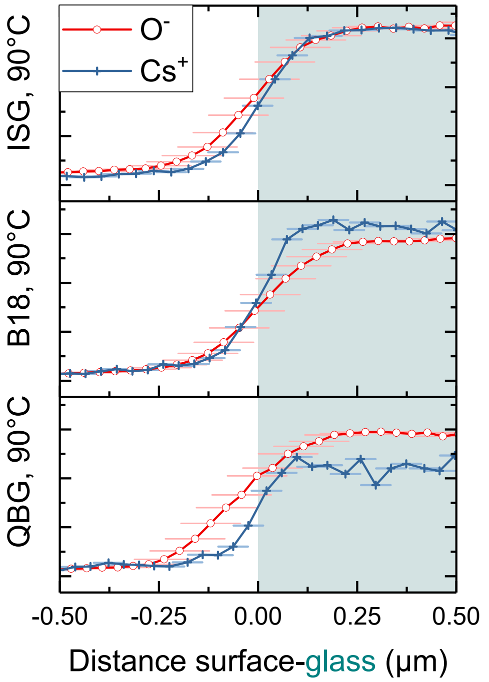

Figure 4.13: Comparison of exemplary (normalized) ^{11}B intensities measured by both ion sources at the corrosion rim-glass interface, showing the higher lateral resolution of the caesium source. Error bars represent the estimated probe sizes.

epitaxial growth, but congruent dissolution continues at an inward-receding surface of the parent phase. This continuously dissolving surface is what is called the reaction interface. Naturally, amorphous materials are lacking any long-range order and as such do not hold definite surface sites, i.e., terrace, step, or kink sites as found in crystals, at which dissolution could otherwise occur in an oriented manner Kossel, 1927; Stranski, 1928. However, if treating the disordered, not (crystal) lattice-like glass surface as an assemblage of differently coordinated and constrained structural units, e.g., Q^2 and Q^3 species, the surface can be depicted as holding pseudocrystallographic sites for dissolution (Dove et al., 2008). Less constrained Q^2 units are rapidly detached from a surface in contrast to the higher coordinated Q^3 units. Nonetheless, Q^3 will eventually be detached, but likely at heterogeneously distributed sites of an disordered glass surface, at which detachment is energetically preferred due to surface energy minimization. Hence, for further discussion the here reported rim-glass transitions (Fig. 4.4-4.10) should be regarded as sharp interfaces between corrosion rim and pristine glass with a nanometre-sized roughness.

4.4.1 Decoupling of (isotope) tracers

The atomically sharp boundary of the rim-glass interface might explain the decoupling of hydrogen and oxygen isotope tracers. In all measured samples with pristine and precorroded glass monoliths, the deuterium tracer is found directly ahead of the ^{18}O tracer. The oxygen isotope composition of the corrosion rim is a mixture of solution derived ^{18}O and ^{16}O originating from the original glass network indicates high fluid mobility across the corrosion rim. Highly solvable tracer isotopes from the solution like ^{44}Ca and ^{38}K were also detected abundantly in the corrosion rim, which is another indicator for thorough water transport across the corrosion rim. While all isotope tracers beside ^{30}Si penetrate the corrosion rim, only deuterium is measured within the pristine glass by NanoSIMS analyses. Gin et al. (2017) have performed a *post-mortem* exchange experiment by submerging a corroded sample in deuterium water at room temperature for 100 h. ToF-SIMS results show concentrations of deuterium up to the rim-glass interface, but count rates for both hydrogen species in the glass were below the detection limit. Deuterium count rates are also not high in the here presented NanoSIMS data, but a thin layer, enriched in deuterium, signals are above the background noise, is located directly behind the rim-glass interface. The seemingly quick exchange of hydrogen isotopes in the corrosion rim even at room temperature explains the lack of deuterium in the corrosion product observed in this study. Sample washing with distilled water has likely removed most deuterium by quick exchange of hydrogen with surfacial silanol groups from the open structure of the corrosion rim (see Suzuki et al., 2008). Nonetheless, deuterium was measured at the rim-glass interface with a small lateral offset from the ^{18}O. Misalignment of data coordinates from different measurement sessions can be excluded when comparing hydrogen and oxygen isotopes as they were measured simultaneously. Thus, deuterium was transported across the rim-glass interface into the pristine glass. Similarly, in one of two glass samples analysed by TEM-EDX, potassium was also detected within the pristine glass.

Treating the corrosion rim as endless reservoir for deuterium, which under the assumption of steady exchange of mobile ions between corrosion rim and bulk solution seems to be adequate, deuterium will diffuse into the pristine glass network from an atomically sharp reaction interface. The latter is by itself known to advance into the glass, at first at a fast initial and then in the following at a slower residual rate (see e.g., Van Iseghem and Grambow, 1987, Chapter 1, Section 1.3.2, p. 9). At the time of termination of the experiments, two rate scenarios for deuterium diffusion into the glass are possible: (i) a steady state between glass corrosion and deuterium diffusion is established, meaning that deuterium diffusion from in fact an interdiffusion-reaction front (Doremus, 1975) is advancing the corrosion interface at a roughly constant distance. With the continued corrosion of the pristine glass, the diffusion front is driven forward. (ii) By the time of experiment termination, the glass corrosion rate had been slowed down enough so that the diffusion of deuterium is faster than the movement of the dissolution interface, resulting in the occurrence of a diffusion front after all. The latter case would exclude any rate-limiting role of deuterium and hence protons in the glass corrosion process. The diffusion front is only a side effect, but, importantly, not rate-limiting. The second rate scenario is fully consistent and supported by a study of Gin et al. (2017), who showed that while the advance of the reaction interface dramatically slowed down, the diffusion of hydrogen continued evidenced by the broader hydrogen diffusion profiles.

4.4.2 Dense Interfacial Layer

While the oxygen and hydrogen isotope tracers revealed a decoupled behaviour from each other at the rim-glass interface, the calcium tracer exhibited a unique decoupling in the one experiment (QBG, precorroded, 150 °C), in which a dense layer within the corrosion rim formed (Fig. 4.9b, Fig. 4.12a).The calcium tracer could not penetrate though this layer. However, it is apparently not fully passivating to all ions as seen by penetration of the smaller solute ions of deuterium, oxygen, sodium, and potassium. The concept of a diffusion barrier (at the reaction interface) was postulated in the literature so far as a *passivating reaction interphase* (PRI) and is considered in the GRAAL model (Frugier et al., 2008; see also Section 1.3.2, p. 13) as it is assumed to control the corrosion rate. A dense layer in the centre of the corrosion rim was only observed in one of two samples analysed by TEM. The isotope profiles by NanoSIMS give no indication of any further dense layer formed like this. Comparing both TEM analysed samples, it appears that the thickness of the dense layer at the corrosion interfaces are similar, while the inner dense layer is twice as thick. The porosity of the outer part matches thereby that of the ISG sample, while it is larger in the inner part (Fig. 4.12c). The location of this inner-rim dense layer is most likely the point of corrosion advancement at the time of sample transfer to the tracer solution. For this, samples were removed from their original vessels and transferred into a new reaction vessels, containing the tracer solution at room temperature. A decrease in temperature will inevidently lower the solubility of dissolved species in the solution in the pore space (or a fluid film). Rapid deposition of phases like amorphous silica thereby may close up pore space for larger ions hindering their transport across this dense layer. In this instance, the effect of this semi-passivating layer is not only seen in isotope or elemental profiles, but also by comparison of the larger pore sizes in the latter part of the corrosion rim. It can only be speculated why only in the instance of this precorroded QBG sample a dense, passivating layer was observed within the corrosion rim, which has also about twice the thickness of the dense layer found at the rim-glass interface. In comparison to other glasses and their corrosion rims, the QBG glass is one of the glasses with a simple composition, and revealed the thickest corrosion rims. A higher corrosion rate equals faster release of sodium at the reaction interface into the confined interfacial and/or pore solution increasing the pH which in turn increases the silica solubility. Drastic decrease of temperature during termination of the experiment results in the precipitation of amorphous silica from a then supersaturated solution. As the precipitation, aggregation and growth of amorphous silica is complexly dependent on temperature, saturation, concentration of background electrolytes, and pH (Iler, 1979), the dense layers might have varying resistance to later re-dissolution and/or different permeabilities for ion transport.

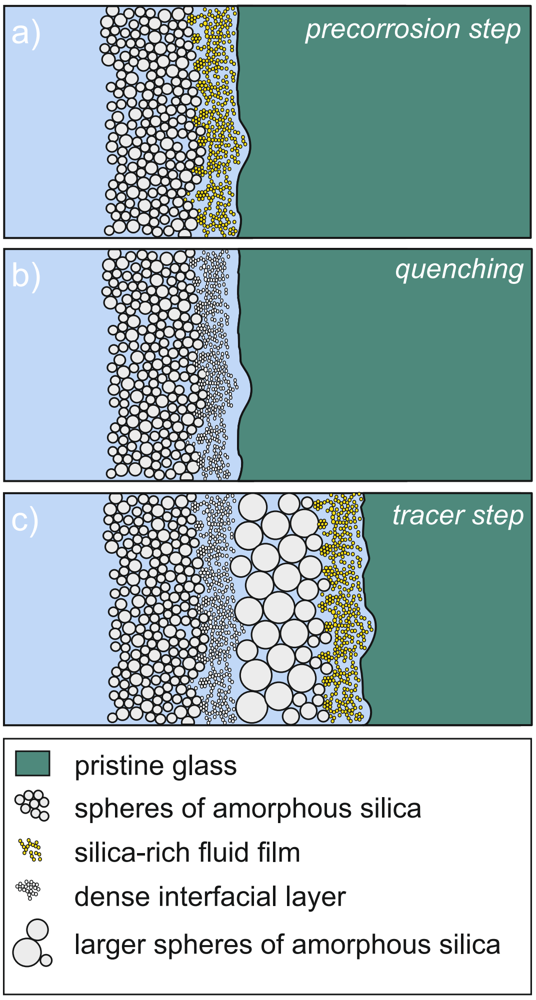

Figure 4.14: Sketch of proposed formation of inner dense layer. **a)** Coupled (congruent) dissolution of the pristine glass (green), saturation and nucleation of amorphous silica in the interfacial layer (yellow spheres), and precipitation of silica spheres (grey) building up the corrosion rim (during the precorrosion step). **b)** Interruption of experiment for samples transfer in tracer solution quenches and densifies the silica-rich interfacial solution (small grey spheres). **c)** Continuation of coupled dissolution-reprecipitation, whereby the difference in the chemical environment conditioned by the partial shielding of the inner quench layer resulted in different sphere morphology.

The pristine QBG glass contains only a minor contamination of calcium (Table 4.1). TEM-EDX clearly shows abundant calcium in the outer part of the corrosion, but also a smaller amount within the inner part (Fig. 4.12), suggesting that it must have been imprinted into the corrosion rim during the late tracer period of the experiment. In both cases the calcium intensity peaks in the respective dense layer, implying that the dense layer cannot be originate from a calcium phase as the inner dense layer predates the calcium input during the tracer stage.

The (sudden) local formation of a dense layer and the porosity difference is hard to explain by diffusive ion exchange and consequent glass network reconstruction. A more elegant explanation is the dissolution-precipitation-based model proposed by Geisler et al. (2010; 2015): (i) The dense layer deposits from a silica-saturated, water-rich layer or fluid film by rapid temperature during quenching the precorrosion experiment (Fig. 4.14), (ii) after which the dense layer acts as a selective diffusion barrier, allowing for a different chemical environment in the second part of the corrosion experiment. As indicated by the blocked calcium ions, pore space solution chemistry should be different between both layers, i.e., pH, saturation states and background electrolytes.

After Iler (1979) the growth of individual silica spheres is amongst others increasing with increasing pH values by Ostwald ripening, which then again results in larger interstitial pore space.

4.4.3 Oxygen exchange

While mobility of calcium is seemingly affected by the inner dense layer, water transport occurred throughout the entire corrosion as indicated by he oxygen isotope profiles (Fig. 4.4-4.10). Almost all experiments reveal constant $^{18/16}$O isotope ratios across the corrosion rim, which shows abundant isotopic exchange between solution and solid as modelled by Geisler et al. (2015), assuming (i) silica saturation at the solution-solid interface, (ii) a constant corrosion rate, i.e., a steady advance of the dissolution-reprecipitation front, (iii) a constant pore fraction in the corrosion rim (about 30%), (iv) varying reactivity of silica with the state of maturation/growth (simplified as distance from the reaction interface), and (v) changing water diffusion coefficients based on the location within the corrosion rim, i.e., low diffusivity at the reaction interface. In contrast to Geisler et al. (2015), however, the oxygen isotope ratio of those corrosion rims formed in isotopically unlabelled solution during the precorrosion stage has fully re-equilibrated by the second experimental stage in the tracer solution. The glass composition cannot be the deciding factor to explain the different re-equilibration behaviour, as the re-equilibration is observed across all compositions, including the TBG also used in the study of Geisler et al. As such, the reactivity of the amorphous silica must somehow differently between those otherwise similar experiments.

As listed in Table 4.1, the $^{18/16}$O ratio of the corrosion rim spreads from 0.03263(12) to 0.11791(24) with the calculated ratio of the tracer solution being ~0.231 and ~0.002 for the pristine glass. In natural systems, amorphous silica is fractionating oxygen isotopes by a preferential uptake of the heavy ^{18}O isotope during precipitation (Kita et al., 1985). Leng and Barker (2006) pointed out that surfacial silanol groups are readily exchanging oxygen with surrounding solution, hence have to be eliminated for analysis of oxygen isotopes as climate proxies. As mentioned before, no correlation between the relative OH/water content of the silica layer and the $^{18/16}$O ratio was observed, which indicates that the measured ^{18}O must have originated from the solid material and not solely from surfacial silanol groups or adsorbed water. It cannot be stated to what extend distilled water from the sample rinsing after termination of the experiments interchanged with surfacial silanol groups and therefore altered the oxygen isotopic signature. Considering that the surface area of silica should correlate with such an exchange, the constant $^{18/16}$O ratio across the whole corrosion rim in the QBG experiment (Fig. 4.12a) characterized by two different porosities stands in contrast to surface size dependent alteration. Furthermore, the different $^{18/16}$O ratios between experiments neither show any correlation with the width of the corrosion rim, run temperature, or concentration of any of the initial glass constituents. Thus, the differences in oxygen isotope ratios of the corrosion rims between experiments cannot be explained here, but possible reflects the individual reactivity of the amorphous silica as modelled by Geisler et al. (2015).

4.4.4 Impact on formulation of the corrosion mechanism

Several observations made in this study and other recent studies challenge the available corrosion models. First of all, the findings of an nanometre-sharp reaction interface made by Hellmann et al. (2015) and Gin et al. (2017) questions the long assumed concept of a continuous ion exchange-based transition from pristine glass to a silica gel reaction rim (Chapter 1, Section 1.3.2, p. 9). On the other hand, the here presented combined results of NanoSIMS and TEM analyses suggest that deuterium and potassium diffused from the nanometre sharp reaction interface into the pristine glass. TEM-EDX furthermore revealed a sigmoidal-shaped concentration profile of potassium behind the reaction interface (Fig. 4.12a,f). Previous ToF-SIMS studies also reported sigmoidal-shaped profiles in the reaction zone (Gin et al., 2015a; Gin et al., 2015a), but the spatial definition of the reaction interface was different. However, the before mentioned APT studies reveal for most elements a sharp change in intensity at the nanometre-sized interface. Nonetheless, specifically the mobile alkalis elements are prone to evaporation loss, whereas hydrogen is apparently not affected (Gin et al., 2017). Thus, at least the glass network is corroding along a sharp interface, while the exact behaviour of network modifiers has still to be determined. The recent discussion about the actual corrosion mechanism inherits the underlying question whether all glass network bonds are being broken during corrosion or if a 'skeletal' remnant of the strongest bonds is retained, which then later restructures to form a silica-rich gel. In the latter case, network modifiers like the alkalis are assumed to be removed by ion exchange with inbound hydrogen in the form of protons. Having a nanometre sharp reaction interface would mean that the ion exchange zone or at least the *restructuring* zone must lie within this dimension.

It was argued above that the dense layers at the reaction interface must be a quenching product and therefore have been formed from a silica-rich fluid phase or hydrogel. Thus far the applicability of the dissolution-precipitation model proposed by Geisler et al. (2010; 2015) was often discarded because of the lack of a fluid films at the reaction interface of corroded samples (Gin et al., 2017, and references therein). The occurrence of dense interfacial layers of similar scale as reported here has been observed before and interpreted as PRI or more recently as layer of hydrated glass (Gin et al., 2013a; Guittonneau et al., 2011). The mechanistic concept of hydrated glass as transitional phase between pristine and corroded glass is no more justifiable in light of the inner dense layer found in the QBG sample, which is otherwise texturally and chemically similar to the dense layers found at the reaction interface. Quenching an experiment cannot explain how the progress of the proposed glass transition by recombination of silanol groups of the hydrated glass to siloxane bridges ($\equiv$Si-OH + HO-Si$\equiv$ $\rightarrow$ $\equiv$Si-O-Si$\equiv$ + H_2O) can be permanently stopped in this layer. However, a quench phase precipitated from a fluid (super-)saturated with respect to amorphous silica will inevitably have a varying chemical and structural properties depending on exemplary the fluid composition. Hence, this thin layer might re-dissolve during the continued glass corrosion process or, if stable, might provide semi-passivating properties as observed in the QBG experiment.

Apart from extensive pattern formation, experiments with less corrosion-resistant glasses often reveal a dense layer on the micrometer scale at the reaction interface, which in some cases detached from the glass body (e.g. Dohmen et al., 2013; Sterpenich and Libourel, 2001; Schalm and Anaf, 2016). The resulting gap between corrosion rim and pristine glass has previously been interpreted as the space which contained the interfacial fluid film before terminating the experiment (Dohmen et al., 2013; Geisler et al., 2010). In some cases, similar gaps can also be observed in mineral replacement reactions (e.g., Pöml et al., 2007; Kasioptas et al., 2011; Kusebauch et al., 2015; Pedrosa et al., 2016). However, in many natural and experimental samples of such replacements governed by coupled dissolution-precipitation a fluid film has not yet been observed at the nanometre scale (A. Putnis, 2002), but reaction interfaces are often well depicted by pore structures (Hövelmann et al., 2010). The *in situ* experiment (Chapter 3, p. 57) showed that a water- and silica-rich layer exists between the corrosion rim and pristine glass during the corrosion process, which in the dried state detaches from the (assumingly) nanometre-sharp interface of the pristine glass due to volume shrinkage. It appears that the thickness of the dense layer and therefore the distance between corrosion rim and pristine glass can vary in orders of magnitude, which could be controlled by total and/or relative solubility of educt and product, (interface) solution chemistry (pH, silica saturation state, background electrolyte (concentration)), glass corrosion rate, and/or permeability of the corrosion rim.

4.5 Conclusions

The here presented tracer experiments provide strong evidence for a dissolution-precipitation-based glass corrosion mechanism. First of all, high resolution TEM images and EDX maps revealed a sharp boundary between the corrosion rim and pristine glass. The interface region is hereby characterized by a distinct thin dense layer situated between glass and porous corrosion rim. HAADF images and TEM-EDX show sharp contrast in Z-contrast and element distribution around the dense layer-glass transition, which is less pronounced between corrosion rim and dense layer. Isotope distributions obtained by NanoSIMS show that water, as indicated by the oxygen tracer (^{18}O), penetrates the corrosion rim and reaches the rim-glass interface, at which point deuterium decouples from the oxygen tracer and diffuses into the pristine glass. Such distinct segregation of isotope tracers requires a sharp interface on the atomic scale, which is only provided by the dissolution-precipitation model (Geisler et al., 2010; Geisler et al., 2015; Hellmann et al., 2012). Nevertheless, the (inter-)diffusion of hydrogen/deuterium into the pristine glass needs ion exchange to keep the charge balance (Doremus, 1975).

The preservation of an amorphous dense layer at the centre of a corrosion rim, which was found in a precorrosion experiment and strongly resembles those layers encountered at the corrosion rim-glass interface, questions previous interpretations of such layers to be a (passivating) transitional phase between glass and corrosion rim (Cailleteau et al., 2008; Frugier et al., 2008). If these dense layers would be one link in a continuous reaction chain of glass hydration, ion exchange and *in situ* restructuring into a gel phase, the dense inner layer should have not been preserved as is, but it should have been further reacted to a gel phase as well. Furthermore, a general passivating character cannot be attributed to the dense layers, as chemical profiles of the dense inner layer reveal only transport limitations for calcium within the corrosion rim, but not for water or other ions. As such, these dense must have formed from quenching a silica-saturated interfacial (pore) solution, which is a result of silica accumulation at the reaction interface by congruent glass dissolution and slow silica transport across the corrosion rim. The dense inner layer is hereby a quench phase induced by the interim temperature drop during the solution change.

Additionally, the oxygen tracer indicated the corrosion rim to be reactive even after formation. The older, outer rim layers of the precorroded samples reveal the same altered oxygen isotope ratios like the newly formed rims. This further implies that there was sufficient water transport and exchange over the entire corrosion rim to equilibrate the oxygen isotopes.

These observations cannot be explained (solely) by any diffusion-driven corrosion model.

4.6 References

Ait Chaou, A., A. Abdelouas, Y. El Mendili, R. Bouakkaz, S. Utsunomiya, C. Martin, and X. Bourbon (2015). "Vapor Hydration of a Simulated Borosilicate Nuclear Waste Glass in Unsaturated Conditions at 50 °C and 90 °C". In: *RSC Advances* 5.79, pp. 64538–64549. ISSN: 2046-2069. DOI: `10.1039/C5RA12384D`.

Bouakkaz, R., A. Abdelouas, Y. El Mendili, B. Grambow, and S. Gin (2016). "SON68 Glass Alteration under Si-Rich Solutions at Low Temperature (35–90° C): Kinetics, Secondary Phases and Isotopic Exchange Studies". In: *RSC Advances* 6.76, pp. 72616–72633.

Bunker, B. (1994). "Molecular Mechanisms for Corrosion of Silica and Silicate Glasses". In: *Journal of Non-Crystalline Solids* 179, pp. 300–308.

Cailleteau, C., F. Angeli, F. Devreux, S. Gin, J. Jestin, P. Jollivet, and O. Spalla (2008). "Insight into Silicate-Glass Corrosion Mechanisms". In: *Nature Materials* 7.12, pp. 978–983. ISSN: 1476-1122, 1476-4660. DOI: `10.1038/nmat2301`.

Dohmen, L., C. Lenting, R. O. C. Fonseca, T. Nagel, A. Heuser, T. Geisler, and R. Denkler (2013). "Pattern Formation in Silicate Glass Corrosion Zones". In: *International Journal of Applied Glass Science* 4.4, pp. 357–370. ISSN: 20411286. DOI: `10.1111/ijag.12046`.

Doremus, R. H. (1975). "Interdiffusion of Hydrogen and Alkali Ions in a Glass Surface". In: *Glass Surfaces*. Elsevier, pp. 137–144. ISBN: 978-0-7204-0419-7.

Dove, P. M., N. Han, A. F. Wallace, and J. J. De Yoreo (2008). "Kinetics of Amorphous Silica Dissolution and the Paradox of the Silica Polymorphs". In: *Proceedings of the National Academy of Sciences* 105.29, pp. 9903–9908.

Frugier, P. et al. (2008). "SON68 Nuclear Glass Dissolution Kinetics: Current State of Knowledge and Basis of the New GRAAL Model". In: *Journal of Nuclear Materials* 380.1-3, pp. 8–21. ISSN: 00223115. DOI: `10.1016/j.jnucmat.2008.06.044`.

Geisler, T., A. Janssen, D. Scheiter, T. Stephan, J. Berndt, and A. Putnis (2010). "Aqueous Corrosion of Borosilicate Glass under Acidic Conditions: A New Corrosion Mechanism". In: *Journal of Non-Crystalline Solids* 356.28-30, pp. 1458–1465. ISSN: 00223093. DOI: `10.1016/j.jnoncrysol.2010.04.033`.

Geisler, T., T. Nagel, M. R. Kilburn, A. Janssen, J. P. Icenhower, R. O. Fonseca, M. Grange, and A. A. Nemchin (2015). "The Mechanism of Borosilicate Glass Corrosion Revisited". In: *Geochimica et Cosmochimica Acta* 158, pp. 112–129. ISSN: 00167037. DOI: `10.1016/j.gca.2015.02.039`.

Gin, S. (2014). "Open Scientific Questions about Nuclear Glass Corrosion". In: *Procedia Materials Science* 7, pp. 163–171. ISSN: 22118128. DOI: `10.1016/j.mspro.2014.10.022`.

Gin, S., J. Ryan, D. Schreiber, J. Neeway, and M. Cabié (2013a). "Contribution of Atom-Probe Tomography to a Better Understanding of Glass Alteration Mechanisms: Application to a Nuclear Glass Specimen Altered 25years in a Granitic Environment". In: *Chemical Geology* 349-350, pp. 99–109. ISSN: 00092541. DOI: `10.1016/j.chemgeo.2013.04.001`.

Gin, S. et al. (2013b). "An International Initiative on Long-Term Behavior of High-Level Nuclear Waste Glass". In: *Materials Today* 16.6, pp. 243–248. ISSN: 13697021. DOI: `10.1016/j.mattod.2013.06.008`.

Gin, S. et al. (2016). "The Controversial Role of Inter-Diffusion in Glass Alteration". In: *Chemical Geology* 440, pp. 115–123. ISSN: 00092541. DOI: `10.1016/j.chemgeo.2016.07.014`.

Gin, S. et al. (2017). "Atom-Probe Tomography, TEM and ToF-SIMS Study of Borosilicate Glass Alteration Rim: A Multiscale Approach to Investigating Rate-Limiting Mechanisms". In: *Geochimica et Cosmochimica Acta* 202, pp. 57–76. ISSN: 00167037. DOI: `10.1016/j.gca.2016.12.029`.

Gin, S., C. Guittonneau, N. Godon, D. Neff, D. Rebiscoul, M. Cabié, and S. Mostefaoui (2011). “Nuclear Glass Durability: New Insight into Alteration Layer Properties”. In: *The Journal of Physical Chemistry C* 115.38, pp. 18696–18706. ISSN: 1932-7447, 1932-7455. DOI: `10.1021/jp205477q`.

Gin, S., P. Jollivet, M. Fournier, F. Angeli, P. Frugier, and T. Charpentier (2015a). “Origin and Consequences of Silicate Glass Passivation by Surface Layers”. In: *Nature Communications* 6, p. 6360. ISSN: 2041-1723. DOI: `10.1038/ncomms7360`.

Gin, S., P. Jollivet, M. Fournier, C. Berthon, Z. Wang, A. Mitroshkov, Z. Zhu, and J. V. Ryan (2015b). “The Fate of Silicon during Glass Corrosion under Alkaline Conditions: A Mechanistic and Kinetic Study with the International Simple Glass”. In: *Geochimica et Cosmochimica Acta* 151, pp. 68–85. ISSN: 00167037. DOI: `10.1016/j.gca.2014.12.009`.

Gormanns, P., S. Reckow, J. C. Poczatek, C. W. Turck, and C. Lechene (2012). “Segmentation of Multi-Isotope Imaging Mass Spectrometry Data for Semi-Automatic Detection of Regions of Interest”. In: *PloS one* 7.2, e30576. ISSN: 1932-6203.

Grambow, B. and R. Müller (2001). “First-Order Dissolution Rate Law and the Role of Surface Layers in Glass Performance Assessment”. In: *Journal of Nuclear Materials* 298.1, pp. 112–124.

Guittonneau, C., S. Gin, N. Godon, J. Mestre, O. Dugne, and P. Allegri (2011). “A 25-Year Laboratory Experiment on French SON68 Nuclear Glass Leached in a Granitic Environment – First Investigations”. In: *Journal of Nuclear Materials* 408.1, pp. 73–89. ISSN: 00223115. DOI: `10.1016/j.jnucmat.2010.10.075`.

Hellmann, R., S. Cotte, E. Cadel, S. Malladi, L. S. Karlsson, S. Lozano-Perez, M. Cabié, and A. Seyeux (2015). “Nanometre-Scale Evidence for Interfacial Dissolution–Reprecipitation Control of Silicate Glass Corrosion”. In: *Nature Materials* 14.3, pp. 307–311. ISSN: 1476-1122, 1476-4660. DOI: `10.1038/nmat4172`.

Hellmann, R., R. Wirth, D. Daval, J.-P. Barnes, J.-M. Penisson, D. Tisserand, T. Epicier, B. Florin, and R. L. Hervig (2012). “Unifying Natural and Laboratory Chemical Weathering with Interfacial Dissolution–Reprecipitation: A Study Based on the Nanometer-Scale Chemistry of Fluid–Silicate Interfaces”. In: *Chemical Geology* 294-295, pp. 203–216. ISSN: 00092541. DOI: `10.1016/j.chemgeo.2011.12.002`.

Hövelmann, J., A. Putnis, T. Geisler, B. C. Schmidt, and U. Golla-Schindler (2010). “The Replacement of Plagioclase Feldspars by Albite: Observations from Hydrothermal Experiments". In: *Contributions to Mineralogy and Petrology* 159.1, pp. 43–59. ISSN: 0010-7999, 1432-0967. DOI: `10.1007/s00410-009-0415-4`.

Icenhower, J. P. and C. I. Steefel (2013). "Experimentally Determined Dissolution Kinetics of SON68 Glass at 90° C over a Silica Saturation Interval: Evidence against a Linear Rate Law". In: *Journal of Nuclear Materials* 439.1, pp. 137–147.

Iler, R. K. (1979). *The Chemistry of Silica: Solubility, Polymerization, Colloid and Surface Properties and Biochemistry of Silica.* John Wiley & Sons. 896 pp. ISBN: 978-0-471-02404-0.

Jégou, C., S. Gin, and F. Larché (2000). "Alteration Kinetics of a Simplified Nuclear Glass in an Aqueous Medium: Effects of Solution Chemistry and of Protective Gel Properties on Diminishing the Alteration Rate". In: *Journal of Nuclear Materials* 280.2, pp. 216–229.

Jollivet, P., F. Angeli, C. Cailleteau, F. Devreux, P. Frugier, and S. Gin (2008). "Investigation of Gel Porosity Clogging during Glass Leaching". In: *Journal of Non-Crystalline Solids* 354.45-46, pp. 4952–4958. ISSN: 00223093. DOI: `10.1016/j.jnoncrysol.2008.07.023`.

Kasioptas, A., T. Geisler, C. Perdikouri, C. Trepmann, N. Gussone, and A. Putnis (2011). "Polycrystalline Apatite Synthesized by Hydrothermal Replacement of Calcium Carbonates". In: *Geochimica et Cosmochimica Acta* 75.12, pp. 3486–3500.

Kita, I., S. Taguchi, and O. Matsubaya (1985). "Oxygen Isotope Fractionation between Amorphous Silica and Water at 34-93[Deg]C". In: *Nature* 314.6006, pp. 83–84. DOI: `10.1038/314083a0`.

Kossel, W. (1927). "Extenoling the Law of Bravais". In: *Nach. Ges. Wiss. Gottingen* 143, p. 25.

Kusebauch, C., T. John, M. J. Whitehouse, S. Klemme, and A. Putnis (2015). "Distribution of Halogens between Fluid and Apatite during Fluid-Mediated Replacement Processes". In: *Geochimica et Cosmochimica Acta* 170 (Supplement C), pp. 225–246. ISSN: 0016-7037. DOI: `https://doi.org/10.1016/j.gca.2015.08.023`.

Leng, M. J. and P. A. Barker (2006). "A Review of the Oxygen Isotope Composition of Lacustrine Diatom Silica for Palaeoclimate Reconstruction". In: *Earth-Science Reviews* 75.1-4, pp. 5–27. ISSN: 00128252. DOI: `10.1016/j.earscirev.2005.10.001`.

Lenting, C., T. Geisler, A. Gerdes, E. Kooijman, E. E. Scherer, and A. Zeh (2010). “The Behavior of the Hf Isotope System in Radiation-Damaged Zircon during Experimental Hydrothermal Alteration”. In: *American Mineralogist* 95.8-9, pp. 1343–1348. ISSN: 0003-004X. DOI: `10.2138/am.2010.3521`.

Lenting, C., O. Plümper, M. Kilburn, P. Guagliardo, M. Klinkenberg, and T. Geisler (2018). “Towards a Unifying Mechanistic Model for Silicate Glass Corrosion”. In: *npj Materials Degradation* 2.1, p. 28. ISSN: 2397-2106. DOI: `10.1038/s41529-018-0048-z`.

Nakouzi, E. and O. Steinbock (2016). “Self-Organization in Precipitation Reactions Far from the Equilibrium”. In: *Science Advances* 2.8, e1601144–e1601144. ISSN: 2375-2548. DOI: `10.1126/sciadv.1601144`.

O’Neil, J. R. (1977). “Stable Isotopes in Mineralogy”. In: *Physics and Chemistry of Minerals* 2.1, pp. 105–123.

Pearson, C. (1988). *Conservation of Marine Archaeological Objects.* Elsevier. ISBN: 978-0-408-10668-9.

Pedrosa, E. T., C. V. Putnis, F. Renard, A. Burgos-Cara, B. Laurich, and A. Putnis (2016). “Porosity Generated during the Fluid-Mediated Replacement of Calcite by Fluorite”. In: *CrystEngComm* 18.36, pp. 6867–6874. DOI: `10.1039/C6CE01150K`.

Pöml, P., M. Menneken, T. Stephan, D. Niedermeier, T. Geisler, and A. Putnis (2007). “Mechanism of Hydrothermal Alteration of Natural Self-Irradiated and Synthetic Crystalline Titanate-Based Pyrochlore”. In: *Geochimica et Cosmochimica Acta* 71.13, pp. 3311–3322.

Putnis, A. (2002). “Mineral Replacement Reactions: From Macroscopic Observations to Microscopic Mechanisms”. In: *Mineralogical Magazine* 66.5, pp. 689–708. ISSN: 14718022, 0026461X. DOI: `10.1180/0026461026650056`.

Putnis, C. V. and K. Mezger (2004). “A Mechanism of Mineral Replacement: Isotope Tracing in the Model System KCl-KBr-H2O”. In: *Geochimica et Cosmochimica Acta* 68.13, pp. 2839–2848. ISSN: 00167037. DOI: `10.1016/j.gca.2003.12.009`.

Putnis, C. V. and E. Ruiz-Agudo (2013). “The Mineral–Water Interface: Where Minerals React with the Environment”. In: *Elements* 9.3, pp. 177–182.

Rebiscoul, D., A. Van der Lee, F. Rieutord, F. Né, O. Spalla, A. El-Mansouri, P. Frugier, A. Ayral, and S. Gin (2004). “Morphological Evolution of Alteration Layers

Formed during Nuclear Glass Alteration: New Evidence of a Gel as a Diffusive Barrier". In: *Journal of Nuclear Materials* 326.1, pp. 9–18. ISSN: 00223115. DOI: `10.1016/j.jnucmat.2003.10.015`.

Ruiz-Agudo, E., C. Putnis, and A. Putnis (2014). "Coupled Dissolution and Precipitation at Mineral–Fluid Interfaces". In: *Chemical Geology* 383, pp. 132–146. ISSN: 00092541. DOI: `10.1016/j.chemgeo.2014.06.007`.

Ruiz-Agudo, E., C. V. Putnis, C. Rodriguez-Navarro, and A. Putnis (2012). "Mechanism of Leached Layer Formation during Chemical Weathering of Silicate Minerals". In: *Geology* 40.10, pp. 947–950. ISSN: 1943-2682, 0091-7613. DOI: `10.1130/G33339.1`.

Schalm, O. and W. Anaf (2016). "Laminated Altered Layers in Historical Glass: Density Variations of Silica Nanoparticle Random Packings as Explanation for the Observed Lamellae". In: *Journal of Non-Crystalline Solids* 442, pp. 1–16. ISSN: 00223093. DOI: `10.1016/j.jnoncrysol.2016.03.019`.

Schindelin, J. et al. (2012). "Fiji: An Open-Source Platform for Biological-Image Analysis". In: *Nat Meth* 9.7, pp. 676–682. ISSN: 1548-7091. DOI: `10.1038/nmeth.2019`.

Sterpenich, J. and G. Libourel (2001). "Using Stained Glass Windows to Understand the Durability of Toxic Waste Matrices". In: *Chemical Geology* 174.1–3. 6th International Silicate Melt Workshop, pp. 181–193. ISSN: 0009-2541. DOI: `http://dx.doi.org/10.1016/S0009-2541(00)00315-6`.

Stranski, I. (1928). "Zur Theorie Des Kristallwachstums: Zeitschrift Fur Physikalische Chemie, v. 136". In:

Suzuki, T., H. Endo, and M. Shibayama (2008). "Analysis of Surface Structure and Hydrogen/Deuterium Exchange of Colloidal Silica Suspension by Contrast-Variation Small-Angle Neutron Scattering". In: *Langmuir* 24.9, pp. 4537–4543. DOI: `10.1021/la7039515`.

Valle, N., A. Verney-Carron, J. Sterpenich, G. Libourel, E. Deloule, and P. Jollivet (2010). "Elemental and Isotopic (29Si and 18O) Tracing of Glass Alteration Mechanisms". In: *Geochimica et Cosmochimica Acta* 74.12, pp. 3412–3431. ISSN: 00167037. DOI: `10.1016/j.gca.2010.03.028`.

Van Iseghem, P. and B. Grambow (1987). "The Long-Term Corrosion and Modelling of Two Simulated Belgian Reference High-Level Waste Glasses". In: *MRS Proceedings* 112. ISSN: 0272-9172. DOI: `10.1557/PROC-112-631`.

Van Iseghem, P. et al. (2004). “GLAMOR: A Critical Evaluation of the Dissolution Mechanisms of High-Level Waste Glasses in Conditions of Relevance for Geological Disposal”. In:

Verney-Carron, A., S. Gin, P. Frugier, and G. Libourel (2010). “Long-Term Modeling of Alteration-Transport Coupling: Application to a Fractured Roman Glass”. In: *Geochimica et Cosmochimica Acta* 74.8, pp. 2291–2315. ISSN: 00167037. DOI: `10.1016/j.gca.2010.01.001`.

Verney-Carron, A., S. Gin, and G. Libourel (2008). “A Fractured Roman Glass Block Altered for 1800 Years in Seawater: Analogy with Nuclear Waste Glass in a Deep Geological Repository”. In: *Geochimica et Cosmochimica Acta* 72.22, pp. 5372–5385. ISSN: 00167037. DOI: `10.1016/j.gca.2008.08.018`.

Wang, Y., C. F. Jove-Colon, and K. L. Kuhlman (2016). “Nonlinear Dynamics and Instability of Aqueous Dissolution of Silicate Glasses and Minerals”. In: *Scientific Reports* 6.1. ISSN: 2045-2322. DOI: `10.1038/srep30256`.

Chapter 5

Towards a unifying corrosion mechanism

5.1 Introduction

Within the last three chapters, the process of the corrosion of borosilicate glass was described from the first surface precipitates at the inward-moving solution-glass interface, over the dynamic development of the corrosion rim itself, and the tracing of individual species within the corrosion rim and across the rim-glass interface. A comprehensive study of the entire spectrum of (early) borosilicate glass corrosion was presented. As a synthesis,the new observation shall used to formulate a unifying mechanistic model merging previously contradicting glass corrosion models. Before that, a brief summary of the most significant findings will be given.

5.1.1 Concentration gradient(s) at solution-glass interface

The dual approach by AFM and SPFT experimental corrosion of glasses delivered strong evidence for a significant compositional difference between the surfacial and bulk solution, influencing the overall corrosion progress. The development of concentration gradients can explain how precipitation of amorphous silica at the glass surface under nominally undersaturated conditions (in the bulk solution) could be achieved. It further diminishes the need for two different mechanistic approaches (congruent dissolution and ion exchange coupled with *in situ* reconstruction of a 'leached' gel phase) to explain both congruent and (apparently) incongruent dissolution behaviour of the same glass at different conditions (Gin et al., 2015a; Gin et al., 2015b). The (implied) establishment of flow rate-depending concentration gradients is not an entirely new finding in general, but was recently described for mineral replacement reactions (Ruiz-Agudo et al., 2016), in which also amorphous silica was the corrosion product. This precipitation and the flow rate dependence of the solution stoichiometry found in the SPFT experiments is substantial evidence to assume the occurrence of strong concentration gradients, for at least solute Si, between the bulk solution and the dissolving glass surface.

5.1.2 Water-rich interfacial layer

The most striking feature of glass corrosion found in the FC-HRS *in situ* experiment is the development of the water-rich zone at the interface between glass and corrosion rim. Gaps or cracks between pristine glass and corrosion rim are commonly found in dried samples from *ex situ* experiments (e.g., Anaf, 2010; Sterpenich and Libourel, 2001;

Geisler et al., 2010; Geisler et al., 2015; Dohmen et al., 2013) and are explained to be the result of cracking or ripping apart due to shrinkage of the previously hydrous silica layer. However, in this work the development of a water-rich zone was observed *in situ*, i.e., while the process was running, implying that it is part of the corrosion process rather than a by-product of sample treatment. The concentration of water or OH-bearing phases at the reaction interface is a common phenomenon and immanent feature of mineral replacement by interface-coupled dissolution-precipitation (ICDP) (A. Putnis, 2002; A. Putnis and C. V. Putnis, 2007). The development of the water-rich zone also shows a strong correlation with the structural maturation of the initial corrosion rim, which might slow down mass transport through the corrosion rim over time. The sudden formation of this initial corrosion rim of about 90 µm within a few hours is further evidence that the glass corrosion is proceeding by an ICDP mechanism (Geisler et al., 2010; Geisler et al., 2015), and that it is not restricted to high alkaline conditions as previously suggested (Gin et al., 2015b). Solid state diffusion-controlled hydrolysis and ion exchange cannot facilitate glass corrosion over such an extend within a short time frame.

5.1.3 Decoupling of isotope tracers & quench layer

The results of the isotope tracer (^{2}H,^{18}O,^{10}B, ^{30}Si, ^{44}Ca) corrosion experiments that were performed with precorroded and pristine glass monoliths of a range of chemical compositions exhibited multiple decoupling between the individual tracers as shown by NanoSIMS analyses. ^{18}O and ^{2}H decoupled at a phase boundary between the silica-based corrosion rim and the underlying, pristine glass, suggesting the diffusion of protons into the glass while molecular water was repressed at the glass surface. The diffusion of ^{2}H into the glass was found to coincide with the outward diffusion of Na^{+}. However, ^{30}Si, even-though abundant in solution, was not detected within the corrosion rim. In a previous study (Geisler et al., 2015), a solute silicon tracer was observed to be partly incorporated into the corrosion rim, however, there the corrosion rim exhibited porosity on the micrometer-scale. It thus seems likely that steric hindrance by the nanometre-sized interstitial pores might have inhibited vast exchange of larger hydrated silica polymorphs. In contrast to Geisler et al., 2015, the oxygen tracer indicated the corrosion rim to be reactive even after its initial formation. The older, outer rim layers of the precorroded samples reveal the same (unnatural) oxygen isotope ratios as the newly formed rims.

This further implies that there was sufficient water transport and exchange over the entire corrosion rim to equilibrate the oxygen isotopes. It has to be noted that the experimental run times were longer here than in Geisler et al., 2015, providing more time for isotope equilibration.

Furthermore, TEM analysis of these samples revealed dense silica layer at the interface between the corrosion rim and the leached glass. Such dense layers are often found within gaps of *post mortem* analysed glass samples of extensively corroded glasses (see above), where the shrinkage of the larger corrosion rims pulled itself apart from the underlying glass. In one precorroded sample another dense layer was identified within the corrosion rim, suggesting that this layer is a relic of the precorrosion step and thus indeed a quench layer precipitated from an interfacial (pore) solution.

5.2 Refined corrosion model

On basis of the above mentioned findings and ground-laying work on ICDP in glass corrosion presented in previous studies (Geisler et al., 2010; Geisler et al., 2015; Dohmen et al., 2013), a refined model for the glass corrosion mechanism is proposed that unifies diffusion-controlled ion exchange in the glass with an interface-coupled glass dissolution-silica precipitation reaction that forms the actual corrosion rim. It provides a fundamental basis for predictive modelling of silicate glass corrosion. The refined model is schematically drawn out in Figure 5.1 for the general case of glass corrosion, but also for the special case of the precorroded QBG experiment (Chapter 4, Fig. 4.9, p.104). The individual reactions involved in the overall corrosion process and their interdependences are presented in the flow chart in Figure 5.2 and will be discussed in the following.

5.2.1 Dissolution

Glass corrosion occurs in diluted (e.g., Icenhower et al., 2008; Kerisit and Pierce, 2011; Inagaki et al., 2012; Inagaki et al., 2013) as well as in silica saturated solutions (e.g., Kerisit and Pierce, 2012; Gin et al., 2015a), whereas there is no linear correlation between silica saturation and corrosion rate (Icenhower and Steefel, 2013). The absolute aqueous solubility of glass is also not relevant in an ICDP process. It is the solubility difference between parent phase (here: glass) and the corrosion product (amorphous silica) which provides the necessary thermodynamic driving force (A. Putnis, 2002; A.

Putnis and C. V. Putnis, 2007). As such, the low solubility of borosilicate glasses does not stand in contrast to their corrosion. Since even at low solubility of the parent phase in solution, the saturation of the solvent with respect to the product phase will result in its precipitation. In this lies the most basic feature and fundamental distinction to any other proposed model. The glass network will be dissolved congruently, which is coupled in space and time to the formation of the corrosion rim by precipitation of amorphous silica. Interestingly, this replacement reaction appears to be more pseudomorphic at low pH values, where the solubility of glass and silica are very low, i.e., dissolved silicon from the glass is quickly saturated in the interfacial solution and directly reprecipitated as amorphous silica. As such, a homogeneously structured corrosion rim is formed, whereas at high pH chemical patterns and structural variations of the corrosion rim are observed (Dohmen et al., 2013; Geisler et al., 2015). Thus, the rate-limiting factor is not the absolute solubility and/or precipitation, but solely the kinetics of the dissolution of the glass network, i.e. the rupture of chemical bonds by hydrolysis. As indicated by ion exchange profiles across the reaction interface (e.g., Gin et al., 2015a; Gin et al., 2015b), the hydrolysis of less strongly-bound glass network modifiers seems to be energetically favoured over higher coordinated network builders. Nevertheless, as overall thermodynamic equilibrium between glass and water cannot be reached, in the next step network bonds like Si-O, Zr-O or Al-O must be broken. Dove et al. (2008) suggested a mechanism for the step-wise dissolution of the disordered silica surface by electrolyte-mediated hydrolysis attack on the highly coordinated Q^3 species, which, in turn, creates a surface of reactive, less coordinated Q^2 species that increase the surface energy. Considering that solute Na^+ increases the pH of the nearby solution, more hydroxyl molecules become available for this hydrolysis reaction. As such, the congruent dissolution of glass is achieved. Depending on the rate of dissolution, solid-state reactive diffusion of protons into the glass may also occur. However, solid-state diffusion rates are generally rather low at ambient to slightly elevated temperatures (potentially occurring in high-level nuclear waste repositories). Thus, larger diffusion profiles of hydrogen can only be expected once the ICDP process has slowed down (Gin et al., 2017) due to reasons discussed below. In light of the application of borosilicate glasses for the safe disposal of high-level nuclear waste, the disintegration of the radionuclide-binding matrix is naturally highly critical for the long-term safety assessment.

5.2.2 Polycondensation, nucleation & precipitation

Initially, in silica undersaturated solution, the dissolved glass constituents will be transported away depending on the concentration gradient between glass surface and bulk solution and/or flow rate of the surrounding aqueous medium. If the transport of solutes is effective, the reaction simply continues with congruent dissolution of the glass (Fig. 5.1a, Fig. 5.2). Thus, in high-flow and/or bulk diluted systems, precipitation should not occur. However, if the mass transport to the bulk solution is slower than the rate of solvation, solute concentration at the glass surface will increase. If saturation with respect to a thermodynamic stable phase is reached, nucleation and precipitation will occur (Fig. 5.1b,c). One of the least soluble phases in the case of silicate glasses is amorphous silica.

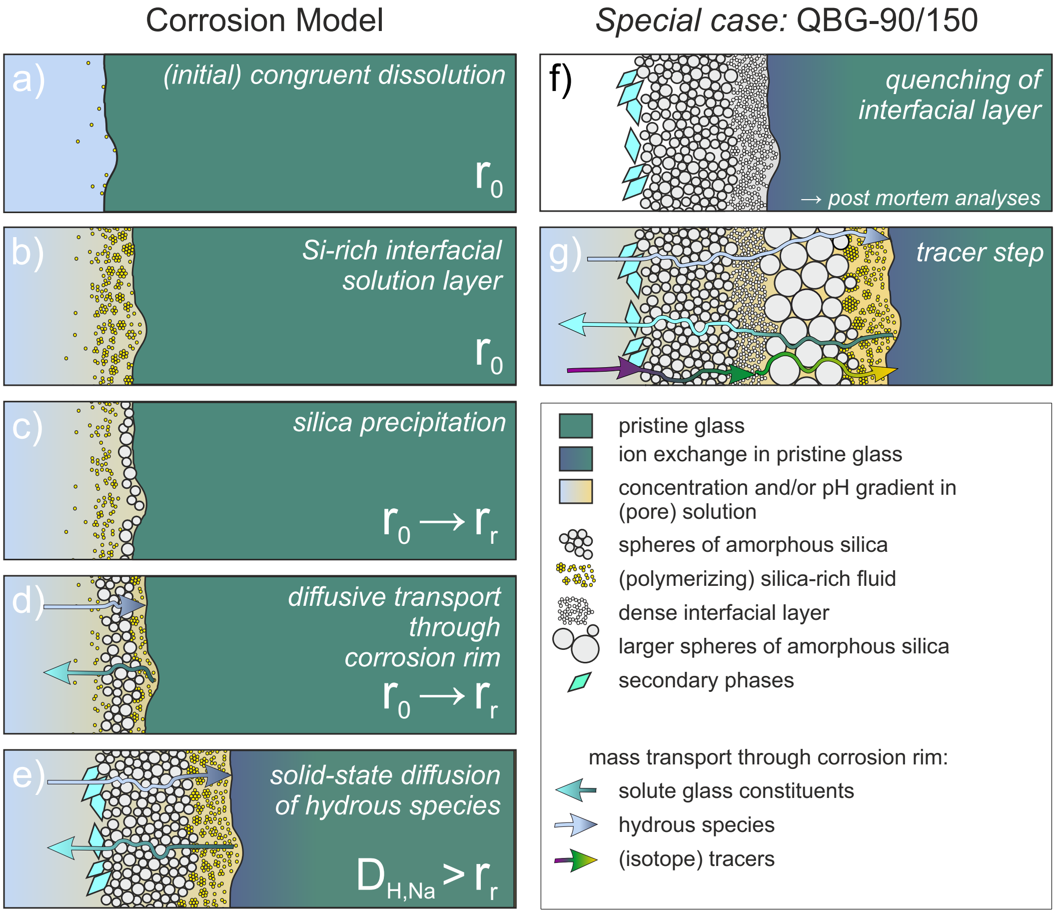

Figure 5.1: Revised phenomenological model (based on Geisler et al., 2015).

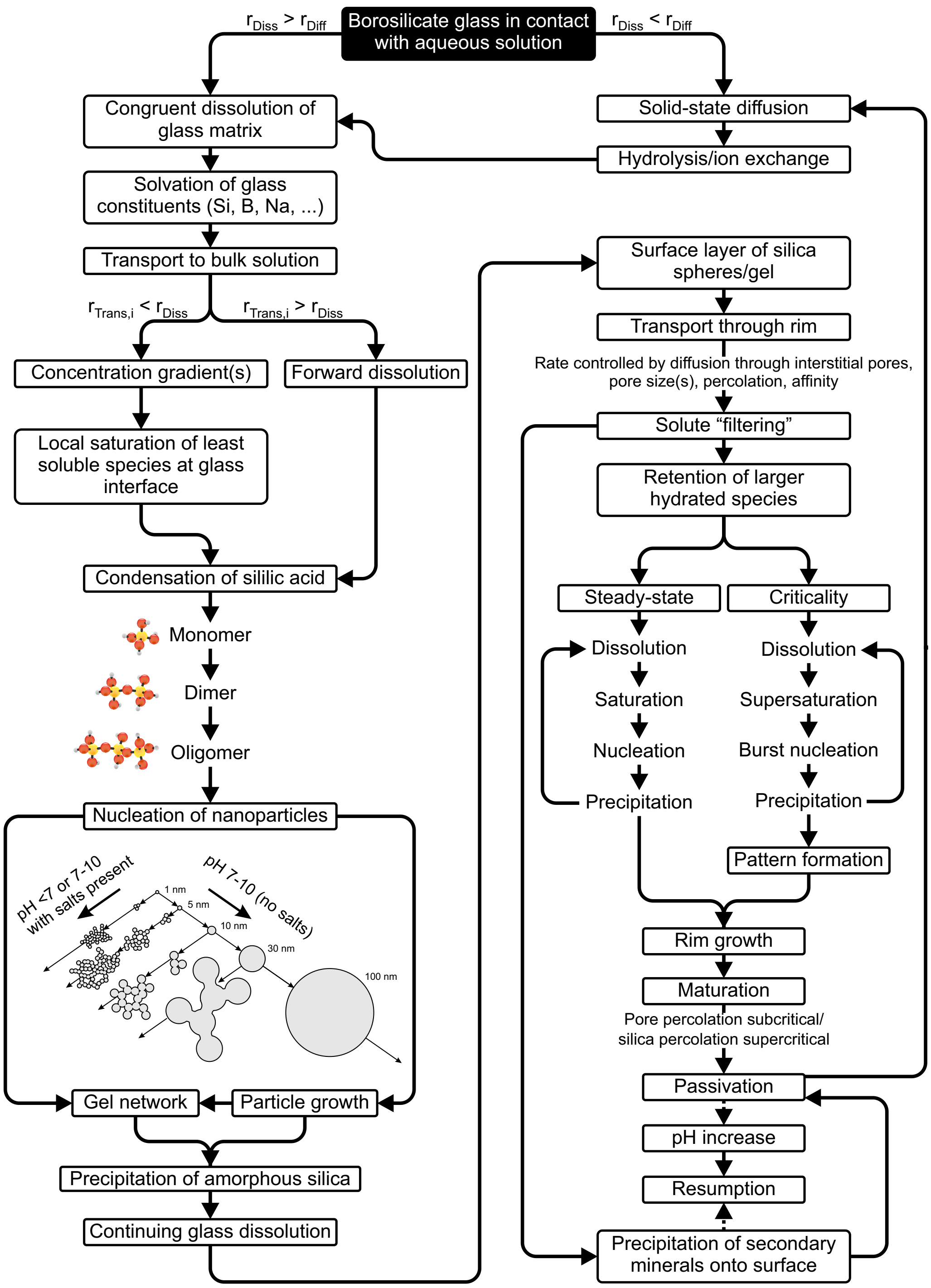

Figure 5.2: Flow chart for the revised phenomenological model of the glass corrosion process. Nucleation scheme of nanoparticles (left side) is redrawn after Iler (1979).

At high enough supersaturation of silica in the (local) solution, silica dimers form by self-condensation reaction of orthosilicic acids, which is catalysed by OH$^-$ above the isoelectric point at pH ≈2 (and by H$^+$ at lower pH) (Iler, 1979,Fig. 5.2):

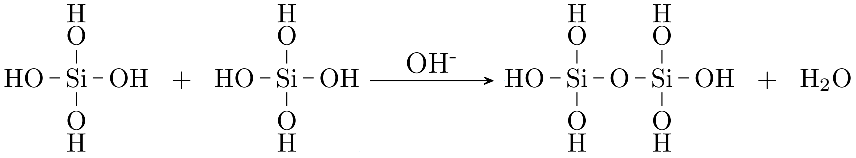

$$\mathrm{Si(OH)_4} + \mathrm{Si(OH)_4} \xrightarrow{\mathrm{OH^-}} \mathrm{(HO)_3Si{-}O{-}Si(OH)_3} + \mathrm{H_2O} \qquad (5.1)$$

In comparison to the following condensation reactions, the monomer-monomer condensation has generally the lowest reaction rate (Rothbaum and Rohde, 1979). The polycondensation of silica continues by addition of a monomer to intermediately ionized dimers (Iler, 1979, Fig. 5.2):

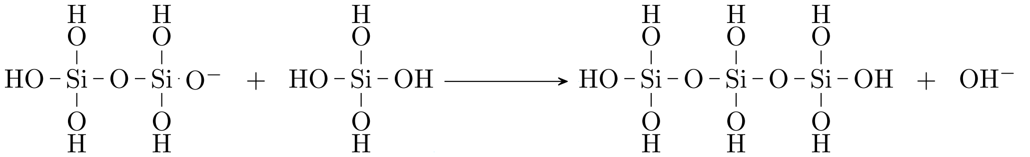

$$\mathrm{(HO)_3Si{-}O{-}Si(OH)_2O^-} + \mathrm{Si(OH)_4} \longrightarrow \mathrm{(HO)_3Si{-}O{-}Si(OH)_2{-}O{-}Si(OH)_3} + \mathrm{OH^-} \qquad (5.2)$$

Such trimer will (Eq. (5.2)) polycondense to a tetramer by further monomer attachment, but it can also form by the condensation of two dimers:

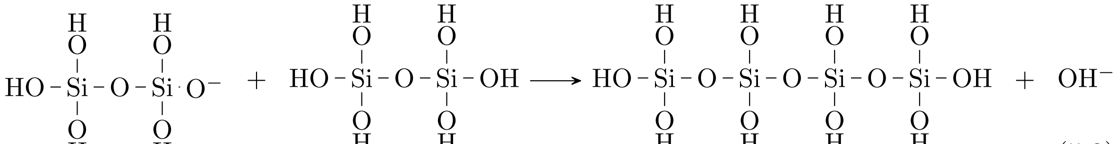

$$\mathrm{(HO)_3Si{-}O{-}Si(OH)_2O^-} + \mathrm{(HO)_3Si{-}O{-}Si(OH)_3} \longrightarrow \mathrm{(HO)_3Si{-}O{-}Si(OH)_2{-}O{-}Si(OH)_2{-}O{-}Si(OH)_3} + \mathrm{OH^-} \qquad (5.3)$$

As cyclic structures are energetically more favourable than linear chains (Iler, 1979; Sefcik and McCormick, 1997), tetramer rings are formed by the condensation of silanol end groups:

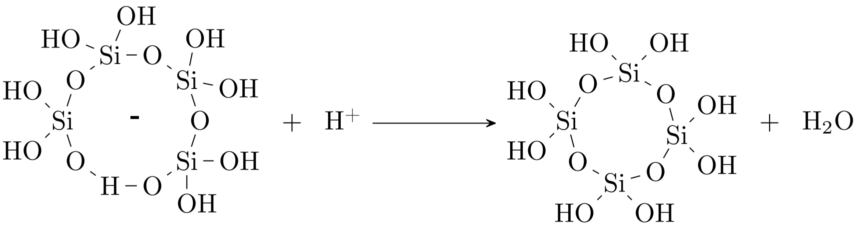

(5.4)

Monomer and dimer will then preferentially attach to the ionized, active sites of the ring structures. Continuous silanol group condensation leads to larger and more compact three-dimensional polymers, from which eventually colloidal nanoparticles may form. Silica polycondensation also leads to the formation of larger polymers of nine-fold ring structures or linear hexamers as evidenced by ^{29}NMR and UV-Raman studies (Cho et al., 2006; Depla et al., 2011), whereby these larger oligomers are less abundant than four-fold rings or tetramers. The overall polycondensation process follows a fourth-order rate law (Icopini et al., 2005), and depends on the silica concentration/supersaturation and the ionization potential of the individual species or sites, which, in turn, depends on the pH of the solution (Iler, 1979). As such, the condensation rate is at a minimum around the isoelectric point (pH $\approx$2), while its maximum can be observed at a pH of around 7, where silica exhibits the highest charge density (Iler, 1979). Moreover, at silicon concentrations close to the equilibrium with respect to amorphous silica, an induction period is reported, during which little or no oligomerization was detected. This was attributed to the time necessary for the formation of critical nuclei of amorphous silica (White et al., 1956; Baumann, 1959; Rothbaum and Rohde, 1979). The duration of this induction period ranges hereby from minutes to several days. It decreases with increasing supersaturation and/or increasing ionic strength of the solution, and, in turn, with decreasing temperature. Moreover, the induction period decreases towards the point of neutral pH in solution. Additionally, Rothbaum & Rhode reported (1979) that fewer silica polymers are formed at higher temperatures, but, in return, their average molecular weight and, as such, their size increases by several orders of magnitude.

It is noteworthy that while free OH^- acts as a catalyst for the polymerization by the formation of siloxane bridges, this process is reversible, i.e., OH^- also drives hydrolysis and depolymerisation (Iler, 1979). It follows that a polymeric nucleus stays in an equilibrium with the monomer concentration of the solution. Particle formation is achieved, once an anhydrous SiO_2 core has formed by continued addition of monomers to the active sites of a polymeric nucleus. At the same time, silanol groups in the inside of the nucleus condense with each other forming new siloxane bridges. The surface of such nanoparticles is estimated to contain about 40-50 silicon atoms (Iler, 1979). At low pH or high ionic strength of the solution, the negative surface charge of these nanoparticles will be compensated by hydronium and/or cations, and the nanoparticles agglomerate and form a gel network. At alkaline conditions, the negative surface charge repels nanoparticles from each other, and particle growth by consumption of monomers can continue (see Fig. 5.2). The monomer depletion in solution follows to the thermodynamic destabilisation, depolymerisation and dissolution of oligomers in solution, which, in turn, promotes further particle growth. Moreover, larger particles grow at the expense of smaller ones

by Ostwald ripening (Ostwald, 1897). The resulting sphere size is thereby independent from the silica concentration, but mainly depends on the given temperature (Iler, 1979). The latter explains the two sets of silica sphere sizes observed in the corrosion rim of the QBG-90/150 experiment in the tracer study, in which the inner section of the corrosion rim, formed at 150 °C, reveals three times larger silica spheres than the outer section (formed at 90 °C) (Chapter 4, Fig. 4.12, p. 108).
Intergrowth of spheres will occur, when two (or more) silica spheres collide. The negative curvature at the contact point of these spherical particles is infinitely small, by which the silica solubility becomes zero and, as a result, intergrowth occurs by instant monomer addition (Iler, 1979). Intergrowth between silica sphere and glass surface is likely not of long continuance due to the thermodynamic instability of glass. Nonetheless, precipitation and accumulation of silica spheres onto the corroding surface (Fig. 5.1c) is reported in numerous studies (e.g., Bunker (1994), Abraitis et al. (2000), Jégou et al. (2000), and Geisler et al. (2015)), and was also observed in the AFM experiments of this study (Chapter 2, Fig. 2.5, p.41). Polycondensation, precipitation and growth of amorphous silica decreases the silica concentration in the nearby solution and, consequently, promotes further glass dissolution. The initial silica precipitation at the glass surface will at one point form a continuous layer of silica spheres (Fig. 5.1c). Further precipitation will preferentially occur onto this silica layer, where the spheres intergrow at their contact points forming a coherent, stable layer (Iler, 1979).

5.2.3 Silica sphere-based corrosion rim

With water and mass transport through the interstitial pores of the intergrown silica spheres, congruent glass dissolution can continue and eventually the connectivity of the underlying glass to the silica sphere layer may partly or entirely be lost (Fig. 5.1d), an effect that was also observed *in situ* (see Chapter 3, p. 57). The reason for this is that while water and small soluble elements are transported across the rim, larger solutes may be subject to transport limitations (Fig. 5.1d,e). Especially the major element forming the corrosion rim, silicon released from the glass dissolution, should be affected. Silicon exhibits a range of aqueous species with increasing pH ($SiOH_4$, $Si_4O_8(OH)_6{}^{2-}$, $Si_4O_8(OH)_4{}^{4-}$, $SiO(OH)_3{}^{-}$, $SiO_2(OH)_2{}^{2-}$, (Brinker and Scherer, 1990)), and polycondensates to larger polymers (see above), which will likely slow down its transport across the corrosion rim into the bulk solution. Moreover, not only will the increase in size of the silica polymer decrease their mobility, but also the surface change density restricts transport rates with increasing size of the silica nulcei (up to about 100 nm (Barisik et al., 2014), which is below the measured sizes in this study (see Chapter 4), Fig. 4.12, p. 108). On the other side, the results of the isotope tracer experiments presented here as well as those of a previous study (Gin et al., 2015b) demonstrated that silicon dissolved in the bulk solution can be restricted from entering the corrosion rim in larger amounts. Comparing most recent isotope tracer studies, it seems that the amount of silicon from solution being incorporated into the corrosion rim may be anti-correlated to the silica saturation of the bulk solution, i.e., at low to medium silica saturation abundant silicon tracer could be detected in the corrosion rim (Valle et al., 2010; Bouakkaz et al., 2016), while at high silica concentration only slight enrichment could be detected (Gin et al., 2015b). Geisler et al. (2015) reported silicon isotope tracer incorporation, however, not uniformly, but only in porous sections of the corrosion rims, which larger oligomers can naturally access more readily. Two mechanism, which are not mutually exclusive, can explain this behaviour: (1) The silicon isotope exchange rate must be coupled to the residence time of the ion in solution. At high silica supersaturation, monomeric silica, released from the glass during congruent dissolution, quickly polycondensates (Rothbaum and Rohde, 1979) and reprecipitates at the glass surface to form the corrosion rim before the silicon of the tracer solution and the dissolved silicon from the glass can exchange and equilibrate. (2) High silica supersaturation promotes oligomerisation. The increasing size of polycondensating oligomers will decrease their transport rates due to electrostatic and steric hinderance within the bulk solution as well as within the corrosion rim, where the transport is governed by the pore size, pore connectivity and its surface charge.

However, the retention of solute silicon in the corrosion rim may even enhance the glass corrosion. If the retained solute silica eventually polycondensates, nucleates and/or precipitates, these reactions (re-)release OH^- groups into the solution (see Eqs. (5.1) to (5.3)). This release would increase the pH value of the pore solution, whereby the congruent glass dissolution is enhanced. Such feedback loop may occur in a steady-state or by a nonlinear phenomenon of criticality (Fig. 5.2). A similar feedback mechanism for oscillatory dissolution behaviour was developed by Wang et al. (2016) for alkaline conditions based on the phenomenological model of Dohmen et al. (2013) and Geisler et al. (2015), in which cations, e.g. Na^+, primarily released by glass dissolution create a positive feedback loop by increasing the pH at the reaction interface and, as such, enhance the dissolution kinetics and the silica solubility. An increase in dissolved silica by glass dissolution coupled with transport limitation across the corrosion rim, can lead to high concentrations of silica in the interfacial solution. In alkaline conditions, in which the silica solubility increases drastically with increasing pH, any process lowering the pH will imminently lead to high degrees of supersaturation of silica, by which burst nucleation and following precipitation can produce fine layers of monodispersed silica spheres (LaMer and Dinegar, 1950). Such critical phenomenon may explain the formation of structural and in consequence also chemical pattern observed in corroded glasses (see Chapter 1, p. 18). A plausible scenario for pattern formation is as follows: (1) A corrosion rim of a certain width has formed that retains solute silica, (2) which polycondensates with increasing silica supersaturation in the interfacial solution. (3) Polycondensation reactions re-release OH^- groups into the interfacial solution (Eqs. (5.1) to (5.3)), increasing its pH, while simultaneously silica nuclei precipitate and silica spheres grow on the extend of monomeric acid or smaller particles. (4) The enhanced increase in pH by the release of sodium from the continuous congruent glass dissolution and the re-release from silica polycondensation leads to an increase in glass dissolution and results in high supersaturation of silica in the interfacial solution. (5) At sufficient supersaturation, burst nucleation will quickly produce a fine layer of small, monodispersed silica spheres (LaMer and Dinegar, 1950), which in contrast to the larger, steadily grown silica spheres can retain more OH^- groups and solute sodium due to their higher surface area to volume ratio. (6) Corrosion then continues again with congruent glass dissolution and silica precipitation as in (1). Whether pattern formation occurs and can be triggered by a critical phenomenon such as burst nucleation, might depend on the alkaline content of the dissolving glass.

With time, the maturation of the corrosion rim by Ostwald ripening (Ostwald, 1897) and polycondensation may eventually fully restrict solute and water transport across the corrosion rim (Fig. 5.1d,e, Fig. 5.2). This can be achieved as a result of pore size reduction itself, which is evidenced by the higher degree of polymerization and decrease of molecular water adsorption in the *in situ* Raman experiment (see Chapter 3, Fig. 3.5, p. 70). Moreover, the percolation of the interstitial pores can become subcritical, meaning that the connectivity of the pore network across the corrosion rim is not given any more. Silicic acid and other glass constituents therefore pile up in the interfacial (pore) solution, which may lead to aggregation and gelation. It follows that less and less silicic acid can be detached from the glass, transported, and dissolved into this interfacial suspension or gel, slowing down the surface-controlled dissolution process. As such, the corrosion rim or specifically the dense interfacial layer might become passivating and the corrosion only proceeds at an up to 200 times slower residual rate (Frugier et al., 2008; Gin et al., 2015a). Only at this point the like-wise slow solid-state diffusion of protons into the pristine glass may become more prominent and an interdiffusion zone may develop (Fig. 5.1e, Fig. 5.2). However, in some situation this stage will never be reached, i.e., dissolution proceeds in a steady state as long as transport through the corrosion rim is possible. Gin et al. (2017) reported results of corrosion experiment similar to those conducted in the isotope tracer study presented in this work, in which the diffusion of hydrogen into the pristine glass proceeded after the corrosion rate itself had dropped by several orders of magnitude. The advance of the hydrogen diffusion front decouples from the slowed congruent dissolution of the glass, which indicates that the protonation of the glass network cannot be rate-limiting for the replacement of the glass by amorphous silica Gin et al., 2017. Hence, the long-term corrosion rate, i.e., the rate of replacement, must be limited by the transport of elements through the corrosion rim formed by amorphous silica.

However, resumption of corrosion may also occur as observed in the *in situ* Raman experiment in this work. A possible explanation is that the passivation of the corrosion rim will also inhibit or sufficiently slow down the transport of solute sodium away from the corrosion interface. Possibly, the continuous growth of silica sphere decreases their effective surface size, which will re-release previously adsorbed sodium and other alkali elements back in the pore solution. The resulting increase in pH will then again increase the congruent dissolution rate of the thermodynamically unstable glass, which, in turn, releases more sodium to the interfacial pore solution (Wang et al., 2016). Such resumption of the corrosion rate was observed as expansion of the water-rich zone at the corrosion interface in the *in situ* Raman experiment (Chapter 3, Fig. 3.4, p. 69). Often, the resumption of corrosion is correlated with the late-stage precipitation of secondary minerals at the surface of the corrosion rim (Ribet and Gin, 2004; Jantzen et al., 2008; Fournier et al., 2014; Frugier et al., 2017), whereby the precipitating minerals, such as phyllosilicates and zeolites, consumes elements adsorbed to surface of the silica sphere in the corrosion rim and as such re-initiates solute transport across the corrosion rim.

5.3 Conclusion

In summary, several observations made in these project studies as well as in other recent studies challenge the available corrosion models that consider the corrosion rim as a residual and restructured glass. First, results of atomic force microscopy and single-pass flow-through experiments deliver strong evidence for a significant compositional difference between the surfacial and bulk solution. Hence, local supersaturation of the interfacial solution with respect to amorphous silica at the glass surface can explain how precipitation of silica can occur when the bulk solution is still undersaturated.

The findings of a clear phase boundary between the dense silica-based corrosion rim and a chemically leached glass (as observed by STEM), which agrees with the nanometre-sharp reaction interfaces observed by APT (Gin et al., 2017; Hellmann et al., 2015), question the intensively propagated concept of a continuous ion exchange-based transition from a pristine glass to a residual, chemically leached and re-structured glass. Moreover, with a novel fluid cell-based *in situ* Raman spectroscopy method it could eventually be shown that a silica- and water-rich zone occurs at this sharp interface between corrosion rim and glass during the corrosion process. Commonly such zones were identified *post mortem* as gaps or cracks between pristine glass and corrosion rim, and, hence, referred to as result of sample drying. These results show that these discontinuities are a primary feature of the corrosion process itself and that the dissolution process must proceed within the therein present interfacial solution.

However, the isotope tracer data from experimentally corroded borosilicate glasses, containing variable amounts of Al, Ca, and/or Zr, unambiguously reveal the formation of an interdiffusion zone ahead of an ICDP interface. This implies that both processes are not mutually exclusive as suggested by Hellmann and coworkers (2015; 2012) and supports previous assumptions that solid-state interdiffusion and related structural relaxation of the glass may be an important process during long-term glass corrosion (Chave et al., 2007; Gin et al., 2017; McGrail et al., 2001). Since the interdiffusion of hydrogen and network modifiers in silicate glasses is usually slow at temperatures that are relevant in most natural or technical systems ($D_H = 1.3 \times 10^{-23}\,m^2\,s^{-1}$), the ICDP process must slow down significantly from typical forward glass dissolution rates in the order of 10^{-12} - 10^{-15} m/s (Icenhower and Steefel, 2015) before an interdiffusion zone can form. Based on textural evidence from HAADF-STEM images, it is proposed that a dense silica layer, observed at the boundary to the glass, reflects the product of quenching and drying of an interfacial (pore) solution that was supersaturated in dissolved silica. This solution forms since with increasing thickness of the corrosion rim aqueous silica cannot effectively be transported away anymore from the dissolution-reprecipitation interface towards the bulk solution. Silicic acid and other glass constituents therefore pile up at the ICDP interface, which may lead to aggregation and gelation. It follows that less and less silicic acid can be detached from the glass, transported, and dissolved into the interfacial suspension or gel, slowing down the surface-controlled dissolution process so that the interdiffusion process becomes the faster process.

The conclusion is that an interface-coupled dissolution-precipitation (ICDP) and an interdiffusion process are not mutual exclusive. The diffusion process may replace the ICDP process but only if the ICDP process significantly slows down. In such a case, the long-term release of elements from the glass becomes dependent on the transport properties of the glass and the growing corrosion rim. Following reactions have so far been identified in this and other studies:

1. Congruent dissolution of the glass (including several individual microscopic reaction steps such as hydrolysis, detachment, transport).
2. Silica precipitation/deposition from an interfacial solution (including several individual microscopic reaction steps such as, e.g., condensation, coagulation, aggregation, ripening).
3. Solid-state ion exchange/interdiffusion inside the glass (e.g., Doremus model (Doremus, 1975; Doremus et al., 1983)).
4. Silica aging (e.g., polymerization, ripening) (Cailleteau et al., 2008).
5. Chemical transport through the silica-based corrosion rim (porosity-controlled) (Geisler et al., 2010; Geisler et al., 2015).
6. Precipitation of secondary minerals within and at the silica surface (e.g., zeolites, clays etc. (Ribet and Gin, 2004)).
7. Aqueous diffusion within a solution boundary layer that allows for silica-saturation at the glass surface before the bulk solution is silica-saturated (Geisler et al., 2010; Geisler et al., 2015; Ruiz-Agudo et al., 2016).

A sound description of the reaction mechanisms and the identification of the rate-limiting steps is essential to predict reliably the long-term corrosion of silicate glasses, particularly when time scales must reach several thousand to millions of years as necessary for safety regulations for a nuclear repository. Accordingly, all above given processes and their interdependencies as well as the dependence of transport properties of the corrosion rim on the morphology of precipitated silica should be considered in future kinetic models.

5.4 References

Abraitis, P. K., F. R. Livens, J. E. Monteith, J. S. Small, D. P. Trivedi, D. J. Vaughan, and R. A. Wogelius (2000). "The Kinetics and Mechanisms of Simulated British Magnox Waste Glass Dissolution as a Function of pH, Silicic Acid Activity and Time in Low Temperature Aqueous Systems". In: *Applied Geochemistry* 15.9, pp. 1399–1416.

Anaf, W. (2010). "Study on the Formation of Heterogeneous Structures in Leached Layers during the Corrosion Process of Glass". In: *CeROArt. Conservation, Exposition, Restauration d'Objets d'Art.* CeROArt asbl.

Barisik, M., S. Atalay, A. Beskok, and S. Qian (2014). "Size Dependent Surface Charge Properties of Silica Nanoparticles". In: *The Journal of Physical Chemistry C* 118.4, pp. 1836–1842. ISSN: 1932-7447. DOI: `10.1021/jp410536n`.

Baumann, H. (1959). "Polymerisation Und Depolymerisation Der Kieselsäure Unter Verschiedenen Bedingungen". In: *Kolloid-Zeitschrift* 162.1, pp. 28–35.

Bouakkaz, R., A. Abdelouas, Y. El Mendili, B. Grambow, and S. Gin (2016). "SON68 Glass Alteration under Si-Rich Solutions at Low Temperature (35–90° C): Kinetics, Secondary Phases and Isotopic Exchange Studies". In: *RSC Advances* 6.76, pp. 72616–72633.

Brinker, C. J. and G. W. Scherer (1990). *Sol-Gel Science: The Physics and Chemistry of Sol-Gel Processing.* San Diego: Academic press. ISBN: 978-0-12-134970-7.

Bunker, B. (1994). "Molecular Mechanisms for Corrosion of Silica and Silicate Glasses". In: *Journal of Non-Crystalline Solids* 179, pp. 300–308.

Cailleteau, C., F. Angeli, F. Devreux, S. Gin, J. Jestin, P. Jollivet, and O. Spalla (2008). "Insight into Silicate-Glass Corrosion Mechanisms". In: *Nature Materials* 7.12, pp. 978–983. ISSN: 1476-1122, 1476-4660. DOI: `10.1038/nmat2301`.

Chave, T., P. Frugier, A. Ayral, and S. Gin (2007). “Solid State Diffusion during Nuclear Glass Residual Alteration in Solution”. In: *Journal of Nuclear Materials* 362.2-3, pp. 466–473. ISSN: 00223115. DOI: `10.1016/j.jnucmat.2007.01.095`.

Cho, H., A. R. Felmy, R. Craciun, J. P. Keenum, N. Shah, and D. A. Dixon (2006). “Solution State Structure Determination of Silicate Oligomers by 29Si NMR Spectroscopy and Molecular Modeling”. In: *Journal of the American Chemical Society* 128.7, pp. 2324–2335.

Depla, A. et al. (2011). “29Si NMR and UV- Raman Investigation of Initial Oligomerization Reaction Pathways in Acid-Catalyzed Silica Sol- Gel Chemistry”. In: *The Journal of Physical Chemistry C* 115.9, pp. 3562–3571.

Dohmen, L., C. Lenting, R. O. C. Fonseca, T. Nagel, A. Heuser, T. Geisler, and R. Denkler (2013). “Pattern Formation in Silicate Glass Corrosion Zones”. In: *International Journal of Applied Glass Science* 4.4, pp. 357–370. ISSN: 20411286. DOI: `10.1111/ijag.12046`.

Doremus, R. H. (1975). “Interdiffusion of Hydrogen and Alkali Ions in a Glass Surface”. In: *Glass Surfaces*. Elsevier, pp. 137–144. ISBN: 978-0-7204-0419-7.

Doremus, R. H., Y. Mehrotra, W. Lanford, and C. Burman (1983). “Reaction of Water with Glass: Influence of a Transformed Surface Layer”. In: *Journal of Materials Science* 18.2, pp. 612–622.

Dove, P. M., N. Han, A. F. Wallace, and J. J. De Yoreo (2008). “Kinetics of Amorphous Silica Dissolution and the Paradox of the Silica Polymorphs”. In: *Proceedings of the National Academy of Sciences* 105.29, pp. 9903–9908.

Fournier, M., S. Gin, and P. Frugier (2014). “Resumption of Nuclear Glass Alteration: State of the Art”. In: *Journal of Nuclear Materials* 448.1-3, pp. 348–363. ISSN: 00223115. DOI: `10.1016/j.jnucmat.2014.02.022`.

Frugier, P. et al. (2008). “SON68 Nuclear Glass Dissolution Kinetics: Current State of Knowledge and Basis of the New GRAAL Model”. In: *Journal of Nuclear Materials* 380.1-3, pp. 8–21. ISSN: 00223115. DOI: `10.1016/j.jnucmat.2008.06.044`.

Frugier, P., M. Fournier, and S. Gin (2017). “Modeling Resumption of Glass Alteration Due to Zeolites Precipitation”. In: *Procedia Earth and Planetary Science* 17, pp. 340–343. ISSN: 18785220. DOI: `10.1016/j.proeps.2016.12.086`.

Geisler, T., A. Janssen, D. Scheiter, T. Stephan, J. Berndt, and A. Putnis (2010). “Aqueous Corrosion of Borosilicate Glass under Acidic Conditions: A New Corrosion

Mechanism”. In: *Journal of Non-Crystalline Solids* 356.28-30, pp. 1458–1465. ISSN: 00223093. DOI: `10.1016/j.jnoncrysol.2010.04.033`.

Geisler, T., T. Nagel, M. R. Kilburn, A. Janssen, J. P. Icenhower, R. O. Fonseca, M. Grange, and A. A. Nemchin (2015). “The Mechanism of Borosilicate Glass Corrosion Revisited”. In: *Geochimica et Cosmochimica Acta* 158, pp. 112–129. ISSN: 00167037. DOI: `10.1016/j.gca.2015.02.039`.

Gin, S. et al. (2017). “Atom-Probe Tomography, TEM and ToF-SIMS Study of Borosilicate Glass Alteration Rim: A Multiscale Approach to Investigating Rate-Limiting Mechanisms”. In: *Geochimica et Cosmochimica Acta* 202, pp. 57–76. ISSN: 00167037. DOI: `10.1016/j.gca.2016.12.029`.

Gin, S., P. Jollivet, M. Fournier, F. Angeli, P. Frugier, and T. Charpentier (2015a). “Origin and Consequences of Silicate Glass Passivation by Surface Layers”. In: *Nature Communications* 6, p. 6360. ISSN: 2041-1723. DOI: `10.1038/ncomms7360`.

Gin, S., P. Jollivet, M. Fournier, C. Berthon, Z. Wang, A. Mitroshkov, Z. Zhu, and J. V. Ryan (2015b). “The Fate of Silicon during Glass Corrosion under Alkaline Conditions: A Mechanistic and Kinetic Study with the International Simple Glass”. In: *Geochimica et Cosmochimica Acta* 151, pp. 68–85. ISSN: 00167037. DOI: `10.1016/j.gca.2014.12.009`.

Hellmann, R., S. Cotte, E. Cadel, S. Malladi, L. S. Karlsson, S. Lozano-Perez, M. Cabié, and A. Seyeux (2015). “Nanometre-Scale Evidence for Interfacial Dissolution–Reprecipitation Control of Silicate Glass Corrosion”. In: *Nature Materials* 14.3, pp. 307–311. ISSN: 1476-1122, 1476-4660. DOI: `10.1038/nmat4172`.

Hellmann, R., R. Wirth, D. Daval, J.-P. Barnes, J.-M. Penisson, D. Tisserand, T. Epicier, B. Florin, and R. L. Hervig (2012). “Unifying Natural and Laboratory Chemical Weathering with Interfacial Dissolution–Reprecipitation: A Study Based on the Nanometer-Scale Chemistry of Fluid–Silicate Interfaces”. In: *Chemical Geology* 294-295, pp. 203–216. ISSN: 00092541. DOI: `10.1016/j.chemgeo.2011.12.002`.

Icenhower, J. P., B. P. McGrail, W. J. Shaw, E. M. Pierce, P. Nachimuthu, D. K. Shuh, E. A. Rodriguez, and J. L. Steele (2008). “Experimentally Determined Dissolution Kinetics of Na-Rich Borosilicate Glass at Far from Equilibrium Conditions: Implications for Transition State Theory”. In: *Geochimica et Cosmochimica Acta* 72.12, pp. 2767–2788. ISSN: 00167037. DOI: `10.1016/j.gca.2008.02.026`.

Icenhower, J. P. and C. I. Steefel (2013). "Experimentally Determined Dissolution Kinetics of SON68 Glass at 90° C over a Silica Saturation Interval: Evidence against a Linear Rate Law". In: *Journal of Nuclear Materials* 439.1, pp. 137–147.

Icenhower, J. P. and C. I. Steefel (2015). "Dissolution Rate of Borosilicate Glass SON68: A Method of Quantification Based upon Interferometry and Implications for Experimental and Natural Weathering Rates of Glass". In: *Geochimica et Cosmochimica Acta* 157, pp. 147–163. ISSN: 0016-7037. DOI: `10.1016/j.gca.2015.02.037`.

Icopini, G. A., S. L. Brantley, and P. J. Heaney (2005). "Kinetics of Silica Oligomerization and Nanocolloid Formation as a Function of pH and Ionic Strength at 25 C". In: *Geochimica et Cosmochimica Acta* 69.2, pp. 293–303.

Iler, R. K. (1979). *The Chemistry of Silica: Solubility, Polymerization, Colloid and Surface Properties and Biochemistry of Silica.* John Wiley & Sons. 896 pp. ISBN: 978-0-471-02404-0.

Inagaki, Y., T. Kikunaga, K. Idemitsu, and T. Arima (2013). "Initial Dissolution Rate of the International Simple Glass as a Function of pH and Temperature Measured Using Microchannel Flow-Through Test Method". In: *International Journal of Applied Glass Science* 4.4, pp. 317–327. ISSN: 20411286. DOI: `10.1111/ijag.12043`.

Inagaki, Y., H. Makigaki, K. Idemitsu, T. Arima, S.-I. Mitsui, and K. Noshita (2012). "Initial Dissolution Rate of a Japanese Simulated High-Level Waste Glass P0798 as a Function of pH and Temperature Measured by Using Micro-Channel Flow-through Test Method". In: *Journal of Nuclear Science and Technology* 49.4, pp. 438–449. ISSN: 0022-3131, 1881-1248. DOI: `10.1080/00223131.2012.669246`.

Jantzen, C. M., D. I. Kaplan, N. E. Bibler, D. K. Peeler, and M. John Plodinec (2008). "Performance of a Buried Radioactive High Level Waste (HLW) Glass after 24 Years". In: *Journal of Nuclear Materials* 378.3, pp. 244–256. ISSN: 00223115. DOI: `10.1016/j.jnucmat.2008.06.040`.

Jégou, C., S. Gin, and F. Larché (2000). "Alteration Kinetics of a Simplified Nuclear Glass in an Aqueous Medium: Effects of Solution Chemistry and of Protective Gel Properties on Diminishing the Alteration Rate". In: *Journal of Nuclear Materials* 280.2, pp. 216–229.

Kerisit, S. and E. M. Pierce (2011). “Monte Carlo Simulations of the Dissolution of Borosilicate and Aluminoborosilicate Glasses in Dilute Aqueous Solutions”. In: *Geochimica et Cosmochimica Acta* 75.18, pp. 5296–5309. ISSN: 00167037. DOI: `10.1016/j.gca.2011.06.036`.

Kerisit, S. and E. M. Pierce (2012). “Monte Carlo Simulations of the Dissolution of Borosilicate Glasses in Near-Equilibrium Conditions”. In: *Journal of Non-Crystalline Solids* 358.10, pp. 1324–1332. ISSN: 00223093. DOI: `10.1016/j.jnoncrysol.2012.03.003`.

LaMer, V. K. and R. H. Dinegar (1950). “Theory, Production and Mechanism of Formation of Monodispersed Hydrosols”. In: *Journal of the American Chemical Society* 72.11, pp. 4847–4854.

McGrail, B. P. et al. (2001). “The Structure of Na 2 O–Al 2 O 3–SiO 2 Glass: Impact on Sodium Ion Exchange in H 2 O and D 2 O”. In: *Journal of non-crystalline solids* 296.1, pp. 10–26.

Ostwald, W. (1897). “Studien Über Die Bildung Und Umwandlung Fester Körper”. In: *Zeitschrift für physikalische Chemie* 22.1, pp. 289–330.

Putnis, A. (2002). “Mineral Replacement Reactions: From Macroscopic Observations to Microscopic Mechanisms”. In: *Mineralogical Magazine* 66.5, pp. 689–708. ISSN: 14718022, 0026461X. DOI: `10.1180/0026461026650056`.

Putnis, A. and C. V. Putnis (2007). “The Mechanism of Reequilibration of Solids in the Presence of a Fluid Phase”. In: *Journal of Solid State Chemistry* 180.5, pp. 1783–1786. ISSN: 00224596. DOI: `10.1016/j.jssc.2007.03.023`.

Ribet, S. and S. Gin (2004). “Role of Neoformed Phases on the Mechanisms Controlling the Resumption of SON68 Glass Alteration in Alkaline Media”. In: *Journal of Nuclear Materials* 324.2-3, pp. 152–164.

Rothbaum, H. and A. Rohde (1979). “Kinetics of Silica Polymerization and Deposition from Dilute Solutions between 5 and 180 C”. In: *Journal of Colloid and Interface Science* 71.3, pp. 533–559.

Ruiz-Agudo, E., H. E. King, L. D. Patiño-López, C. V. Putnis, T. Geisler, C. Rodriguez-Navarro, and A. Putnis (2016). “Control of Silicate Weathering by Interface-Coupled Dissolution-Precipitation Processes at the Mineral-Solution Interface”. In: *Geology* 44.7, pp. 567–570. ISSN: 0091-7613, 1943-2682. DOI: `10.1130/G37856.1`.

Sefcik, J. and A. V. McCormick (1997). “Thermochemistry of Aqueous Silicate Solution Precursors to Ceramics”. In: *AIChE Journal* 43.S11, pp. 2773–2784.

Sterpenich, J. and G. Libourel (2001). “Using Stained Glass Windows to Understand the Durability of Toxic Waste Matrices”. In: *Chemical Geology* 174.1–3. 6th International Silicate Melt Workshop, pp. 181–193. ISSN: 0009-2541. DOI: `http://dx.doi.org/10.1016/S0009-2541(00)00315-6`.

Valle, N., A. Verney-Carron, J. Sterpenich, G. Libourel, E. Deloule, and P. Jollivet (2010). “Elemental and Isotopic (29Si and 18O) Tracing of Glass Alteration Mechanisms”. In: *Geochimica et Cosmochimica Acta* 74.12, pp. 3412–3431. ISSN: 00167037. DOI: `10.1016/j.gca.2010.03.028`.

Wang, Y., C. F. Jove-Colon, and K. L. Kuhlman (2016). “Nonlinear Dynamics and Instability of Aqueous Dissolution of Silicate Glasses and Minerals”. In: *Scientific Reports* 6.1. ISSN: 2045-2322. DOI: `10.1038/srep30256`.

White, D. E., W. Brannock, and K. Murata (1956). “Silica in Hot-Spring Waters”. In: *Geochimica et Cosmochimica Acta* 10.1-2, pp. 27–59.